

# Emerging versatile two-dimensional $\text{MoSi}_2\text{N}_4$ family

Yan Yin,<sup>1</sup> Qihua Gong,<sup>1, 2,\*</sup> Min Yi,<sup>1, †</sup> and Wanlin Guo<sup>1, ‡</sup>

<sup>1</sup>*Institute for Frontier Science & State Key Lab of Mechanics and Control of Mechanical Structures & Key Lab for Intelligent Nano Materials and Devices of Ministry of Education & College of Aerospace Engineering, Nanjing University of Aeronautics and Astronautics (NUAA), Nanjing 210016, China*

<sup>2</sup>*MIIT Key Lab of Aerospace Information Materials and Physics & College of Physics, Nanjing University of Aeronautics and Astronautics (NUAA), Nanjing 210016, China*

(Dated: October 29, 2022)

The discovery of two-dimensional (2D) layered  $\text{MoSi}_2\text{N}_4$  and  $\text{WSi}_2\text{N}_4$  without knowing their 3D parents by chemical vapor deposition in 2020 has stimulated extensive studies of 2D  $\text{MA}_2\text{Z}_4$  system due to its structural complexity and diversity as well as versatile and intriguing properties. Here, a comprehensive overview on the state-of-the-art progress of this 2D  $\text{MA}_2\text{Z}_4$  family is presented. Starting by describing the unique sandwich structural characteristics of the emerging monolayer  $\text{MA}_2\text{Z}_4$ , we summarize and anatomize their versatile properties including mechanics, piezoelectricity, thermal transport, electronics, optics/optoelectronics, and magnetism. The property tunability via strain engineering, surface functionalization and layered strategy is also elaborated. Theoretical and experimental attempts or advances in applying 2D  $\text{MA}_2\text{Z}_4$  to transistors, photocatalysts, batteries and gas sensors are then reviewed to show its prospective applications over a vast territory. We further discuss new opportunities and suggest prospects for this emerging 2D family. The overview is anticipated to guide the further understanding and exploration on 2D  $\text{MA}_2\text{Z}_4$ .

## I. INTRODUCTION

Two-dimensional (2D) materials have intrigued great attentions over the years since their fantastic characteristics are close to and even superior than their bulk counterparts, for instance, excellent mechanical properties [1–3], ultrahigh heat conduction [4–6], unique quantum effects in low dimensions (e.g., superconductivity and quantum hall effect, etc.) [7–11]. Since graphene has been successfully prepared by mechanical exfoliation [12–14], most 2D members have been prepared by the top-down exfoliation of their naturally existed bulk parent materials, e.g., mechanical stripping materials ( $\text{MoS}_2$ , h-BH,  $\text{NbSe}_2$ ,  $\text{MnBi}_2\text{Te}_4$ ) [15–17], interface-assisted exfoliation materials (black phosphorene,  $\text{FeSe}$ ,  $\text{Fe}_3\text{GeTe}_2$ ,  $\text{RuCl}_3$ ,  $\text{PtSe}_2$ ,  $\text{PtTe}_2$ ,  $\text{PdTe}_2$ , and  $\text{CrSiTe}_3$ ) [18, 19], and fluid dynamics assisted exfoliation [20–22]. However, their structures are essentially limited by the parent materials. Bottom-up growth method, an another fabrication strategy, has been applied to synthesize dozens of novel 2D materials, e.g., monolayer borophene by direct evaporation [23, 24], multilayer TMDs by chemical vapor deposition (CVD) [25, 26], 2D van der Waals (vdW) heterostructures designed by mechanically assembled stacks [27], and other materials prepared via layer-by-layer stacking in a specific sequence. However, 2D materials synthesized by this method face the challenge of discontinuous growth due to the surface energy constraints.

Recently, Ren and the coworkers successfully prepared novel 2D layer materials ( $\text{MoSi}_2\text{N}_4$  and  $\text{WSi}_2\text{N}_4$ ) without

knowing their 3D parents, and broke through the obstacle of island growth [28]. In their growing process, a Cu/Mo bilayer was used as the substrate and  $\text{NH}_3$  gas as the nitrogen source. The crucial point of layer growth by CVD is that the appropriate atomic passivation of surface dangling bonds favors the decrement of surface energy. The growth diagrams of 2D molybdenum nitride without ( $\text{MoN}_2$ ) or with Si ( $\text{MoSi}_2\text{N}_4$ ) are shown in Fig. 1(a). The growing progress of  $\text{MoN}_2$  without Si shows the obvious island domains and finally uneven micrometer-scale domains (appropriately 10 nm thick) form. On the contrary,  $\text{MoN}_2$  with Si ( $\text{MoSi}_2\text{N}_4$ ) firstly forms as triangular domains with uniform thickness, then expands to a centimeter-scale uniform polycrystalline film, and eventually maintains great ambient stabilization, as shown in Fig. 1(b). The high-angle annular dark field scanning TEM (HAADF-STEM) observation (Fig. 1(c) and (d)) indicates that  $\text{MoSi}_2\text{N}_4$  is a  $\text{MoN}_2$ -derived septuple-atomic-layer compound built up in the order of N-Si-N-Mo-N-Si-N. The vdW form of  $\text{MoSi}_2\text{N}_4$  can be grown layer by layer due to the free of dangling bonds, indicating the possibility of large-scale preparation of this 2D compound.

Thanks to the breakthrough achievement in experimental synthesis, series of theoretical studies on  $\text{MoSi}_2\text{N}_4$  and its derived materials have been further carried out. Density functional theory (DFT) calculations define this septuple-atomic-layer compounds as 2D  $\text{MA}_2\text{Z}_4$  family [29]. This 2D ternary material includes group IVB, VB and VIB elements for M-site atom, group IVA elements for A-site atom and group VA elements for Z-site atom. The general approach to design  $\text{MA}_2\text{Z}_4$  family layered van der Waals materials is proposed by intercalating  $\text{MoS}_2$ -type  $\text{MZ}_2$  layer into an InSe-type  $\text{A}_2\text{Z}_2$  monolayer (Fig. 1(e)) [29]. If 2H and 1T phases of  $\text{MZ}_2$  and  $\alpha$  and  $\beta$  phases of  $\text{A}_2\text{Z}_2$  are considered, 4

\* [gongqihua@nuaa.edu.cn](mailto:gongqihua@nuaa.edu.cn)

† [yimin@nuaa.edu.cn](mailto:yimin@nuaa.edu.cn)

‡ [wlguo@nuaa.edu.cn](mailto:wlguo@nuaa.edu.cn)

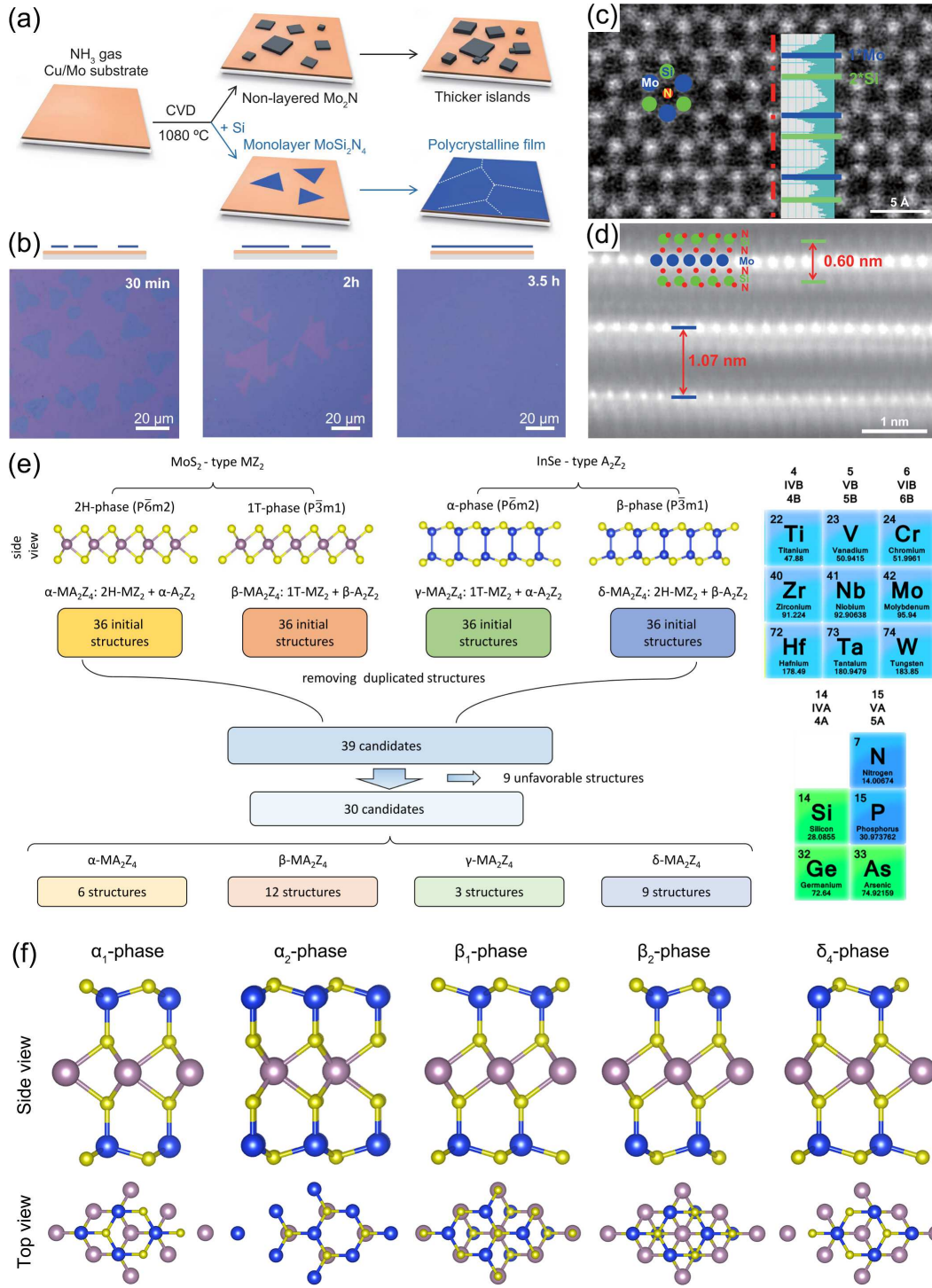


FIG. 1. (a) Growth diagrams of  $\text{MoN}_2$  and  $\text{MoSi}_2\text{N}_4$  by CVD. (b) Optical images of  $\text{MoSi}_2\text{N}_4$  grown by CVD for 30 min, 2 hours, and 3.5 hours. High-angle annular dark field scanning TEM (HAADF-STEM) imaging: (c) top view and (d) side view. (e) Schematic illustration of the intercalation method that uses the structures of a  $\text{MoS}_2$ -like monolayer (2H- and 1T phases) and those of an InSe-like monolayer ( $\alpha$  and  $\beta$  phases) to construct the structures of monolayer  $\text{MA}_2\text{Z}_4$  family. (f) Unit cells for stable 2D  $\text{MA}_2\text{Z}_4$  with different structures. [28, 29]

types of monolayer  $\text{MA}_2\text{Z}_4$  nanosheets can be obtained, i.e.,  $\alpha_i\text{-MA}_2\text{Z}_4$  ( $i = 1\text{--}6$ ),  $\beta_i\text{-MA}_2\text{Z}_4$  ( $i = 1\text{--}12$ ),  $\gamma_i\text{-MA}_2\text{Z}_4$  ( $i = 1\text{--}3$ ) and  $\delta_i\text{-MA}_2\text{Z}_4$  ( $i = 1\text{--}9$ ). In total,

there exist 30 structures of this family by removing duplicate symmetry and abandoning the structures that are energetically unstable. Five stable structures of 2D

$\text{MA}_2\text{Z}_4$  are shown in Fig. 1(f). The experimentally synthesized and the most widely studied structure is  $\alpha_1\text{-MA}_2\text{Z}_4$ . Due to the rich compositions and diverse structures,  $\text{MA}_2\text{Z}_4$  family has exhibited intriguing physical and chemical characteristics, such as non-linear optics and second harmonic response [30, 31], quantum behavior of strong exciton-phonon coupling in  $\alpha_1\text{-MoSi}_2\text{N}_4$  [32, 33], spin polarization and plasmon properties in  $\alpha_1\text{-MoSi}_2\text{N}_4$  [34, 35], superconductivity in  $\alpha_1\text{-TaSi}_2\text{N}_4$  and  $\text{NbSi}_2\text{N}_4$  [36], topological insulating property in  $\beta_2\text{-SrGa}_2\text{Se}_4$  and  $\text{SrGa}_2\text{Te}_4$  [29], ferromagnetic nature in  $\delta_4\text{-VSi}_2\text{P}_4$  [29], valley-half-semiconducting property in  $\alpha_1\text{-VSi}_2\text{N}_4$  [37], Mott transition in  $\text{XSi}_2\text{N}_4$  [38], etc. These intriguing properties could enable promising applications of  $\text{MA}_2\text{Z}_4$  family in nanoelectronic devices such as magnetic tunnel junction, field effect transistors, highly sensitive and reusable gas sensors, etc. [39–46]

In this paper, we aim to review the recent progress of the novel 2D layered  $\text{MA}_2\text{Z}_4$  family, in terms of its structures, versatile properties and perspective applications. After introducing the diverse structures in Fig. 1, we provide an extensive overview on the versatile properties regarding to mechanics, piezoelectricity, thermal transport, electronics, optics/optoelectronics, and magnetism. The tunability of each property via strain engineering, surface functionalization and layered strategy (e.g., multilayer or heterostructure) is also expounded. Then, we introduce the perspective applications derived from the excellent properties of  $\text{MA}_2\text{Z}_4$ , including transistors, photocatalysts, batteries and sensors. Finally, we summarize the outstanding advantages of this family and suggest the conceivable outlook in the future.

## II. VERSATILE PROPERTIES

### A. Mechanical properties

Since the extraordinary mechanical properties of graphene (103 GPa of the in-plane stiffness and nearly 1 TPa of the elastic modulus [50]), 2D materials with excellent mechanical properties have attracted great attentions. As for  $\text{MoSi}_2\text{N}_4$ , its experimentally measured tensile strength ( $E$ ) and elastic modulus ( $Y$ ) are  $65.8 \pm 18.3$  GPa and  $491.4 \pm 139.1$  GPa [28], respectively, which are nearly half of those in graphene and higher than those in most 2D TMDs (e.g., 22 GPa and  $270 \pm 100$  GPa of  $\text{MoS}_2$ ) [3, 51, 52], MXene (e.g., 17 GPa and 333 GPa of  $\text{Ti}_3\text{C}_2\text{T}_x$  [53], 26 GPa and 386 GPa of  $\text{Nb}_4\text{C}_3\text{T}_x$  [54]), and black phosphorene [55] (18 GPa and 166 GPa). In detail, Ren et al. [28] measured the mechanical properties of monolayer  $\text{MoSi}_2\text{N}_4$  via atomic force microscopy nanoindentation (Fig. 2(a)). With a diamond tip of 11.1 nm, the indentation of hole is about 23 nm. The elastic behavior of monolayer  $\text{MoSi}_2\text{N}_4$  is demonstrated due to the well fitting force-displacement curves of loading and unloading states. Theoretical prediction of mechanical properties of 2D materials is mainly based

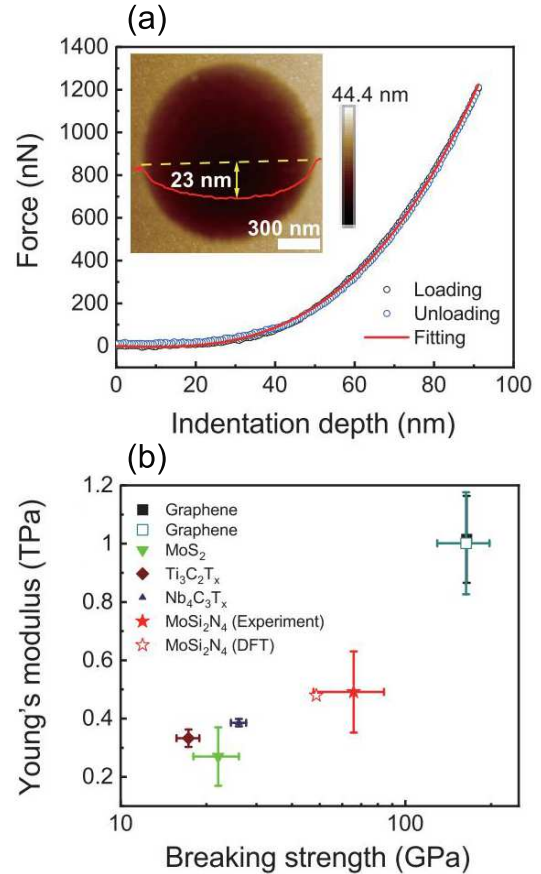


FIG. 2. (a) Force-displacement curve of monolayer  $\text{MoSi}_2\text{N}_4$  by atomic force microscopy nanoindentation, inset: the nanoindentation profile of suspended  $\text{MoSi}_2\text{N}_4$ . (b) Mechanical properties of  $\text{MoSi}_2\text{N}_4$  and other 2D materials. [28]

on the linear elastic model. The theoretically calculated tensile strength and elastic modulus are 48.3–57.8 GPa and 479.1–487.0 GPa, respectively [47, 56, 57], in good agreement with experimental values.

Actually, the critical strain and ideal tensile stress of 2D materials are vital indicators for practical applications, which depend on the elastic limit and lattice vibration [58]. Li et al. [56] focused on the elastic limit and failure mechanism of monolayer  $\text{MoSi}_2\text{N}_4$ . Under biaxial and uniaxial (zigzag or armchair) strains, the ideal strengths of monolayer  $\text{MoSi}_2\text{N}_4$  are similar, about 50 GPa, while the corresponding critical strain is 19.5% (biaxial strain), 26.5% (zigzag strain) and 17.5% (armchair strain). In Fig. 3, when the strains are below 20% ( $\epsilon < 20\%$ ), the tensile stresses ( $\sigma$ ) are in the order of  $\sigma_{\text{bi}} > \sigma_{\text{arm}} > \sigma_{\text{zig}}$ . There exists an obvious yield phenomenon under biaxial and armchair strains when  $\epsilon \geq 20\%$ , but the yield limit under a zigzag strain is about 25%. By fitting the initial strain-stress curve based on the linear regression up to 1% strain (the inset of Fig. 3(a)), the elastic moduli are calculated as  $E_{\text{zig}} = 448.3 \pm 5.1$  GPa and  $E_{\text{arm}} = 457.8 \pm 3.9$  GPa, which are more than

TABLE I. Structures and properties of semiconductors in  $\text{MA}_2\text{Z}_4$  family: lattice constants ( $a$ ), bandgap ( $E_g^{\text{PBE}}$  for PBE and  $E_g^{\text{HSE}}$  for HSE), carrier mobility ( $\mu_e$  for electron and  $\mu_h$  for holes), elastic modulus ( $Y$ ), tensile strength ( $E$ ), Poisson's ratio ( $\nu$ ), thermal conductivity ( $\kappa$ ). [28, 29, 47–49]

Struc.	Phase	$a$ (Å)	$E_g^{\text{PBE}}$ (eV)	$E_g^{\text{HSE}}$ (eV)	$\mu_e$ ( $\text{cm}^2\text{V}^{-1}\text{s}^{-1}$ )	$\mu_h$ ( $\text{cm}^2\text{V}^{-1}\text{s}^{-1}$ )	$Y$	$E$ (GPa)	$\nu$	$\kappa$ ( $\text{Wm}^{-1}\text{K}^{-1}$ )
$\text{MoSi}_2\text{N}_4$	$\alpha_1$	2.91	1.74( $\Gamma$ -K)	2.31( $\Gamma$ -K)	200	1000	$491.4 \pm 139.1$ GPa	65.8±18.3	0.28	417–439
$\text{MoSi}_2\text{P}_4$	$\alpha_1$	3.47	0.70(K-K)	0.99(K-K)	246–258	1065–1429	159 GPa	17.5–21.2	*	116–122
	$\alpha_2$	3.46	0.91(K-K)	1.19(K-K)	*	*	*	*	*	*
$\text{MoSi}_2\text{As}_4$	$\alpha_1$	3.62	0.56(K-K)	0.98(K-K)	*	*	*	*	*	46
	$\alpha_2$	3.61	0.74(K-K)	1.02(K-K)	*	*	*	*	*	*
$\text{MoGe}_2\text{N}_4$	$\alpha_1$	3.02–3.04	0.91–0.99( $\Gamma$ K-K)	1.27–1.38( $\Gamma$ K-K)	490	2190	362 GPa	40.3–42.1	*	286
$\text{MoGe}_2\text{P}_4$	$\alpha_1$	3.55	0.04( $\Gamma$ -K)	0.84( $\Gamma$ -K)	*	*	139 GPa	15.3–18.4	*	63
	$\alpha_2$	3.53	0.56(K-K)	0.95(K-K)	*	*	*	*	*	*
$\text{MoGe}_2\text{As}_4$	$\alpha_2$	3.69	0.47(K-K)	0.83( $\Gamma$ K-K)	*	*	*	*	*	*
$\text{WSi}_2\text{N}_4$	$\alpha_1$	2.91	2.08( $\Gamma$ -K)	2.57–2.66( $\Gamma$ -K)	320	2026	506 GPa	55.5–59.2	0.27	401–503
$\text{WSi}_2\text{P}_4$	$\alpha_1$	3.48	0.53(K-K)	0.81(K-K)	*	*	167 GPa	18.8–22.0	*	129
	$\alpha_2$	3.46	0.86(K-K)	1.11(K-K)	*	*	*	*	*	*
$\text{WSi}_2\text{As}_4$	$\alpha_2$	3.61	0.71(K-K)	0.95(K-K)	*	*	*	*	*	*
$\text{WGe}_2\text{N}_4$	$\alpha_1$	3.02	1.15–1.29( $\Gamma$ K-K)	1.51–1.69( $\Gamma$ K-K)	690	2490	384 GPa	42.6–44.5	*	322
$\text{WGe}_2\text{P}_4$	$\alpha_1$	3.55	0.48(K-K)	0.73(K-K)	*	*	145 GPa	16.5–19.3	*	64
	$\alpha_2$	3.54	0.63( $\Gamma$ K-K)	0.89(K-K)	*	*	*	*	*	*
$\text{WGe}_2\text{As}_4$	$\alpha_2$	3.69	0.50( $\Gamma$ K- $\Gamma$ K)	0.78(K-K)	*	*	*	*	*	*
$\text{CrSi}_2\text{N}_4$	$\alpha_1$	2.84	0.49( $\Gamma$ -K)	0.94(K-K)	*	*	468 GPa	55.4–57.8	*	332–348
$\text{CrSi}_2\text{P}_4$	$\alpha_1$	3.42	0.28(K-K)	0.64(K-K)	*	*	154 GPa	18.5–21.2	*	120
	$\alpha_2$	3.41	0.34( $\Gamma$ K-K)	0.65(K-K)	*	*	*	*	*	*
$\text{CrGe}_2\text{N}_4$	$\alpha_1$	2.98	0.49( $\Gamma$ -K)	0.31( $\Gamma$ -K)	*	*	340 GPa	38.1–38.7	*	198
$\text{CrGe}_2\text{P}_4$	$\alpha_2$	3.49	0.04( $\Gamma$ K-K)	0.36( $\Gamma$ K-K)	*	*	*	*	*	*
$\text{TiSi}_2\text{N}_4$	$\alpha_1$	2.93	1.57( $\Gamma$ M-M)	2.50( $\Gamma$ M-M)	*	*	*	*	*	107
$\text{ZrSi}_2\text{N}_4$	$\alpha_1$	3.04	1.55( $\Gamma$ M-M)	2.41( $\Gamma$ M-M)	*	*	382 N/m	*	0.32	82
	$\beta_2$	3.05	1.00( $\Gamma$ -M)	0.36( $\Gamma$ -M)	*	*	400 N/m	*	0.26	*
$\text{ZrGe}_2\text{N}_4$	$\beta_2$	3.19	1.04( $\Gamma$ - $\Gamma$ )	2.34( $\Gamma$ - $\Gamma$ )	*	*	*	*	*	*
$\text{HfSi}_2\text{N}_4$	$\alpha_1$	3.02	1.80( $\Gamma$ M-M)	2.70( $\Gamma$ M-M)	*	*	406 N/m	*	0.32	124
	$\beta_2$	3.04	1.21( $\Gamma$ -M)	2.21( $\Gamma$ -M)	*	*	420 N/m	*	0.25	*
$\text{HfGe}_2\text{N}_4$	$\beta_2$	3.18	1.15( $\Gamma$ - $\Gamma$ )	2.45( $\Gamma$ - $\Gamma$ )	*	*	*	*	*	*
$\text{PdSi}_2\text{N}_4$	$\beta_2$	2.99	2.50( $\Gamma$ -M)	3.80( $\Gamma$ -M)	*	*	356 N/m	*	0.29	*
$\text{PtSi}_2\text{N}_4$	$\beta_2$	3.02	2.50( $\Gamma$ -M)	3.80( $\Gamma$ -M)	*	*	349 N/m	*	0.30	*

twice those of  $\text{MoS}_2$  ( $E_{\text{zig}} = 197.9 \pm 4.3$  GPa and  $E_{\text{arm}} = 200 \pm 3.7$  GPa) [59]. The degeneracy of elastic moduli indicate a nearly elastic isotropy in monolayer  $\text{MoSi}_2\text{N}_4$ . On the other hand, the failure mechanism has been investigated on the aspect of lattice stability by phonon dispersion. When the tensile strength limit is reached under an armchair strain, the phonon dispersion

has no imaginary frequency. This indicates lattice stability and further reveals that the failure phenomenon of monolayer  $\text{MoSi}_2\text{N}_4$  is ascribed to the elastic failure of the SiN layer before reaching the critical strain. The obvious imaginary frequency of out-of-plane acoustic branch (ZA) before reaching tensile strength limit demonstrates that the failure mechanism of monolayer  $\text{MoSi}_2\text{N}_4$  is at-

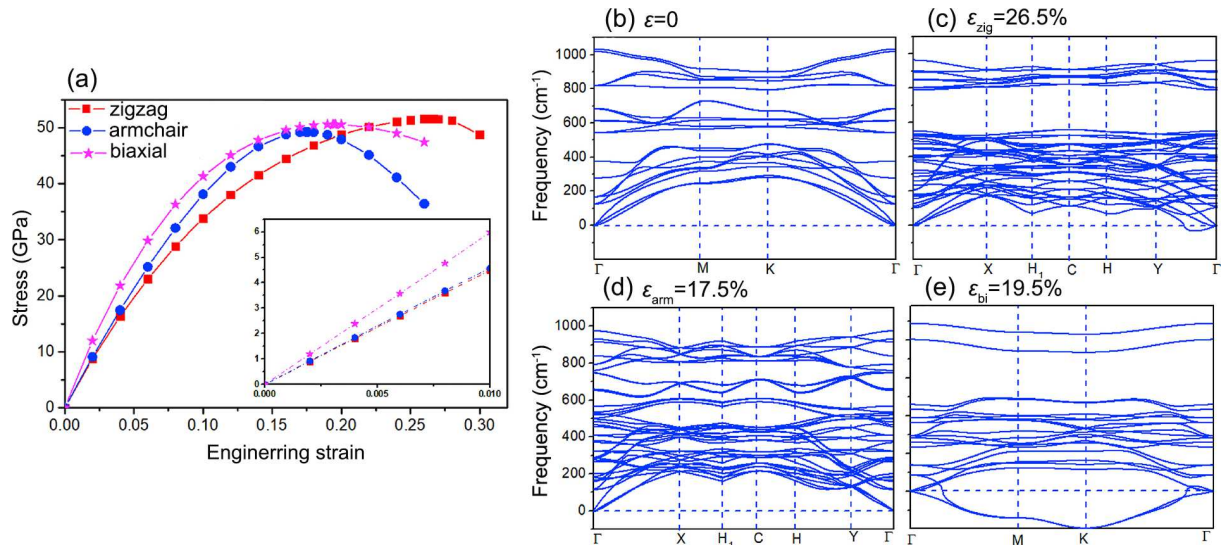


FIG. 3. (a) Strain-stress curve of monolayer  $\text{MoSi}_2\text{N}_4$  and the corresponding phonon dispersion under different strains: (b) no strain, (c) zigzag uniaxial strain  $\epsilon_{\text{zig}} = 26.5\%$ , (d) armchair uniaxial strain  $\epsilon_{\text{arm}} = 17.5\%$ , (e) biaxial strain  $\epsilon_{\text{bi}} = 19.5\%$ . [56]

tributed to phonon instability under the zigzag or biaxial strains.

The mechanical parameters of other members in  $\text{MA}_2\text{Z}_4$  family are listed in Table 2. Mortazavi et al. [47] found in  $\text{MA}_2\text{Z}_4$  family the mechanical properties are mainly affected by the terminating atom (Z-site) rather than the core atom (M-site). Three possible factors that influence the mechanical properties are proposed: Z-site atomic mass, structure and chemical bonds. Firstly, increasing Z-site atomic weight deteriorates the mechanical properties, but the elastic modulus has little change when M-site atomic mass is increased. For examples,  $\text{MA}_2\text{N}_4$  has higher  $Y$  and  $E$  than  $\text{MA}_2\text{P}_4$ , while  $Y$  and  $E$  of  $\text{MoSi}_2\text{N}_4$  and  $\text{WSi}_2\text{N}_4$  are close. Secondly, since the M-A bonds are absolutely vertical, only M-Z and A-Z bonds participate in the deformation when applying an in-plane loading, indicating that the two bonds related to Z-site atoms determine the mechanical properties. Besides, chemical bonds formed with N atoms are always stronger than those with P/As atoms. Bonds formed with Si are sturdier than those with Ge, resulting in the highest elastic modulus of monolayer  $\text{MSi}_2\text{N}_4$ .

The mechanical properties of some other  $\text{MA}_2\text{Z}_4$ -derived materials have also been investigated, e.g.,  $\text{CrC}_2\text{N}_4$ ,  $\text{SnSi}_2\text{N}_4$ ,  $\text{SnGe}_2\text{N}_4$  and  $\text{XMoSiN}_2$  ( $\text{X} = \text{S}/\text{Se}/\text{Te}$ ) [60–63]. The predicted elastic modulus and tensile strength of  $\text{CrC}_2\text{N}_4$  are as high as 676 and 54.8 GPa, respectively, while those of  $\text{SnSi}_2\text{N}_4$  (478 and 47 GPa) are close to those of  $\text{MoSi}_2\text{N}_4$ . This indicates that the  $\text{MA}_2\text{Z}_4$  structure offers excellent mechanical features, but the intrinsic mechanisms related to the elements and structures require further studies.

## B. Piezoelectricity, ferroelectricity and flexoelectricity

Piezoelectricity of 2D materials can convert mechanical energy into electrical energy and *vice versa*, which always occurs in semiconductors or insulators with broken inversion symmetry. The relax-ion piezoelectric coefficients ( $e_{ijk}$  and  $d_{ijk}$ ) are expressed as

$$e_{ijk} = \frac{\partial P_i}{\partial \epsilon_{jk}} = e_{ijk}^{\text{elc}} + e_{ijk}^{\text{ion}} \quad (1)$$

and

$$d_{ijk} = \frac{\partial P_i}{\partial \sigma_{jk}} = d_{ijk}^{\text{elc}} + d_{ijk}^{\text{ion}} \quad (2)$$

where  $P_i$ ,  $\epsilon_{jk}$ ,  $\sigma_{jk}$  are polarization vector, strain and stress. The subscript *elc* or *ion* represent the electronic or ionic contributions. The relationship between  $d_{ijk}$  and  $e_{ijk}$  is built via elastic tensor ( $C_{ij}$ , with the Voigt notation). The independent parameters of tensor are reduced due to the symmetry of crystal structure. In monolayer  $\text{MA}_2\text{Z}_4$ , the counterpart with  $\text{P}\bar{6}m2$  space group prohibits the out-of-plane piezoelectric effect, so that only the in-plane piezoelectric strain and stress coefficients (i.e.,  $e_{11}$ ,  $d_{11}$ ) and elastic coefficients (i.e.,  $C_{11}$ ,  $C_{12}$ ) are considered [64, 65].

Structure effect on piezoelectricity of  $\text{MA}_2\text{Z}_4$  has been investigated [64]. The structures are divided into six configurations by different operations (translation, mirror and rotation) of  $\text{A}_2\text{Z}_2$  layers, which are nominated as  $\alpha_i$  ( $i = 1\text{--}6$ ), as shown in Fig. 4(a). It is observed that the values of  $C_{11} - C_{12}$  of  $\text{MSi}_2\text{N}_4$  ( $\text{M} = \text{Mo}, \text{W}$ ) are close when  $i = 1, 2, 4, 5$ , while those of  $C_{11} - C_{12}$  are higher when  $i = 3, 6$ , indicating  $\alpha_3$  and  $\alpha_6$   $\text{MSi}_2\text{N}_4$  ( $\text{M} = \text{Mo}/\text{W}$ ) with high resistance to deformation. The

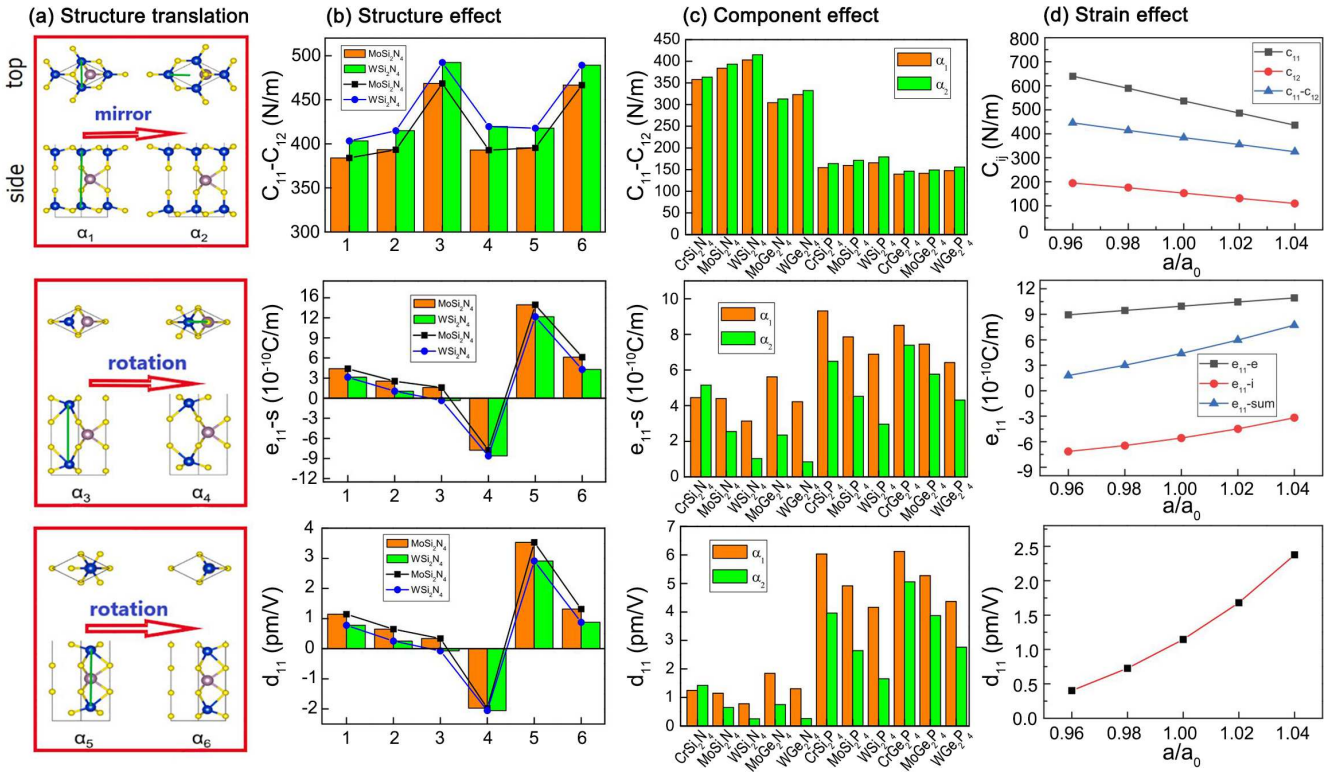


FIG. 4. (a) Structure translation of  $\alpha_i\text{-MA}_2\text{Z}_4$  ( $i = 1\text{-}6$ ). (b-d) Structure, component and strain effects on piezoelectric parameters. [64, 65]

structural sensibility of  $d_{11}$  is homologous with that of  $e_{11}$  from  $\alpha_1$  to  $\alpha_6$ .  $e_{11}$  of  $\alpha_5$  exhibits the largest value among six structures, which is  $13.95 \times 10^{-10} \text{ C/m}$  for  $\text{MoSi}_2\text{N}_4$  and  $12.17 \times 10^{-10} \text{ C/m}$  for  $\text{WSi}_2\text{N}_4$ .  $d_{11}$  of  $\alpha_5\text{-MoSi}_2\text{N}_4$  and  $\alpha_5\text{-WSi}_2\text{N}_4$  is 3.53 and 2.91 pm/V, respectively.  $d_{11}$  of  $\alpha_1\text{-MoSi}_2\text{N}_4$  and  $\alpha_1\text{-WSi}_2\text{N}_4$  (experimentally synthesized phases) is 1.15 and 0.78 pm/V, respectively.

Studies on the influence of different M/A/Z atoms reveal that  $C_{11} - C_{12}$  of both  $\alpha_1$  and  $\alpha_2$  improves with the element periodicity increasing (Fig. 4(c)). For instance,  $C_{11} - C_{12}$  of  $\text{MSi}_2\text{N}_4$  is in the order of  $\text{CrSi}_2\text{N}_4\text{-MoSi}_2\text{N}_4\text{-WSi}_2\text{N}_4$ . The larger elastic constants of  $\text{MA}_2\text{N}_4$ , compared with those of  $\text{MA}_2\text{P}_4$  and other 2D materials (e.g., TMDs, metal oxides, and III-V semiconductors [66, 67]), indicate that  $\text{MA}_2\text{N}_4$  system is more rigid. The change trend of  $e_{11}$  and  $d_{11}$  follows the opposite regularity, compared with elastic coefficients.  $d_{11}$  of  $\text{MA}_2\text{P}_4$  with the same M and A atoms is larger than that of  $\text{MA}_2\text{N}_4$  for both  $\alpha_1$  and  $\alpha_2$  phases.  $d_{11}$  of  $\alpha_1\text{-}$  and  $\alpha_2\text{-MA}_2\text{Z}_4$  is in the range of 0.78–6.12 pm/V and 0.25–5.06 pm/V, respectively. Monolayer  $\text{MA}_2\text{P}_4$  nanosheets (e.g.,  $\alpha_1\text{-CrSi}_2\text{P}_4$ ,  $\alpha_1\text{-MoSi}_2\text{P}_4$ ,  $\alpha_1\text{-CrGe}_2\text{P}_4$ ,  $\alpha_1\text{-MoGe}_2\text{P}_4$  and  $\alpha_2\text{-CrGe}_2\text{P}_4$ ) show excellent piezoelectric response. In addition, the effect of A-site atoms on piezoelectric performance can be ignored so that  $d_{11}$  of  $\text{MoGe}_2\text{N}_4$  is close to that of  $\text{MoSi}_2\text{N}_4$ .  $d_{11}$  of most monolayer  $\text{MA}_2\text{P}_4$  nanosheets is even larger than that of 2D TMDs (e.g.,  $d_{11} = 3.65 \text{ pm/V}$  of  $\text{MoS}_2$ ,  $d_{11} = 2.12 \text{ pm/V}$

of  $\text{WS}_2$ ,  $d_{11} = 4.55 \text{ pm/V}$  of  $\text{MoS}_2$ , and  $d_{11} = 2.64 \text{ pm/V}$  of  $\text{WSe}_2$ ) [68] and  $d_{33}$  (3.1 pm/V) of bulk piezoelectric wurtzite GaN [69].

The compressive and tensile biaxial strain are shown to obviously improve and deteriorate the piezoelectric performance of  $\text{MoSi}_2\text{N}_4$ , respectively (Fig. 4(d)) [65]. Piezoelectric stress and strain responses are improved with the in-plane strain from -4% to 4%.  $d_{11}$  can be enhanced by 107% if a tensile biaxial strain of 4% is applied.  $\text{VSi}_2\text{P}_4$ , a spin-gapless semiconductor (SGS), possesses a wide range of properties due to its strain sensitivity. With the increasing strain, it presents as ferromagnetic metal (FMM), SGS, ferromagnetic semiconductor (FMS), or ferromagnetic half-metal (FMHM) [70]. In the strain range of 1%–4%, the coexistence of ferromagnetism and piezoelectricity can be achieved in FMS  $\text{VSi}_2\text{P}_4$ . Its  $d_{11}$  under 1%, 2% and 3% strain is 4.61, 4.94 and 5.27 pm/V, respectively.

There exist both in-plane and out-of-plane piezoelectric polarizations in Janus  $\text{MSiGeN}_4$  (M = Mo/W) owing to the broken reflection symmetry along the out-of-plane direction [71, 72]. The in-plane piezoelectric coefficients of Janus  $\text{MSiGeN}_4$  ( $d_{11} = 1.494 \text{ pm/V}$  for  $\text{MoSiGeN}_4$ ,  $d_{11} = 1.050 \text{ pm/V}$  for  $\text{WSiGeN}_4$ ) are between those of  $\text{MSi}_2\text{N}_4$  and  $\text{MGe}_2\text{N}_4$ , while the out-of-plane stress piezoelectric coefficients ( $d_{31}$ ) are -0.014 and 0.011 pm/V for  $\text{MoSiGeN}_4$  and  $\text{WSiGeN}_4$ , respectively. Under an in-plane biaxial strain,  $d_{11}$  of  $\text{MSiGeN}_4$  is improved with

the increasing  $e_{11}$ , which is similar with  $MA_2N_4$ . A tensile strain of 10% can increase  $d_{11}$  of  $MoSiGeN_4$  and  $WSiGeN_4$  by several times, with the values up to 8.081 and 7.282 pm/V, respectively. On the contrary, a compressive biaxial strain can effectively enhance the out-of-plane piezoelectric response. The  $MA_2Z_4$ -derived  $SrAlGaSe_4$  has both in-plane ( $d_{11} = -1.865$  pm/V) and out-of-plane ( $d_{31} = -0.068$  pm/V) piezoelectricity under uniaxial a tensile strain of 6% [73].

In addition to piezoelectricity, the intrinsic ferroelectricity and its electrical switching in  $MA_2Z_4$  are still open issues. For example, the sliding ferroelectricity is found in vdW  $MoA_2N_4$  bilayer and multilayer [74]. The interlayer inequivalence caused by the stacking order directly generates the out-of-plane polarization. Then, the induced vertical polarization can be switched via the interlayer sliding. The calculated vertical polarization is 3.36, 3.05, 2.49 and 3.44 pC/m for AB stacking bilayer  $MoSi_2N_4$ ,  $MoGe_2N_4$ ,  $CrSi_2N_4$  and  $WSi_2N_4$ , respectively, which are higher than that of bilayer  $WTe_2$  and BN [75, 76].

The flexoelectricity of monolayer  $MA_2Z_4$  is also of interest, which is often induced by bending deformation of 2D materials with a strain gradient [47]. The out-of-plane bending flexoelectric coefficients of 12 kinds of  $MA_2Z_4$  ( $M = Mo/Cr/W$ ,  $A = Si/Ge$ ,  $Z = N/P$ ) are found in the range of 0.001–0.047 nC/m under a bending strain gradient of 0.3/Å. The highest flexoelectric coefficient of  $WGe_2N_4$  is about 1.5 times higher than that of  $MoS_2$  [77]. It is proposed that the enhancement of flexoelectricity is insufficient with the bending deformation, but is broadened by the construction of asymmetry structures (e.g., Janus counterparts) [78, 79].

### C. Thermal conductivity

Owing to the high tensile strength and thus strong bond interactions, the thermal conductivity of monolayer  $MA_2Z_4$  family has attracted attentions. Based on thermal Boltzmann transport equations, the theoretical lattice thermal conductivity ( $\kappa$ ) of  $MoSi_2N_4$  is predicted as high as  $400 \text{ Wm}^{-1}\text{K}^{-1}$  at room temperature [47, 49, 80, 81], which is larger than that of most other 2D materials, such as hydrogenated borophene ( $368 \text{ Wm}^{-1}\text{K}^{-1}$ ) [82], TMDs ( $23$ – $142 \text{ Wm}^{-1}\text{K}^{-1}$ ) [83–85], group IVA and VIA compounds ( $0.26$ – $9.8 \text{ Wm}^{-1}\text{K}^{-1}$ ) [86, 87]. But it is lower than that of graphene ( $3000$ – $5000 \text{ Wm}^{-1}\text{K}^{-1}$ ) [88, 89], and h-BNs ( $600 \text{ Wm}^{-1}\text{K}^{-1}$ ) [90]. Such high thermal conductivity of monolayer  $MoSi_2N_4$  is promising for heat conductors and thermal management in semiconductor devices.

In Slack's classic rules [91, 92], crystals with high thermal conductivity follows four rules: simple crystal structure, light atomic masses, strong bonding and low anharmonicity. In the monolayer  $MA_2Z_4$  family, by replacing M/A/Z atoms at different sites, the different contributions to  $\kappa$  have been further examined [47, 49]. It is found that when Z- site atoms are replaced,  $\kappa$

of monolayer  $MA_2Z_4$  obeys the Slack's rules (red lines in Fig. 5(a)). For instance,  $\kappa$  of  $MoSi_2Z_4$  decreases by one order of magnitude from  $Z = N$  to  $As$ , indicating that Z atom plays a critical role in controlling the thermal conductivity of  $MoSi_2Z_4$ . The similar variation phenomena are found in  $MoGe_2Z_4$  and  $WGe_2Z_4$  as well. Meanwhile, in A-site-replaced  $MA_2Z_4$ ,  $\kappa$  is decreased by about 40.3%–50.4% from  $A = Si$  to  $Ge$ .  $\kappa$  of  $MoGe_2N_4$  ( $286 \text{ Wm}^{-1}\text{K}^{-1}$ ) is about 40.3% lower than that of  $MoSi_2N_4$  ( $439 \text{ Wm}^{-1}\text{K}^{-1}$ ).  $\kappa$  of  $WGe_2P_4$  ( $64 \text{ Wm}^{-1}\text{K}^{-1}$ ) is only half that of  $WSi_2P_4$  ( $129 \text{ Wm}^{-1}\text{K}^{-1}$ ). The decreasing phenomena are intrinsically attributed to the phonon properties. The Z- or A-site atoms of  $MA_2Z_4$  determine the phonon frequency range. Monolayer  $MA_2N_4$  shows wider frequency range than  $MA_2P_4$  and  $MA_2As_4$  (Fig. 5(b)).  $MSi_2Z_4$  exhibits wider phonon dispersion than  $MGe_2Z_4$ . Thermal conductivity is related to the phonon group velocity that directly depends on phonon branches. Thus, wider phonon bands lead to higher phonon group velocity and result in higher thermal conduction.

When M atoms are from different group IVB or VIB atoms, the variation of  $\kappa$  is abnormal and the conventional guideline for searching high  $\kappa$  does not work.  $\kappa$  exhibits an irregular oscillation with the increasing atomic mass and decreasing Debye temperature (green dash lines in Fig. 5(a)). Mortazavi et al. proposed that the weight of core atoms is the dominant factor on thermal conduction of  $MA_2Z_4$  and  $\kappa$  increases with the weight of core atoms. This violates the Slack's rules but is consistent with the classical theory that stiffer systems favor a higher  $\kappa$ . However, in our recent work [49], we found that the influential factors on the variation of  $\kappa$  is not limited to the atomic mass. For instance, the average mass of  $WSi_2N_4$  is 1.5 times that of  $CrSi_2N_4$ , but  $\kappa$  shows only 13% difference. We proposed that the abnormal thermal conductivity of M-site replaced  $MA_2Z_4$  is relative to the group that M atoms belong to.  $\kappa$  of  $MA_2Z_4$  with group VIB M atom is about 3–4 times of that with group IVB M atom. These abnormal phenomena with respect to M atoms are attributed to the fundamental vibrational properties and phonon scattering behavior. The acoustic branches of  $MA_2Z_4$  with group VIB M are more bunched and less flattened. Consequently, the phonon scattering rates (Fig. 5(c)) of group VIB M-site  $MA_2Z_4$  are lower than that of group IVB M-site  $MA_2Z_4$ , and higher  $\kappa$  presents in the former. As shown in Fig. 5(d), the thermal conductivity of monolayer  $MA_2Z_4$  family is in a very wide range ( $10^1$ – $10^3 \text{ Wm}^{-1}\text{K}^{-1}$ ), locating between that of 2D TMDs and hBN.

### D. Thermoelectric properties

In addition to the thermal conductivity, the thermoelectric performance of monolayer  $MA_2Z_4$  has been also investigated. The dimensionless figure of merit ( $ZT$ ) is always used to measure the efficiency of thermoelec-

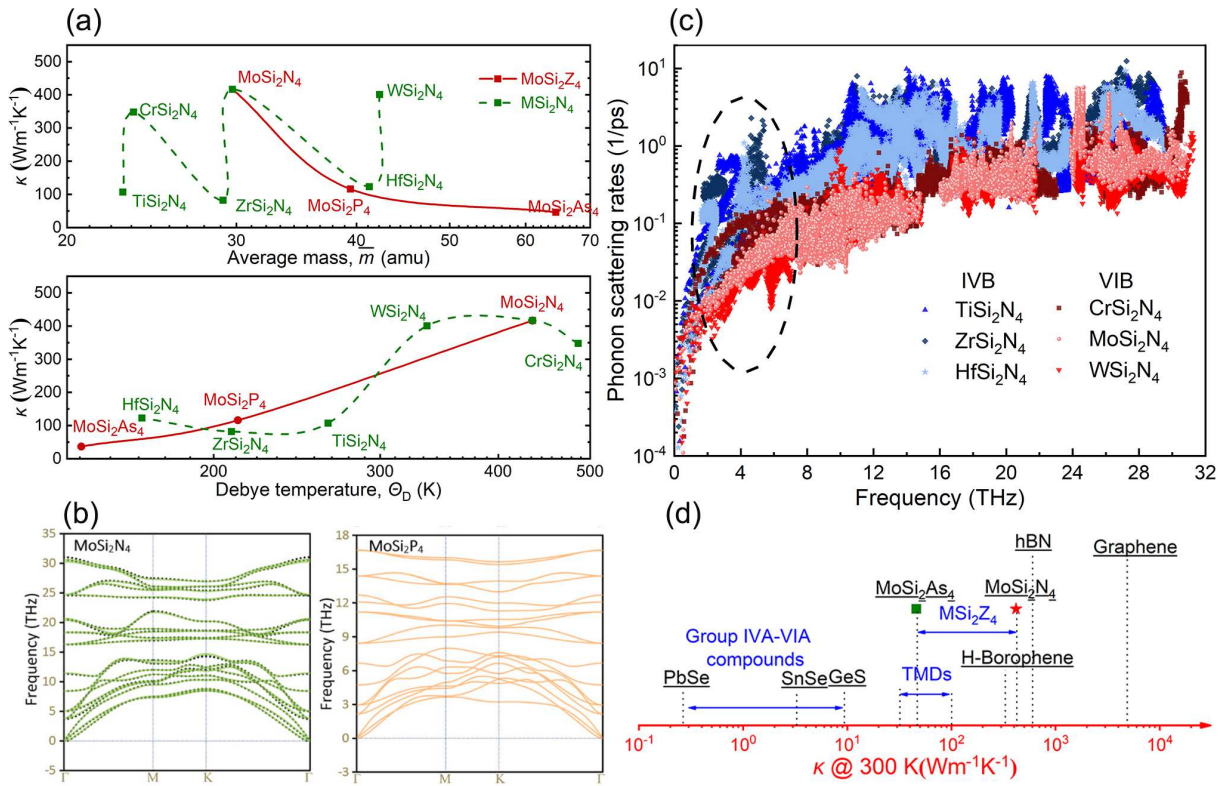


FIG. 5. (a) Thermal conductivity ( $\kappa$ ) as a function of average mass (upper) and Debye temperature (down). (b) Phonon dispersion of MoSi<sub>2</sub>N<sub>4</sub> and MoSi<sub>2</sub>P<sub>4</sub>, where the frequency range of MoSi<sub>2</sub>N<sub>4</sub> is wider than that of MoSi<sub>2</sub>P<sub>4</sub>. (c) Phonon scattering of MA<sub>2</sub>Z<sub>4</sub> with different M-site atoms, indicating that MA<sub>2</sub>Z<sub>4</sub> with group VIA atom has lower scattering rates. (d) Comparison of  $\kappa$  at 300 K between MA<sub>2</sub>Z<sub>4</sub> family and other 2D materials. [47, 49]

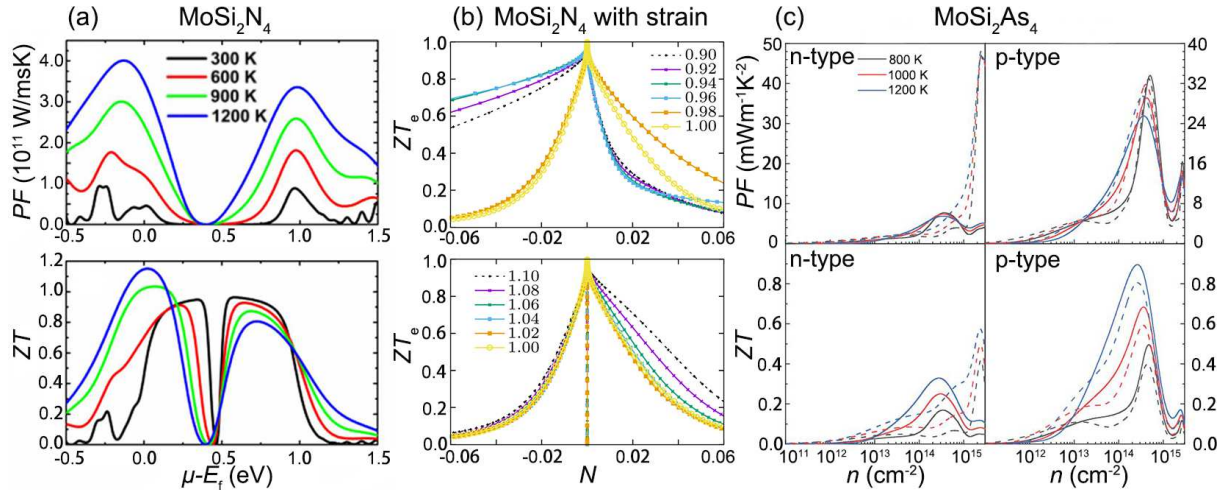


FIG. 6. (a) Thermoelectric performance of monolayer MoSi<sub>2</sub>N<sub>4</sub> at different temperatures: Power factor (PT) (top) and figure of merit (ZT) (bottom). (b) Effect of compressive (top) and tensile (bottom) strain on ZT. (c) Thermoelectric performance of monolayer MoSi<sub>2</sub>As<sub>4</sub>. [57, 93, 94]

tric conversion of a thermoelectric material, which is expressed as:

$$ZT = \frac{S^2 T}{\rho(\kappa_e + \kappa_l)} \quad (3)$$

where  $S$ ,  $1/\rho$ ,  $T$ ,  $\kappa_e$ , and  $\kappa_l$  are the Seebeck coefficient, electrical conductivity, working temperature, electronic thermal conductivity and lattice thermal conductivity, respectively. The higher  $ZT$  indicates the better heat-to-electricity conversion efficiency. Thus, 2D materials

for the thermoelectric field are prone to semiconductors with high Seebeck coefficient, electrical conductivity and low thermal conductivities.

The power factor ( $PF = S^2T/\rho$ ) of monolayer  $\text{MoSi}_2\text{N}_4$  is studied to evaluate the capability of producing electricity [57]. The heat conversion into electricity is favored by the temperature since  $PF$  increases considerably with temperature. The maximum  $PF$  is located at a chemical potential range of 0.12–0.98 eV (upper in Fig. 6(a)).  $PF$  in the negative chemical potential region is more sensitive to temperature than in the positive region. Meanwhile the maximum  $ZT$  increases with temperature in the chemical potential range of -0.45–0.5 eV. The maximum  $ZT$  of monolayer  $\text{MoSi}_2\text{N}_4$  is up to 1.2 at 1200 K [57], while  $ZT$  of  $\text{MoGe}_2\text{N}_4$  is up to 1.0 at 900 K [95]. Guo et al. [93] studied the effect of strain on the thermoelectric performance of monolayer  $\text{MoSi}_2\text{N}_4$ , as shown in Fig. 6(b). They found that the compressive strain rather than the tensile strain has significant effect on  $S$ . Besides,  $S$  with n-type doping has observable improvement under a compressive strain, which is ascribed to the strain-driven conduction band degeneracies.

As mentioned above, the high lattice thermal conductivity of monolayer  $\text{MoSi}_2\text{N}_4$  brings negative effect on  $ZT$  and further restrains the thermoelectric performance. It is imperative for seeking other  $\text{MA}_2\text{Z}_4$  semiconductors with low thermal conductivity to satisfy the requirement of high  $ZT$ . Monolayer  $\text{MoSi}_2\text{As}_4$  semiconductor has no doubt to be a good candidate due to its low lattice thermal conductivity. However, Huang et al. [94] found that  $ZT$  of  $\text{MoSi}_2\text{As}_4$  is 0.33 for n-type and 0.90 for p-type at 1200 K, which are even lower than that of  $\text{MoSi}_2\text{N}_4$  (Fig. 6(c)). The underlying reason still remains unknown. Hence, whether there is any member with ultra-high thermoelectric properties needs to be further explored.

### E. Electrical properties

Till now, nearly hundred members in monolayer  $\text{MA}_2\text{Z}_4$  family have been predicted. Wang et al. [29] systematically investigated 72 thermodynamically and dynamically stable  $\text{MA}_2\text{Z}_4$  compounds with a septuple-atomic-layer which possess the same intercalated architecture as  $\text{MoSi}_2\text{N}_4$ . The electric properties can be classified according to the total numbers of valence electrons. Most of monolayer  $\text{MA}_2\text{Z}_4$  nanosheets with 32 or 34 valence electrons are semiconductors, while those with 33 valence electrons are non-magnetic metals or ferromagnetic semiconductors. Ding et al. [98] identified 12 stable  $\text{MSi}_2\text{N}_4$  with trigonal prismatic (H-phase) or octahedral (T-phase) structures, including six new members. The M-site atoms contain both the early transition metal element (group IIIB–VIB) and the late transition metal (group VIIIB, e.g., Pd and Pt). Group IIIB and IVB  $\text{MSi}_2\text{N}_4$  with H- and T-phase geometries are all stable, while group VB and VIB ones are only stable with

H-phase. Moreover, other  $\text{MoSi}_2\text{N}_4$  derived structures have emerged in an overwhelming trend, such as, bilayer or multilayer  $\text{MA}_2\text{Z}_4$ , heterostructures, Janus  $\text{MA}_2\text{Z}_4$ , etc. These  $\text{MA}_2\text{Z}_4$  nanosheets exhibit versatile electronic properties depending on the number of valence electrons and structural phases. In this subsection, we emphatically discuss the intrinsic electrical properties of these monolayers and their tunability.

H-phase monolayer  $\text{MA}_2\text{Z}_4$  nanosheets, where  $\text{M} = \text{Cr}/\text{Mo}/\text{W}/\text{Ti}/\text{Zr}/\text{Hf}$ ,  $\text{A} = \text{Si}/\text{Ge}$ ,  $\text{Z} = \text{N}/\text{P}/\text{As}$ , are semiconductors with a bandgap around 0.04–1.79 eV (PBE) and 0.31–2.57 eV (HSE) calculated by DFT [47, 49]. Monolayer  $\text{MA}_2\text{N}_4$  nanosheets are indirect bandgap materials ( $\Gamma$ -K), while monolayer  $\text{MA}_2\text{P}_4$  nanosheets are direct gap semiconductors (K-K). The electronic contribution to CB and VB derived primarily from interior atomic orbitals leads to the robust band edge states [99]. From the projected band structure and charge density distribution (Fig. 7), valence band maximum (VBM) at  $\Gamma$  point is mainly contributed by  $\text{M}-d_{z^2}$  orbital and marginally contributed by  $\text{Z}-p_z$  and  $\text{A}-p_z$ , while at K point it is contributed by  $\text{M}-(d_{x^2-y^2}, d_{xy})$  and  $\text{Z}-(p_x, p_y, p_z)$  orbitals which locate at the centre area of the structure. Conduction band minimum (CBM) is solely occupied by  $\text{M}-(s, d_{z^2})$  orbitals. The strong interaction of  $d$  orbitals of M atom renders to the highly dispersion between VB and CB, indicating high charge carrier mobilities and small effective masses. The calculated electron and hole mobilities are 200 and  $1100 \text{ cm}^2\text{V}^{-1}\text{s}^{-1}$  for  $\text{MoSi}_2\text{N}_4$ , 490 and  $2190 \text{ cm}^2\text{V}^{-1}\text{s}^{-1}$  for  $\text{MoGe}_2\text{N}_4$ , 320 and  $2026 \text{ cm}^2\text{V}^{-1}\text{s}^{-1}$  for  $\text{WSi}_2\text{N}_4$ , 690 and  $2490 \text{ cm}^2\text{V}^{-1}\text{s}^{-1}$  for  $\text{WGe}_2\text{N}_4$  [47]. The carrier mobility ( $\mu$ ) of monolayer  $\text{MoSi}_2\text{P}_4$  is comparable with that of  $\text{MoSi}_2\text{N}_4$ , where  $\mu$  in zigzag (armchair) direction is 245.992 (257.985)  $\text{cm}^2\text{V}^{-1}\text{s}^{-1}$  for electrons and 1065.023 (1428.885)  $\text{cm}^2\text{V}^{-1}\text{s}^{-1}$  for holes [48], which are much higher than those of  $\text{MoS}_2$  (72.16 and  $200.52 \text{ cm}^2\text{V}^{-1}\text{s}^{-1}$  [100]). Besides,  $\text{SnGe}_2\text{N}_4$  [62], a  $\text{MA}_2\text{Z}_4$ -derived structure without transition metals, possesses a high electron mobility of  $1061.66 \text{ cm}^2\text{V}^{-1}\text{s}^{-1}$ , but a low hole mobility of  $28.35 \text{ cm}^2\text{V}^{-1}\text{s}^{-1}$ , owing to a strongly concave downward conduction band and a flat valence band.

The bandgap of bilayer  $\text{MoSi}_2\text{Z}_4$  ( $\text{Z} = \text{P}/\text{As}$ ) is similar with that of monolayers due to the weak vdW interaction between layers. In terms of carrier mobilities, there exist several interesting phenomena [101]. (1) In monolayer and bilayer  $\text{MoSi}_2\text{Z}_4$ , the hole carrier mobilities are about 3–4 times larger than those of electrons. The difference of carrier mobilities effectively facilitates the spatial separation of electrons and holes, restraining the recombination probability of photo-excited carriers. (2) Carrier mobility of bilayer  $\text{MoSi}_2\text{Z}_4$ , especially hole carrier mobility, exhibits anisotropic behaviors. (3) the carrier mobilities (electron and hole) of bilayer  $\text{MoSi}_2\text{Z}_4$  are about 2 times that of monolayer  $\text{MoSi}_2\text{Z}_4$ . Monolayer and bilayer  $\text{MoSi}_2\text{Z}_4$  with high carrier mobilities exhibit pronounced carrier polarization and are promis-

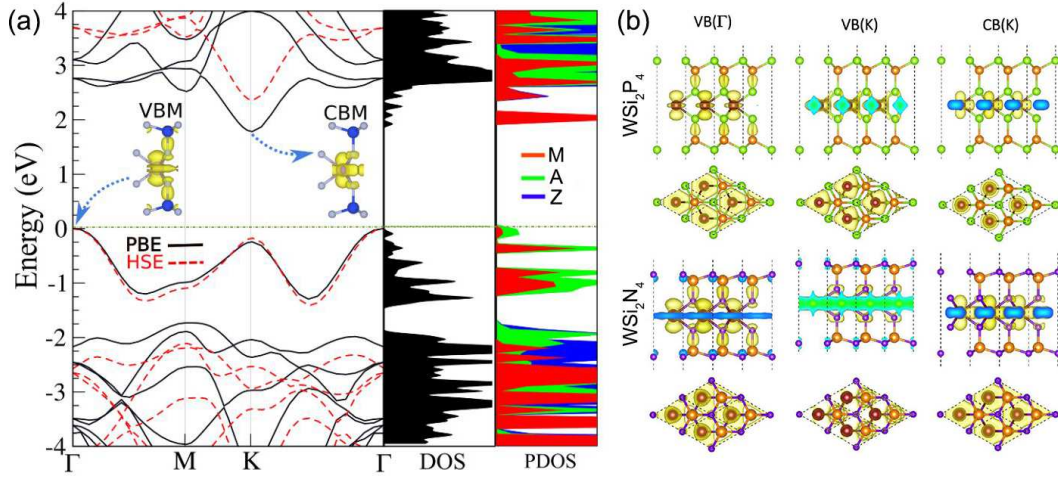


FIG. 7. (a) Band structure of monolayer  $\text{MoSi}_2\text{N}_4$ . (b) Charge density distribution of  $\text{WSi}_2\text{P}_4$  and  $\text{WSi}_2\text{N}_4$  at  $\text{VB}(\Gamma)$ ,  $\text{VB}(K)$  and  $\text{CB}(K)$  with the isosurface value as  $0.01 \text{ e}/\text{\AA}^3$ . [47, 57]

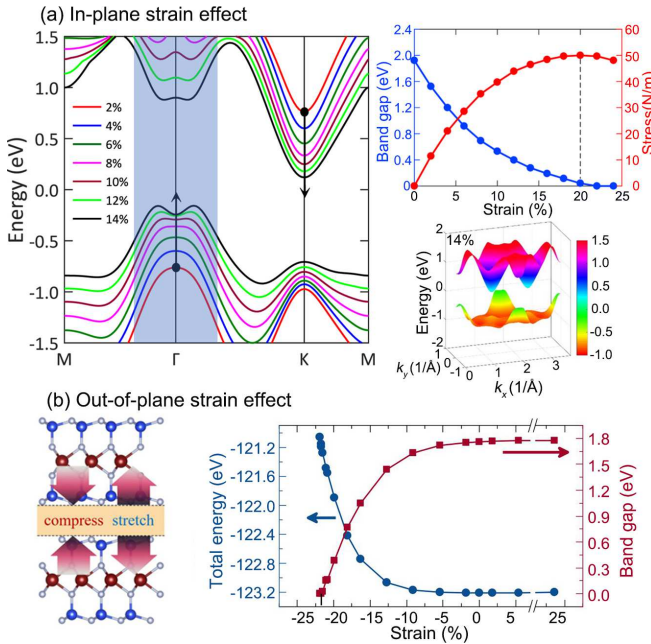


FIG. 8. (a) In-plane strain effect on monolayer  $\text{MoSi}_2\text{N}_4$ : variation of band structure (left), bandgap and stress versus strain (top right), and 3D ‘Mexican hat’ band under a tensile strain of 14% (bottom right). (b) Out-of-plane strain effect on bilayer  $\text{MoSi}_2\text{N}_4$ . [96, 97]

ing materials for high-performance nanoscale electronic and optoelectronic devices.

The electronic transition of monolayer  $\text{MA}_2\text{Z}_4$  from semiconductor to metal can be triggered by applying in-plane strains [48, 96]. The bandgap of monolayer  $\text{MoSi}_2\text{N}_4$  decreases with the increasing in-plane biaxial strain (Fig. 8(a)). The relation between bandgap ( $E_g$ ) and strain ( $\epsilon$ ) is fitted as [96]  $E_g = 0.004 \epsilon^2 - 0.17 \epsilon + 1.87$ . Under an in-plane biaxial strain of 4% (6%), the ef-

fective mass of holes is  $-2.33 m_e$  ( $-3.84 m_e$ ) and the effective mass of electrons is  $0.48 m_e$  ( $0.43 m_e$ ). This suggests that the in-plane biaxial strain simultaneously enhances the localization of holes and free electrons, which would achieve fascinating features like ferromagnetism and superconductivity. When the in-plane strain is over 10%, there exists an inversion at the edge of VBM, known as a ‘Mexican hat’ in which two VBMs are induced and the transport properties would be improved. As the strain increases, the variation of ‘Mexican hat’ dispersion is more noticeable. When  $\epsilon = 20\%$ ,  $\text{MoSi}_2\text{N}_4$  becomes semimetal. For  $\text{MoSi}_2\text{P}_4$  under an in-plane armchair uniaxial strain, the bandgap transfers to be indirect at  $\epsilon = 2\%$ , 3% and returns to be direct at  $\epsilon = -10\%$  [48]. Semiconductor-metal transition is predicted at  $\epsilon_{\text{arm}} = -12\%$  and  $\epsilon_{\text{zig}} = -12\%$  or 12%. Under an in-plane compressive strain, the bandgap of bilayer  $\text{MoSi}_2\text{N}_4$  and  $\text{WSi}_2\text{N}_4$  is transferred from the indirect to direct state and the bandgap value changes slightly, while the bandgap rapidly decreases with the increasing tensile strain [102].

The vertical (out-of-plane) compressive strain is also demonstrated to effectively tune the electronic properties of bilayer vdW  $\text{MA}_2\text{Z}_4$  [97]. With the increase of vertical compressive strain, the bandgap of bilayer  $\text{MoSi}_2\text{N}_4$  monotonically decreases and reaches 0 eV at  $\epsilon = 22\%$  (Fig. 8(b)). This is attributed to the opposite energy shift of the states in different layers. This shift is driven by the asymmetric charge redistribution on the inner Z-Z sublayer at the interface. The similar transition is confirmed in other bilayer  $\text{MA}_2\text{Z}_4$ , and the pressure to realize such a transition ranges from 2.18 to 32.04 GPa.

The potential of 2D materials in industrial-grade low-dimensional nanodevices is further boosted by the enormous design flexibility offered by the vertical vdW heterostructures (vdWHs), in which physical properties can be customized by the vertically stacking of different 2D atomic layers. Interlayer coupling of semiconducting vdWHs form 3 types of band alignment: type I (strad-

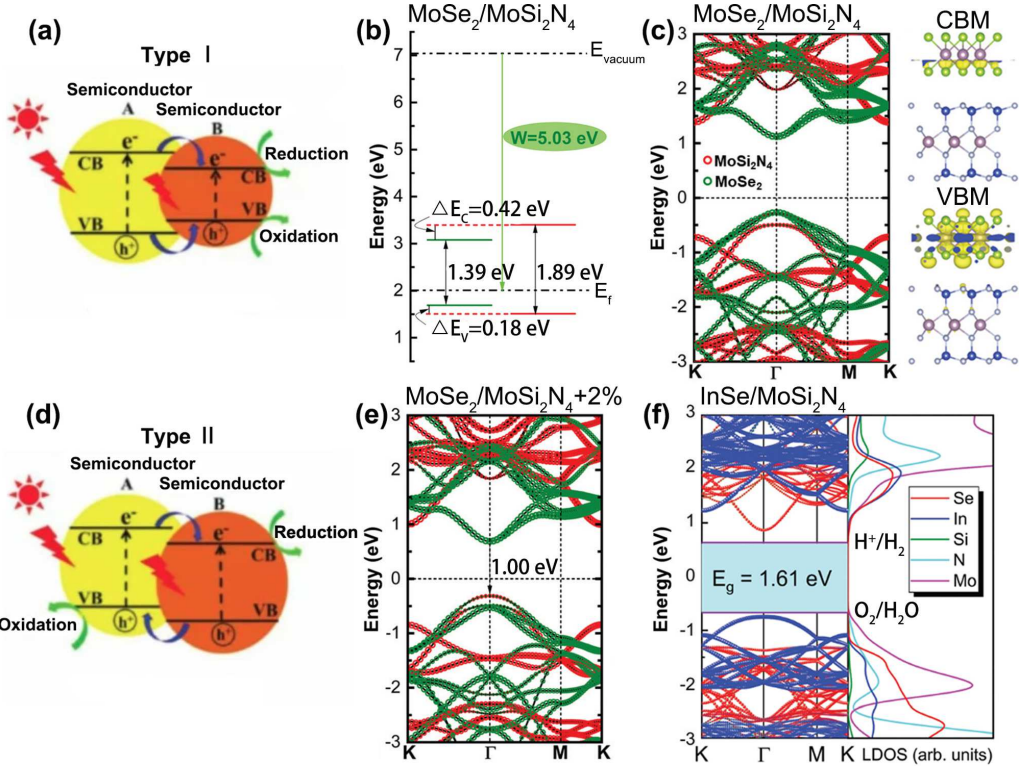


FIG. 9. Semiconducting heterostructures: (a) schematic diagrams of type I (straddling gap) and (d) type II (staggered gap) bands. (b) Type I band alignment of  $\text{MoSe}_2/\text{MoSi}_2\text{N}_4$  and (c) charge distribution at CBM and VBM. Type II band structures of (e)  $\text{MoSe}_2/\text{MoSi}_2\text{N}_4$  under 2% strain and (f)  $\text{InSe}/\text{MoSi}_2\text{N}_4$ . [103, 104]

dling gap binds electrons/holes with the critical ratio of conduction band offset and valence band offset), type II (staggered gap promotes the separation of electrons and holes and suppresses the recombination of electrons and holes), and type III (broken gap). Several previous studies have revealed the electronic properties of vdWHs by stacking 2D semiconductors with  $\text{MA}_2\text{Z}_4$ .

TMDs/ $\text{MA}_2\text{Z}_4$  vdWHs at the ground state belong to the type I alignment, due to the mismatch induced by strain and layer interaction between TMDs and  $\text{MoSi}_2\text{N}_4$  (Fig. 9) [103, 105]. TMDs provide the main contribution to CBM and VBM. The carrier mobilities of  $\text{MoSe}_2/\text{MoSi}_2\text{N}_4$  and  $\text{WSe}_2/\text{MoSi}_2\text{N}_4$  are up to  $10^4 \text{ cm}^2\text{V}^{-1}\text{s}^{-1}$ , which are higher than those of monolayer  $\text{MoSe}_2$  and  $\text{WSe}_2$ . Under an external electric field or strain, the band structures of TMDs/ $\text{MA}_2\text{Z}_4$  vdWHs are transferred from type I to type II. Actually, some other vdWHs by stacking 2D materials (e.g.,  $\text{C}_3\text{N}_4$ ,  $\text{ZnO}$ ,  $\text{InSe}$  and  $\text{Cs}_3\text{Bi}_2\text{I}_9$ ) with  $\text{MoSi}_2\text{N}_4$  exhibit semiconducting characteristic with type II band structure, indicating promising application in photocatalytic field [104, 106–108]. The carrier mobility of type II  $\text{InSe}/\text{MoSi}_2\text{N}_4$  is up to  $10^4 \text{ cm}^2\text{V}^{-1}\text{s}^{-1}$ , indicating more suitable for photocatalytic nano devices when compared with type I TMDs/ $\text{MA}_2\text{Z}_4$  vdWHs. In addition,  $\text{BP}/\text{MoSi}_2\text{P}_4$  and  $\text{BP}/\text{MoGe}_2\text{N}_4$  vdWHs possess direct bandgap and belong to type II alignment [109, 110]. Combined with high op-

tical absorption properties, these  $\text{MA}_2\text{Z}_4$ -based vdWHs would be promising candidates for solar cell devices.

In metal and semiconductor contacts, the Schottky phenomenon with rectification effect in vdWHs occurs. Reducing the Schottky barrier height (SBH) or tuning the Schottky contacts to Ohmic contacts are key challenges for achieving energy efficient and high-performance power devices.  $\text{MA}_2\text{Z}_4$ -based vdWHs provide opportunities for reconfigurable and tunable nanoelectronic devices. In graphene/ $\text{MA}_2\text{Z}_4$  vdWHs, there exists a tiny bandgap [111]. P-type Schottky contacts are formed at the interfaces of two heterojunctions, where the electrons are transferred from graphene to  $\text{MoSi}_2\text{N}_4$  ( $\text{WSi}_2\text{N}_4$ ). The n-type SBH ( $\Phi_n$ ) and the p-type SBH ( $\Phi_p$ ) are 0.922 eV and 0.797 eV, respectively, indicating the presence of a p-type Schottky contact [112]. In contrast, graphene/ $\text{MoGe}_2\text{N}_4$  vdWH forms an n-type Schottky contact with a barrier of 0.63 eV [113]. Monolayer Janus  $\text{MoSiGeN}_4$  maintains the semiconducting property with an indirect bandgap of 1.436 (2.124) eV obtained by PBE (HSE06) [114]. The vdWHs formed by graphene and Janus  $\text{MoGeSiN}_4$  or  $\text{MoSiGeN}_4$  have been investigated. The n-type SBH of graphene/ $\text{MoGeSiN}_4$  is 0.63 eV, while the p-type SBH of graphene/ $\text{MoSiGeN}_4$  is 0.74 eV. These SBHs are close to those of  $\text{MA}_2\text{Z}_4$  ( $\text{MoSi}_2\text{N}_4$  and  $\text{MoGe}_2\text{N}_4$ ), but more adjustable, providing a useful guidance for the design of controllable Schot-

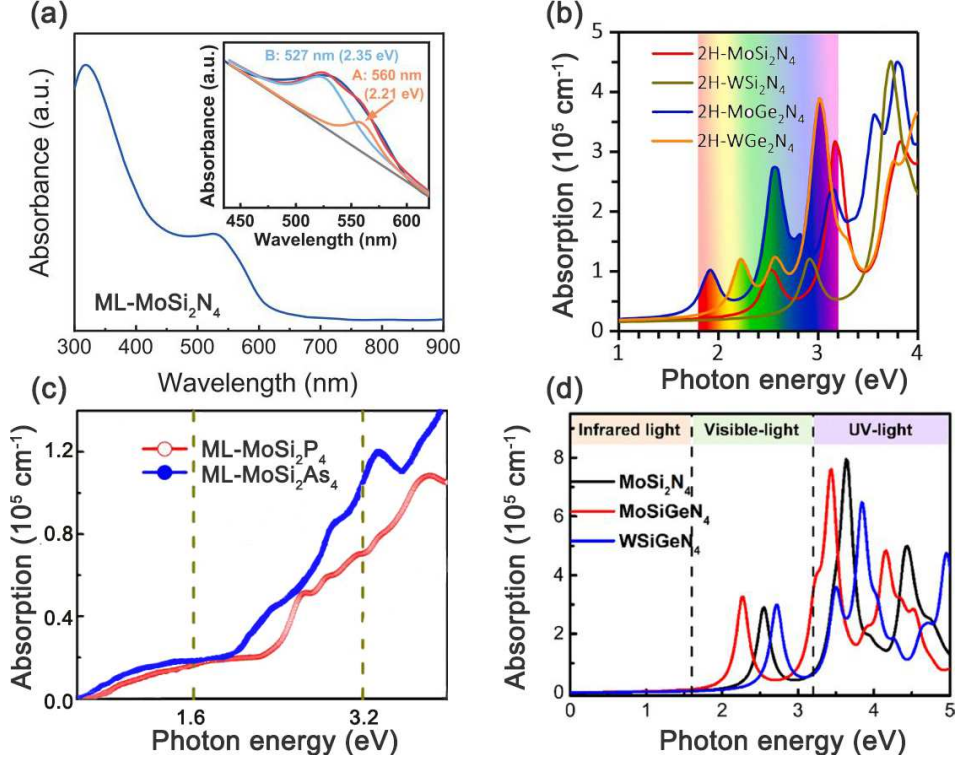


FIG. 10. Optical absorption spectra of monolayer  $MA_2Z_4$  system: (a)  $MoSi_2N_4$ , (b)  $MA_2N_4$  ( $M = Mo/W$ ,  $A = Si/Ge$ ), (c)  $MoSi_2Z_4$  ( $Z = P/As$ ), and (d) Janus  $MSiGeN_4$ . [28, 47, 72, 101]

tky nanodevices by using  $MA_2Z_4$  family. Compared with graphene-based vdWHs, the vdWHs formed by  $MA_2Z_4$  and other 2D materials possess better performance in Schottky contact [112, 115]. In  $NbS_2/MoSi_2N_4$ ,  $\Phi_n$  and  $\Phi_p$  are 1.642 eV and 0.042 eV, respectively [112]. This ultralow p-type SBH of  $NbS_2/MoSi_2N_4$  vdWH suggests the potential of  $NbS_2$  as an efficient 2D electrical contact to  $MoSi_2N_4$  with high charge injection efficiency, particularly at room-temperature.

In addition, the Schottky contact types of multilayer vdWHs vary with the order of stacking layers. For instance, the graphene/ $MoSi_2N_4/MoGe_2N_4$  vdWH has an n-type Schottky contact with a SBH of 0.33 eV. While  $MoSi_2N_4$ /graphene/ $MoGe_2N_4$  and  $MoSi_2N_4/MoGe_2N_4$ /graphene vdWHs are both p-type with a SBH of 0.41 and 0.46 eV, respectively [116]. The contact barriers in the multilayer vdWHs are smaller than those in the bilayer vdWHs, suggesting that the graphene/ $MoSi_2N_4/MoGe_2N_4$  vdWHs provide an effective pathway to reduce the Schottky barrier. This is highly beneficial for improving the charge injection efficiency of contact heterostructures. The p-type Schottky contacts of  $MoSi_2N_4$ /graphene or  $WSi_2N_4$ /graphene at the interface can be transferred to n-type by a compressive strain. When a compressive strain of 10% is applied, the transition from Schottky to Ohmic contacts occurs in  $MoSi_2N_4$ /graphene and  $WSi_2N_4$ /graphene. However, no transition is induced by a tensile strain [111, 113].

## F. Optical properties

The optical absorption of monolayer  $MA_2Z_4$  system is up to  $10^5 \text{ cm}^{-1}$  in the visible range [28, 57, 120, 121], which is comparable with that of graphene, phosphorene and  $MoS_2$ . In monolayer  $MoSi_2N_4$  (Fig. 10(a)), the experimental results show that a strong peak of optical absorption appears at about 320 nm and a broad peak in the range of 500–600 nm [28]. The calculated results are in good agreement with the experimental data.

Different atomic compositions bring the tunable optical properties to this system [47, 72, 101, 122]. The obvious redshift phenomena of optical absorption spectra are triggered by heavy atoms in M-site  $MA_2N_4$  (Fig. 10(b)), while the absorption coefficient is insensitive to the M-site counterparts. The absorption of  $MoSi_2N_4$  and  $WSi_2N_4$  is both  $10^5 \text{ cm}^{-1}$  in the visible region. The similar red-shift of absorption spectra exhibits in A- or Z-site  $MoA_2Z_4$  as well (Fig. 10(c)). The absorption coefficient, however, is improved with the increasing mass of A or Z atoms. For instance, the absorptions of  $MoSi_2Z_4$  ( $Z = N/P/As$ ) are in the order of  $MoSi_2N_4/MoSi_2P_4/MoSi_2As_4$ . In Janus  $MA_2Z_4$  (Fig. 10(d)), the redshift of absorption spectra and the absorption enhancement exist in the lighter  $MoSiGeN_4$ , compared with  $WSiGeN_4$ . As for  $MA_2Z_4$ -derived materials (e.g.,  $CrC_2N_4$  [60],  $SnGe_2N_4$  [62] and  $XMoSiN_2$  [63]), the absorption of visible light can be up to  $10^5 \text{ cm}^{-1}$  as

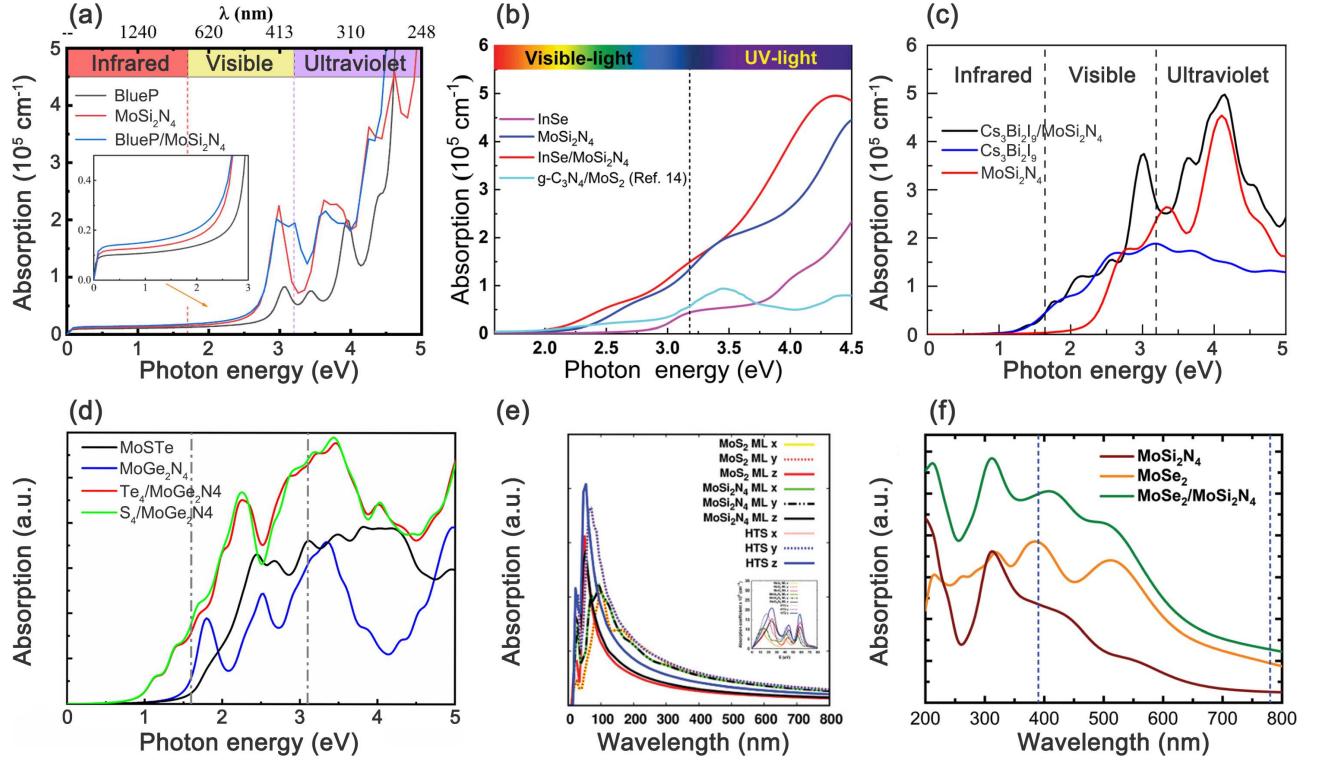


FIG. 11. Optical absorption spectra of  $MA_2Z_4$  based heterostructures: (a) BlueP/MoSi<sub>2</sub>N<sub>4</sub> (b) InSe/MoSi<sub>2</sub>N<sub>4</sub>, (c) Cs<sub>3</sub>Bi<sub>2</sub>I<sub>9</sub>/MoSi<sub>2</sub>N<sub>4</sub>, (d) Janus MoSTe/MoGe<sub>2</sub>N<sub>4</sub>, (e) MoS<sub>2</sub>/MoSi<sub>2</sub>N<sub>4</sub>, and (f) MoSe<sub>2</sub>/MoSi<sub>2</sub>N<sub>4</sub>. [103, 104, 108, 117–119]

well. When Cr is replaced by Mo or W in CrC<sub>2</sub>N<sub>4</sub>, the first absorption peak appears in ultraviolet spectra and high frequencies.

Furthermore, optical properties of  $MA_2Z_4$  are shown to be manipulated by strain, surface functionalization, and heterostructure. Firstly, the optical absorption spectrum of MoSi<sub>2</sub>N<sub>4</sub> shows redshift (blueshift) under a tensile (compressive) strain [96, 123, 124]. The absorption edges decrease with the increasing tensile strain. A 4–10% tensile strain enhances the optical absorption capacity in the visible region up to 43–70%. The reflectance ability (average reflectance rate), meanwhile, is improved from 16% to 23% with the tensile strain from 0% to 10%. Yang et al. [124] found monolayer MoSi<sub>2</sub>N<sub>4</sub> exhibits more outstanding optical absorption capacity in the ultraviolet range than that in the visible range, especially under biaxial compressive strain. The optical bandgap is evaluated by the slope of absorption peak, in which the corresponding value is 2.47 eV without strain, 2.9 eV with -3% strain and 3.05 eV with -4% strain. Furthermore, compared with monolayer  $MA_2Z_4$ , the bilayer or multilayer  $MA_2Z_4$  shows strong optical absorbance and broad absorption areas as well [101, 125, 126]. When the vertical (out-of-plane) compressive strain increases from 0 to 12%, there exists strong blueshift but only slight decrease of absorption and reflectivity. This manifests that  $MA_2Z_4$  possesses stable optical absorption capacity independent of vertical strain and the number of layers, which will be more convenient for experimental fabrication of

2D optoelectronic devices [126].

Secondly, it has been reported that surface functionalization plays an active role in regulating the optical properties of MoSi<sub>2</sub>N<sub>4</sub>, where the adatoms can be Au, F, and Alkali elements (Li, Na, K) [127–129]. In Au-MoSi<sub>2</sub>N<sub>4</sub>, the optical absorption capacity is significantly improved with the increment of Au concentration (6.25–56.3%/unit cell). It can be increased by 1–2 times in the visible light region and by 52% in the ultraviolet region. The results show that Au absorption is beneficial for the photocatalytic activity, making Au-MoSi<sub>2</sub>N<sub>4</sub> a potential candidate for photoelectrochemical applications and short-wavelength optoelectronic devices. Alkali-metal adsorption not only enhances the optical absorption coefficient but enlarges the absorption area [128]. The absorption coefficient at a wavelength of 380 nm is  $0.34 \times 10^5$  cm<sup>-1</sup> for pristine MoSi<sub>2</sub>N<sub>4</sub>,  $0.57 \times 10^5$  cm<sup>-1</sup> for Li-MoSi<sub>2</sub>N<sub>4</sub>,  $1.09 \times 10^5$  cm<sup>-1</sup> for Na-MoSi<sub>2</sub>N<sub>4</sub>, and  $0.89 \times 10^5$  cm<sup>-1</sup> for K-MoSi<sub>2</sub>N<sub>4</sub>. The light at wavelength of 780 nm is almost unabsorbable by pristine MoSi<sub>2</sub>N<sub>4</sub>. However, the absorption at this wavelength is  $0.92 \times 10^5$  cm<sup>-1</sup> for Li-MoSi<sub>2</sub>N<sub>4</sub>,  $1.34 \times 10^5$  cm<sup>-1</sup> for Na-MoSi<sub>2</sub>N<sub>4</sub>, and  $1.14 \times 10^5$  cm<sup>-1</sup> for K-MoSi<sub>2</sub>N<sub>4</sub>. Na-MoSi<sub>2</sub>N<sub>4</sub> exhibits the strongest optical response among these three alkali-metal-decorated MoSi<sub>2</sub>N<sub>4</sub>.

Thirdly, in Fig 11, the optical absorption capacity of monolayer MoSi<sub>2</sub>N<sub>4</sub> is comparable with that of monolayer MoS<sub>2</sub> and MoSe<sub>2</sub>, and better than that of other monolayer 2D materials, such as BlueP, InSe and

$\text{Cs}_3\text{Bi}_2\text{I}_9$ . It is interesting that  $\text{MA}_2\text{Z}_4$ -based vdWHs have more excellent optical response than the monolayer  $\text{MA}_2\text{Z}_4$  and other monolayer 2D materials [103, 104, 108, 110, 117–119, 130]. These enhancements mainly appear in the visible and ultraviolet light range. The high performance of BlueP/ $\text{MoSi}_2\text{N}_4$  vdWH is in the visible light range of 460–780 nm (the insert of Fig. 11(a)), which is attributed to the overlap of electronic states between valence bands caused by the interlayer coupling and charge transfer [117]. InSe/ $\text{MoSi}_2\text{N}_4$  vdWH shows great improvement of absorption in the ultraviolet range [104]. The absorption of monolayer  $\text{Cs}_3\text{Bi}_2\text{I}_9$  is superior than that of monolayer  $\text{MoSi}_2\text{N}_4$  in the photon energy range of 1–2.6 eV, while the relationship reverses in the ultraviolet range (high photon energy), as shown in Fig. 11(c). Surprisingly, the absorption is enhanced in the whole range by constructing the  $\text{Cs}_3\text{Bi}_2\text{I}_9/\text{MoSi}_2\text{N}_4$  vdWH [108]. Similarly, this increasing phenomena appear in Janus MoSTe/ $\text{MoGe}_2\text{N}_4$ ,  $\text{MoS}_2/\text{MoSi}_2\text{N}_4$  and  $\text{MoSe}_2/\text{MoSi}_2\text{N}_4$  vdWHs (Fig. 11(d–f)) [103, 118, 119], indicating the tunability of optical absorption by forming vdWHs. As for strain effect on the absorption of  $\text{MA}_2\text{Z}_4$ -based heterostructures, the obvious redshift (blueshift) of optical spectrum appears under a tensile (compressive) strain. In BlueP/ $\text{MoSi}_2\text{N}_4$  vdWH, it is found that a compressive strain restrains the absorption on coefficient in the visible region, while a tensile strain (0–8%) promotes the optical absorption ability [117]. In Janus MoSTe/ $\text{MoGe}_2\text{N}_4$  vdWH, a compressive strain increases the absorption coefficient in the visible and ultraviolet regions, while a tensile strain enhances it in the infrared region, regardless of which side (S or Te atoms) approaching to  $\text{MoSi}_2\text{N}_4$  [119].

### G. Magnetic properties

It has been reported that group-VB (V/Nb/Ta)  $\text{MA}_2\text{Z}_4$  nanosheets exhibit robust intrinsic magnetism, and group-VIB (Cr/Mo/W)  $\text{MA}_2\text{Z}_4$  ones show antiferromagnetic ground states [29, 131–133]. In Table II,  $\text{NbSi}_2\text{N}_4$ ,  $\text{NbSi}_2\text{As}_4$ ,  $\text{NbGe}_2\text{Z}_4$ ,  $\text{NbGe}_2\text{P}_4$ ,  $\text{TaSi}_2\text{N}_4$  and  $\text{TaGe}_2\text{P}_4$  are ferromagnetic metals with the magnetic moment from 0.37 to 0.78  $\mu_B$  per metal atom, while  $\text{VA}_2\text{Z}_4$  (except  $\text{VGe}_2\text{N}_4$ ) are ferromagnetic semiconductors with a magnetic moment of 1  $\mu_B$  per V atom. On the other hand,  $\text{NbSi}_2\text{P}_4$ ,  $\text{TaSi}_2\text{P}_4$ ,  $\text{TaSi}_2\text{As}_4$ ,  $\text{TaGe}_2\text{N}_4$  and group-VIB  $\text{MA}_2\text{Z}_4$  (e.g.,  $\text{CrSi}_2\text{N}_4$ ,  $\text{CrSi}_2\text{P}_4$ ,  $\text{CrGe}_2\text{N}_4$ ,  $\text{CrGe}_2\text{As}_4$ ,  $\text{MoGe}_2\text{As}_4$ ,  $\text{WGe}_2\text{As}_4$  and  $\text{WGe}_2\text{P}_4$ ) are antiferromagnetic.

For ferromagnetic semiconductors, there exist three types: type-I spin gapless semiconductors (SGSs) (a zero bandgap in one spin channel but a bandgap in another spin channel), type-II SGSs (bandgaps of spin-up or spin-down channel but zero gap for the valence band and conduction band in opposite spin channels), and bipolar magnetic semiconductors (BMSs) (the valence band and conduction band in opposite spin channels approach-

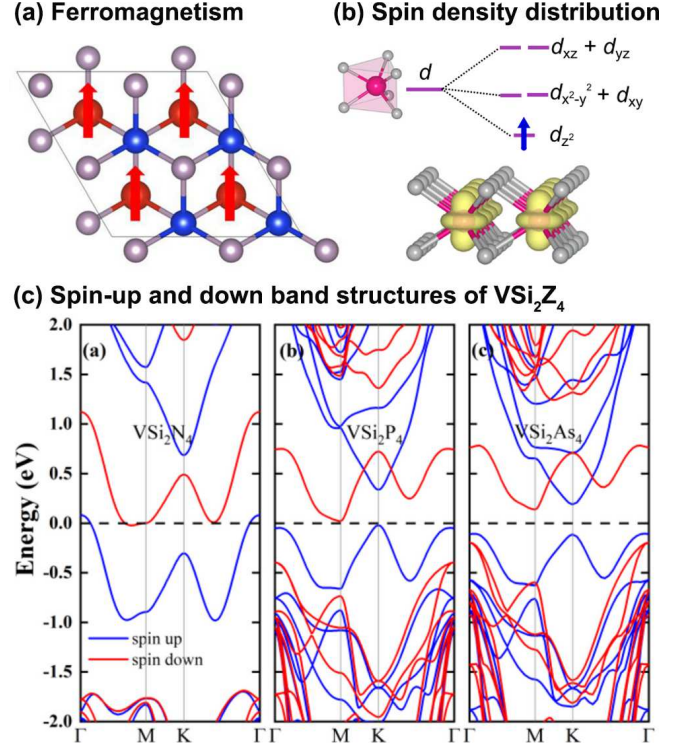


FIG. 12. (a) Magnetic ground states of monolayer  $\text{VSi}_2\text{Z}_4$ . (b) Spin density distribution. (c) Spin-up (blue) and spin-down (red) band structures of  $\text{VSi}_2\text{Z}_4$  by PBE functional. [134, 135]

ing to Fermi level). 2D SGSs and BMSs with high Curie temperatures are highly desirable for advanced spintronic applications due to their unique electronic structure and high spin polarization [136, 137]. The intrinsic magnetic mechanisms of monolayer  $\text{MA}_2\text{Z}_4$  nanosheets (e.g.,  $\text{VSi}_2\text{N}_4$ ,  $\text{VSi}_2\text{P}_4$  and  $\text{NbSi}_2\text{N}_4$ ) have been investigated by dissecting the spin-up and spin-down band structures, magnetic anisotropic energy (MAE) and Curie temperature ( $T_C$ ).

The magnetic ground states of monolayer  $\text{VSi}_2\text{Z}_4$  are ferromagnetic (FM) by considering the spin polarization, as shown in Fig. 12(a) [134]. Based on GGA-PBE functional calculations, for the spin-up channel of monolayer  $\text{VSi}_2\text{P}_4$  both VBM and CBM are located at K point and a direct bandgap of 0.36 eV presents, while VBM at  $\Gamma$  point and CBM at M point indicate an indirect bandgap of 0.42 eV for the spin-down channel (Fig. 12(c)). The zero indirect bandgap between spin-up VBM and spin-down CBM implies that monolayer  $\text{VSi}_2\text{P}_4$  and  $\text{VSi}_2\text{N}_4$  are type-II SGSs via PBE calculations. In  $\text{VSi}_2\text{As}_4$ , the VBM and CBM for spin channels nearby the Fermi level are in the opposite direction, indicating that the spin-polarized currents would be easily generated with tunable spin polarization by applying a small gate voltage. The results show that the intrinsic ferromagnetism is attributed to the unpaired electron from the metal atom. It can be noticed that in  $\text{VSi}_2\text{Z}_4$  (Fig. 12(b)), the  $d$  orbital electrons from transition metal occupy the bands

TABLE II. Structural properties of magnetic  $MA_2Z_4$ : lattice constants ( $a$ ), magnetic moment ( $Mag^{PBE}$  for PBE and  $Mag^{HSE}$  for HSE), magnetic type (FM for ferromagnetic and AFM for antiferromagnetic), magnetic anisotropic energy (MAE), Curie temperature ( $T_C$ ) with PBE, PBE+ $U$  and HSE. [28, 29, 98]

Struc.	Phase	$a$ ( $\text{\AA}$ )	$Mag^{PBE}$ ( $\mu_B$ )	$Mag^{HSE}$ ( $\mu_B$ )	$Mag^{HSE}$ ( $\mu_B$ )	Type	MAE (meV)	$T_C^{PBE}$ (K)	$T_C^{PBE+U}$ (K)	$T_C^{HSE}$ (K)
$VSi_2N_4$	$\alpha_1$	2.88	0.97	1.05	1.00–1.19	FM	75.0–76.4	230	350	506–687
$VSi_2P_4$	$\alpha_1$	2.88	0.96	1.04	1.00	FM	68.5	230	350	506–687
	$\delta_4$	3.48	1.00	*	1.00	FM	*	235	452	*
$VSi_2As_4$	$\alpha_2$	3.72	1.00	*	1.00	FM	*	250	*	*
$VGe_2P_4$	$\alpha_2$	3.56	1.00	*	1.00	FM	*	*	*	*
$VGe_2As_4$	$\alpha_2$	3.72	1.00	*	1.00	FM	*	*	*	*
$NbSi_2N_4$	$\alpha_1$	2.96	0.32–0.57	*	1.00	FM	95.5	*	*	*
$NbSi_2P_4$	$\alpha_1$	3.53	*	*	*	AFM	*	*	*	*
$NbGe_2N_4$	$\alpha_1$	3.09	0.72	*	1.00	FM	*	*	*	197
$TaSi_2P_4$	$\alpha_1$	3.54	*	*	*	AFM	*	*	*	*
$TaSi_2As_4$	$\alpha_2$	3.68	*	*	*	AFM	*	*	*	*
$TaGe_2N_4$	$\alpha_1$	3.08	0.49	*	1.00	FM	*	*	*	*
$YSi_2N_4$	$\alpha_1$	3.07	1.00	*	1.00	FM	*	*	*	90
$YSi_2N_4$	$\beta_2$	3.08	1.00	*	1.00	FM	*	*	*	85

approaching to the Fermi level, accompanying with the mixed orbital (e.g.,  $d_{z^2} + d_{x^2+y^2}$ ) or transition of orbital composition (e.g., the transition between  $d_{z^2}$  and  $d_{x^2+y^2}$ ) [120, 135, 138].

The increment of bandgap is 0.3 eV under the consideration of Coulomb interaction ( $U$ ) effect [29, 139]. The bandgap of  $VSi_2Z_4$  by HSE functional is larger than that by PBE and PBE+ $U$ . For instances, by HSE functional,  $VSi_2N_4$  possesses a direct bandgap of 0.78 eV at K point,  $VSi_2P_4$  has an indirect bandgap of 0.84 eV with spin-up CBM at  $\Gamma$  point and spin-down VBM at M point, and  $NbSi_2P_4$  exhibits an indirect bandgap of 0.54 eV with spin-up VBM at  $\Gamma$  point and spin-down CBM at M point. The comparison with the three calculation method shows that the bandgap increases from PBE, PBE+ $U$  to HSE. However, the spin polarizations under these methods are still high since there exists only one spin channels around the Fermi level.

Magnetic anisotropic energy (MAE) of  $NbSi_2N_4$ ,  $VSi_2N_4$  and  $VSi_2P_4$  are summarized in Table 2. The positive values indicate the in-plane alignment of magnetic moments. Therefore, these ferromagnetic monolayer  $MA_2Z_4$  nanosheets have easy magnetization plane, i.e., none energy consumes when magnetization rotates in the plane. In the finite energy resolution (1 eV), it is found that the total energy has no dependence on the angle of the magnetic moment within the plane, implying the weak in-plane anisotropy of MAE [139], similar to the recently reported 2D  $MnPS_3$  [140]. MAE of  $VSi_2Z_4$  ( $Z = N/P$ ) in the range of 0.11 to 0.25 meV

per magnetic atom is lower than other 2D materials (e.g., 0.8 meV of  $CrI_3$  [141], 0.72 meV of  $Fe_3P$  [142] and 1 meV of  $Fe_3GeTe_2$  [143]), and close to  $CrCl_3$  (0.02 meV),  $CrBr_3$  (0.16 meV),  $NiI_2$  [144] (0.11 meV) and  $FeCl_2$  [145] (0.07 meV).

Curie temperature ( $T_C$ ) of  $VSi_2N_4$ ,  $VSi_2P_4$  and  $VSi_2As_4$  is 230, 235, and 250 K, respectively. [134], which is much higher than 45 K for monolayer  $CrI_3$  [146] and 130 K for monolayer  $Fe_3GeTe_2$  [147]. In Akanda's paper [139], the normalized magnetization of  $VSi_2N_4$  and  $VSi_2P_4$  based on Monte Carlo calculations follows to the analytic expression:  $m(T) = (1 - T/T_C)^\beta$ , as shown in Fig. 14. The results from PBE+ $U$  show that  $T_C$  of  $VSi_2N_4$  and  $VSi_2P_4$  are 350 and 452 K, respectively, which are above room temperature. The difference of predicted  $T_C$  is ascribed to the unequal calculation method using different DFT functionals.  $T_C$  of  $VSi_2N_4$  by HSE functional is up to 506–687 K.  $T_C$  of Janus  $VSiGeN_4$  and  $VSiSnN_4$  is 507 K and 347 K, respectively [135]. With the same functional (e.g., PBE+ $U$ ), the transition temperature of monolayer  $MA_2Z_4$  is higher than that of other 2D magnets (e.g.,  $TcGeSe_3$ ,  $TcGeTe_3$ ,  $ScCl$ ,  $YCl$ ,  $LaCl$ ,  $LaBr_2$ ,  $CrSBr$ , etc.) with high  $T_C$  over room temperature [148, 149].

The magnetic properties of  $MA_2Z_4$  family can be tuned by strain, adatoms and defects [135, 138, 139, 150–152]. Similar to the case of magnetic thin films [153–155], strain or stress also has a significant effect on magnetic behaviors of monolayer  $MA_2Z_4$ . The strain coefficient ( $\alpha_\epsilon$ ) is defined as the sensitivity of MAE to strain, which

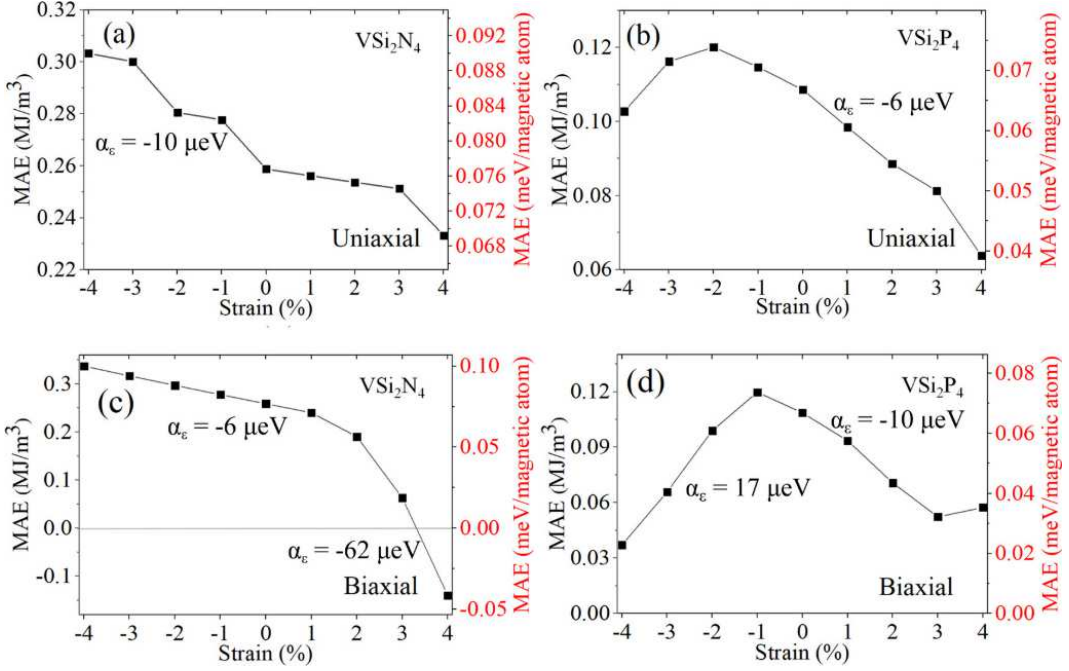


FIG. 13. Strain effect on MAE calculated with PBE(SOC) +  $U$ : (a) VSi<sub>2</sub>N<sub>4</sub> and (b) VSi<sub>2</sub>P<sub>4</sub> under a uniaxial strain, (c) VSi<sub>2</sub>N<sub>4</sub> and (d) VSi<sub>2</sub>P<sub>4</sub> under a biaxial strain. [139]

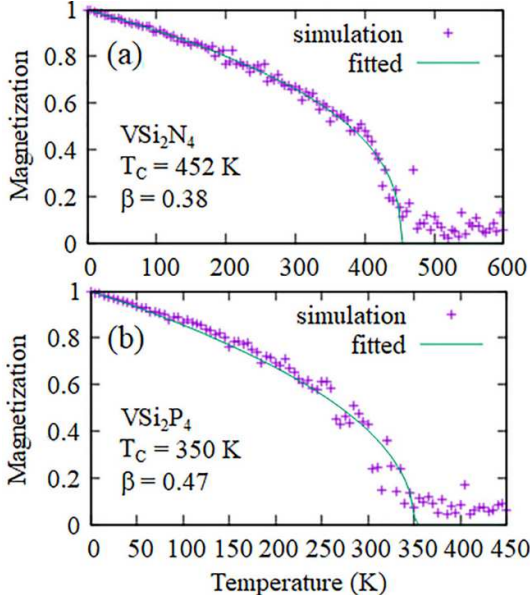


FIG. 14. Monte Carlo calculations of the normalized magnetization as a function of temperature for (a) VSi<sub>2</sub>N<sub>4</sub> and (b) VSi<sub>2</sub>P<sub>4</sub>. The solid lines show the best fits to the analytical expression. [139]

is expressed as  $\alpha_e = dE_{\text{MAE}}/d\epsilon$ . In VSi<sub>2</sub>N<sub>4</sub>,  $\alpha_e$  is  $-10 \mu\text{eV}/\%$  under a compressive uniaxial strain and  $-6 \mu\text{eV}/\%$  under a biaxial strain, while in VSi<sub>2</sub>P<sub>4</sub>,  $\alpha_e = -6 \mu\text{eV}/\%$  under a tensile uniaxial strain,  $-10 \mu\text{eV}/\%$  under a tensile biaxial strain, and  $17 \mu\text{eV}/\%$  under a

compressive biaxial strain (Fig. 13). The strain sensitivity of both two materials is lower than that of CrSb ( $32 \mu\text{eV}/\%$ ) [156]. When the biaxial strain is up to 3–4%, the spin direction of VSi<sub>2</sub>N<sub>4</sub> rotates from in-plane to out-of-plane state [138, 139].

Additionally, substitutional doping and atomic vacancies induce the transition of nonmagnetic state in MoSi<sub>2</sub>N<sub>4</sub> to magnetic state. Transition metal substitutional doping (e.g., Ag, Au, Bi, Fe, Mn, Pb and V) induces the asymmetric spin channels in MoSi<sub>2</sub>N<sub>4</sub> with generating a magnetic moment of  $1.00\text{--}5.87 \mu_B$  [152, 158]. Schwingenschlögl et al. [151] reported that N-site vacancy in MoSi<sub>2</sub>N<sub>4</sub> leads to the spin-majority bands crossing the Fermi level. N- and Si-site vacancies generate a magnetic moment of  $1.0$  and  $2.0 \mu_B$ , respectively. The nonmagnetic state in MA<sub>2</sub>Z<sub>4</sub>-derived MoN<sub>2</sub>X<sub>2</sub>Y<sub>2</sub> (XY = AlO, GaO, InO) nanosheets is transferred to ferromagnetic state by a hole doping [133]. Li et al. [159] found the element substitution of nitrogen by carbon causes different magnetic moments in monolayer MSi<sub>2</sub>C<sub>x</sub>N<sub>4-x</sub> (M = Cr/Mo/W,  $x = 1$  or 2). The position of carbon atoms determines the ground state of magnetic moments. Monolayer CrSi<sub>2</sub>CN<sub>3</sub> (C bridged Si and Mo) is predicted as ferromagnetic half-metal, where the magnetic moments is mainly originated from Cr atoms ( $0.72 \mu_B$  per atom). There exist three AFM structures, i.e., CrSi<sub>2</sub>N<sub>2</sub>C<sub>2</sub> (two C atoms located at two outermost sites), MoSi<sub>2</sub>N<sub>2</sub>C<sub>2</sub> and CrSi<sub>2</sub>N<sub>3</sub>C (one C atoms located at outermost site). The magnetic moments are ascribed to the C and metal atoms. The FM states in half-metallic 2D systems are attributed to the hole-mediated double exchange, while the AFM states

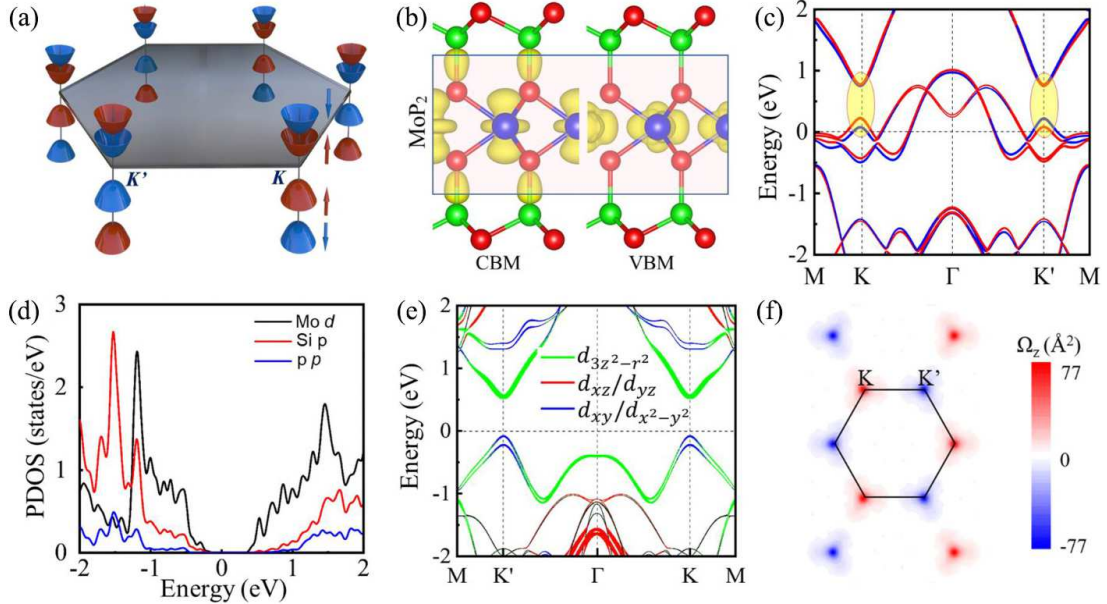


FIG. 15. (a) Schematic of the valleys near the  $K$  and  $K'$  points. (b) Charge densities at the VBM and CBM of  $\text{MoSi}_2\text{P}_4$ . (c) Band structure of  $\text{MoP}_2$ . (d) Partial densities of states (PDOSs) of  $\text{MoSi}_2\text{P}_4$ . (e) Orbital-projected band structure of  $\text{MoSi}_2\text{P}_4$ . (f) Berry curvature of  $\text{MoSi}_2\text{P}_4$  with nonzero Berry curvature indicating the abnormal transverse velocity. [157]

are originated from the super-exchange.

$\text{MA}_2\text{Z}_4$  family also has spin-valley properties. As an emerging degree of freedom, valley refers to the presence of multiple energy extremal points in the Brillouin zone (BZ) for low-energy carriers in a semiconductor. Analogous to charge and spin, the valley degree of freedom can be exploited for information encoding and processing, leading to the concept of valleytronics [160]. The spin-valley feature of semiconductors in  $\text{MA}_2\text{Z}_4$  family has been systematically studied. Taking into account the spin-orbit coupling (SOC), valley spin splittings of  $\text{MA}_2\text{Z}_4$  appear near both the CBM and VBM. The remarkable splitting near VBM is 139–500 meV, but the spin splitting near CBM is tiny [157, 161, 162].

Six kinds of monolayer  $\text{MA}_2\text{Z}_4$  ( $\text{M} = \text{Mo/W}$ ,  $\text{A} = \text{C/Si/Ge}$ ,  $\text{Z} = \text{N/P/Ge}$ ) nanosheets, i.e.,  $\text{MoSi}_2\text{P}_4$ ,  $\text{MoSi}_2\text{As}_4$ ,  $\text{WSi}_2\text{P}_4$ ,  $\text{WSi}_2\text{As}_4$ ,  $\text{WGe}_2\text{P}_4$  and  $\text{WGe}_2\text{As}_4$ , possess strong spin-valley coupling [157, 163]. They are all direct bandgap semiconductors with band extrema located at the inequivalent  $K$  and  $K'$  point (Fig. 15(a)). A remarkable spin splitting near the VBM is shown in all the six monolayers with SOC, and the splitting in W-based compounds is larger than that in Mo-based ones. The spin valleys are attributed to the  $\text{MZ}_2$  layer by analysing DOS and charge distribution (Fig. 15(b)). Furthermore, the comparison of spin band structures between monolayer  $\text{MoP}_2$  (Fig. 15(c)) and  $\text{MoSi}_2\text{P}_4$  (Fig. 15(e)) shows that there exist other interfering states in the energy range of the valleys of  $\text{MoP}_2$ . This manifests that the AZ layers play the role of structural stabilizer and protect the valley states from the interference of the  $p$  orbitals of Z atoms and  $d$  orbitals of M atom. Time-

reversal symmetry always constrains the valley-polarized current. Nonzero Berry curvature of  $\text{MA}_2\text{Z}_4$  in Fig. 15(f) indicates the abnormal transverse velocity proportional to the Berry curvature would be generated, leading to a spatial separation of the carriers coupled to two different valleys. The carriers from different valleys are accumulated at opposite sides, resulting in an anomalous valley Hall effect. [157, 164]

Monolayer  $\text{MoSi}_2\text{As}_4$  is found to exhibit ‘perfect valleys’ with no interference from other part of Brillouin zone, as well as multiple-folded valleys (Fig. 16) [164]. The another valley is originated from the second unoccupied conduction band, which enlarges the degree of freedom in energy. The calculation results show that the electron can be selectively pumped from VBM to CBM with a low photon energy of 0.41 eV. With 1.00 eV energy input, the electron can be excited to the VBM and second unoccupied conduction band, indicating the potential application of  $\text{MoSi}_2\text{As}_4$  for multiple-information operator and storage in valleytronic devices.

The experimentally synthesized  $\text{MoSi}_2\text{N}_4$  and  $\text{WSi}_2\text{N}_4$  are indirect bandgap semiconductors in which CBM is located at  $K$  (or  $K'$ ) and VBM at  $\Gamma$  point, limiting their potential utilization in valleytronic devices. Nevertheless, the difference between the uppermost valence band at  $K$  and  $\Gamma$  point is small (e.g., 144.4 meV in  $\text{MoSi}_2\text{N}_4$ ). Strain engineering could eliminate this small difference. The indirect bandgap of  $\text{MoSi}_2\text{N}_4$  is transferred to the direct bandgap under a compressive strain of 2% and the direct-gap state maintains until a compressive strain up to 4% [160, 161]. Monolayer  $\text{MoSi}_2\text{N}_4$  with -4% strain possesses a large spin splitting and strong spin valley cou-

pling (valleys K and K') and thus would be an ideal valleytronic materials.

For other magnetic members in  $MA_2Z_4$  family, the coupling between magnetism and valley provokes the quantum anomalous Hall (QAH) effect. The spin splitting of  $VSi_2N_4$  is 102.3 meV (27.3 meV) at VBM (CBM) [37]. In contrast, the spin splitting of  $VSi_2P_4$  is 49.4 meV at CBM but can be neglected at VBM [165]. Ma et al. [165] separately considered the effect of SOC or magnetic exchange interaction on spin splitting of  $VSi_2P_4$ , and proposed that the combined effect causes its spontaneous valley polarization (Fig. 17). The spin splitting energy at K and K' points is expressed as  $\Delta^{K/K'} = E_{\uparrow}^{K/K'} - E_{\downarrow}^{K/K'}$ ,  $\uparrow$  and  $\downarrow$  mean spin-up and spin-down channels. With the magnetic exchange interaction, the broken time-reversal symmetry leads to  $\Delta_{mag}^K = \Delta_{mag}^{K'}$ ; with SOC, the time-reversal symmetry results in  $\Delta_{SOC}^K = -\Delta_{SOC}^{K'}$ ; with the synergistic effect, the net spin splitting should be the  $\Delta_{mag}^K + \Delta_{SOC}^K$  at K point and  $\Delta_{mag}^{K'} + \Delta_{SOC}^{K'}$  at K' point. Li et al. [166] found Hubbard- $U$  can effectively tune the phase diagram of  $MA_2Z_4$  family, and result in intriguing magnetic, valley and topological features. When  $U = 2.25$  and  $2.36$  eV, the QAH phase and valley structure coexist, as shown in Fig. 17(e) and (f). Besides, strain effect promotes the trivial topology in  $VSi_2P_4$  and

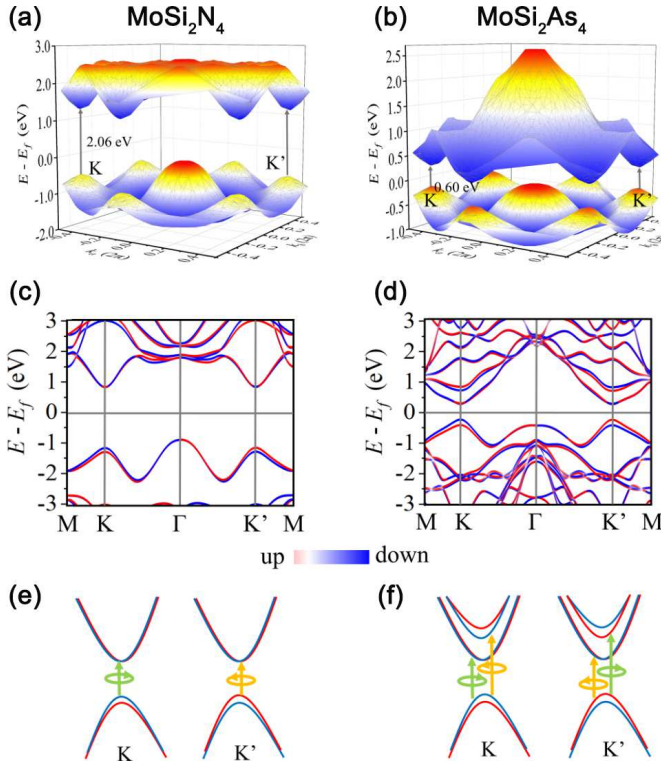


FIG. 16. Spin-valley band structures of monolayer  $MoSi_2N_4$  and  $MoSi_2As_4$ : (a) (b) 3D CBM and VBM of  $MoSi_2N_4$  and  $MoSi_2As_4$ , (c) (d) spin down and spin up band with SOC. Comparison between (e) traditional valleys and (f) multiple-folded valleys. [164]

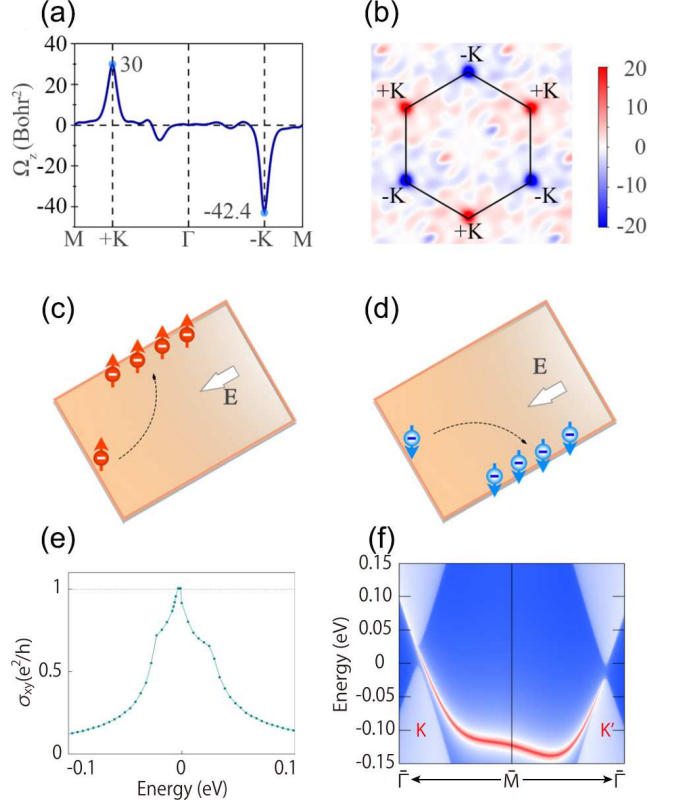


FIG. 17. Berry curvature of monolayer  $VSi_2P_4$  (a) as a curve along the high-symmetry points and (b) as a counter map over the 2D Brillouin zone. (c) (d) Diagrams of the anomalous valley Hall effect under an electron doping and an in-plane electric field, but with opposite magnetization. (e) Anomalous Hall conductivity versus chemical potential with SOC. (f) The corresponding edge spectrum for the QAH state with SOC. Note that the plot is centred at the M point, so the left valley is K and the right valley is K'. [165, 166]

$VA_2Z_4$ -derived materials ( $VN_2X_2Y_2$ ) [165–167]. There exists an edge state connecting the valence and conduction bands under a compressive strain of 2.1 % [165], and a biaxial tensile strain [166].

### III. PROSPECTIVE APPLICATION

#### A. Transistors

Semiconductors in 2D  $MA_2Z_4$  family have atomic-scale thickness, ambient stability, suitable bandgap and excellent electronic mobilities, indicating that this family could be promising candidates for the new-generation miniaturized field-effect transistors (FETs) [168–172]. Double-gate metal-oxide-semiconductor FET (DG MOSFET) based on monolayer  $MoSi_2N_4$  has been designed and investigated [168, 169]. This kind of FET has advantages of high operating frequency, good gain controllability and low feedback capacitance. There are three

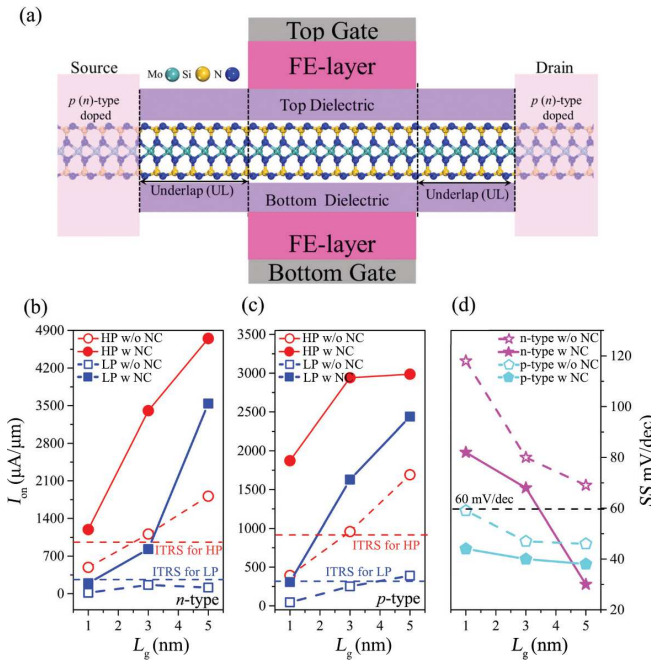


FIG. 18. (a) Nanodevice design of monolayer  $MA_2Z_4$ -based transistor. On-current ( $I_{on}$ ) of (b) n-type and (c) p-type versus gate length ( $L_g$ ). (d) Subthreshold swing ( $SS$ ) versus  $L_g$ . [168]

factors to evaluate the performance of DG MOSFET, i.e., on-current ( $I_{on}$ ), gate control, and intrinsic delay time and power consumption.

$I_{\text{on}}$  represents the device operating speed, while off-current ( $I_{\text{off}}$ ) means the static power dissipation. According to the International Technology Roadmap for Semiconductors (ITRS) published in 2013, the standard of  $I_{\text{on}}$  ( $I_{\text{on}}/I_{\text{off}}$ ) is  $900 \mu\text{A}\mu\text{m}^{-1}$  ( $9.0 \times 10^3$ ). The highest  $I_{\text{on}}$  of n-type (p-type) DG monolayer  $\text{MoSi}_2\text{N}_4$  MOSFET is up to  $1813 \mu\text{A}\mu\text{m}^{-1}$  ( $1690 \mu\text{A}\mu\text{m}^{-1}$ ), as shown in Fig. 18(b) and (c) [168], which is 70% (80%) higher than n-type (p-type) DG monolayer  $\text{MoS}_2$  MOSFET [173]. Subthreshold swing ( $SS$ ) can reflect the switching rate of MOSFET between the on and off states, which always describes the gate-control ability in the subthreshold region.  $SS$  of DG monolayer  $\text{MA}_2\text{Z}_4$  MOSFET is predicted as  $69 \text{ mV dec}^{-1}$  for the n-type and  $52 \text{ mV dec}^{-1}$  for the p-type when the optimum  $I_{\text{on}}$  is reached. As for sub-5 nm scale MOSFETs, the value of  $SS$  should be below the Boltzmann limit at room temperature ( $60 \text{ mV dec}^{-1}$ ) since the short channel effect would cause the coexist of tunneling current and thermionic current, and further influence the overall performance of devices. When gate length ( $L_g$ ) is below 5 nm,  $SS$  of p-type and n-type  $\text{MA}_2\text{Z}_4$  MOSFETs is  $46\text{--}52 \text{ mV dec}^{-1}$  (Fig. 18(d)) [168, 169]. Switching speed in MOSFETs is described by the intrinsic delay time and power consumption. The ITRS standard of delay time for the high performance and low power is 0.423 and 1.493 ps, respectively. Besides, ITRS requirements of power consumption for the high performance and low

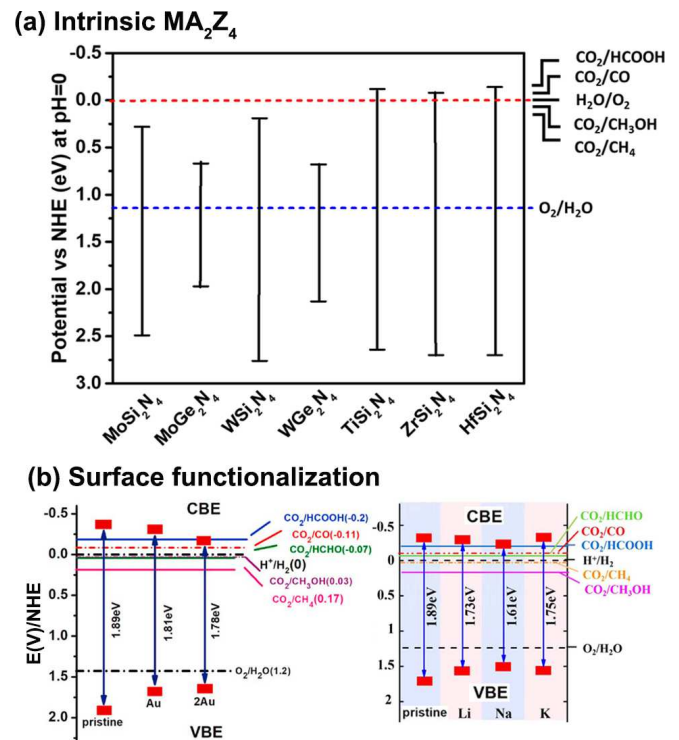


FIG. 19. Band edge positions with respect to water redox and CO<sub>2</sub> reduction levels of (a) monolayer MA<sub>2</sub>Z<sub>4</sub> members and (b) MoSi<sub>2</sub>N<sub>4</sub> after surface functionalization. The normal hydrogen electrode (NHE) potential is set as 0 eV. [120, 127, 128]

power are 0.24 and 0.28  $fJ\mu m^{-1}$ , respectively. DG monolayer  $MA_2Z_4$  MOSFET with an optimum assembly can meet the standards. In brief, the design of device determines whether DG monolayer  $MA_2Z_4$  MOSFET satisfies the ITRS standard in terms of the structural parameters, like gate length, doping concentration to the source and drain, and underlap length between gate and electrodes.

## B. Photocatalyst

Photocatalytic process can be described by four important steps: (1) light absorption to generate electron-hole pairs, (2) separation of excited charges to suppress the electron-hole recombination, (3) transfer of electrons and holes to the surface of photocatalysts, and (4) utilization of charges on the surface for redox reactions [174, 175]. The typical reactions are water splitting and CO<sub>2</sub> reduction, which are important for the environment and dual-carbon confinement strategy. 2D MA<sub>2</sub>Z<sub>4</sub> systems with high optical absorption could be prospective candidates for photocatalytic applications.

The band edges of photocatalyst candidate in 2D MA<sub>2</sub>Z<sub>4</sub> systems must straddle the standard redox potentials. The conduction band edge (CBE) of monolayer MoSi<sub>2</sub>N<sub>4</sub> is about 0.71 eV, higher than the H<sup>+</sup>/H<sub>2</sub> re-

duction level. The valence band edge (VBE) is about 0.19 eV, lower than the  $O_2/H_2O$  oxidation level. Band edges of monolayer  $MoSi_2N_4$  straddle the water redox potentials in both highly acidic and neutral conditions (Fig. 19(a)). In contrast, the band edges of monolayer  $WSi_2N_4$  ( $WGe_2N_4$ ) only satisfy the standard in the highly acidic (neutral) condition [47, 123]. Group-IVB  $MSi_2N_4$  nanosheets with appropriate band edges are considered as the most suitable materials among 2D  $MA_2Z_4$  family for both water splitting and  $CO_2$  reduction application [120]. It is revealed that adatoms reduce the bandgap of  $MoSi_2N_4$  and further promote the possibility of photocatalytic process [127, 128, 176]. The CBE of  $Au-MoSi_2N_4$  is closer to the level for  $CO_2/HCOOH$  reduction and thus can easily transfer charges to  $CO_2$  and produce natural gas ( $HCOOH$ ,  $HCHO$ ,  $CO$ ,  $CH_4$ , and  $CH_3OH$ ). The VBE of  $Au-MoSi_2N_4$  approaching to the  $O_2/H_2O$  redox potential is beneficial for the interaction between holes and  $H_2O$ , and restrains the electron-hole recombination (Fig. 19(b)) [127]. Meanwhile, Li and Na absorption can improve the capacity of water splitting by using  $MoSi_2N_4$  [128]. The adjustable CBE and VBE are observed in  $MA_2Z_4$ -based heterostructures (e.g., BlueP/, InSe/ and  $MoSiGeN_4/MoSi_2N_4$ ) [104, 117, 125, 177–179], providing more possibility of this family for photocatalytic devices.

The other important factor of photocatalysis is the absorption of reactive atoms or molecules, which determines the electron transition to the surface and the charge utilization for redox reactions. The optimal site for hydrogen or  $CO_2$  absorption in monolayer  $MA_2Z_4$  is reported as Z site due to the lowest spontaneous binding energy compared with other sites [120, 180]. The Gibbs free energy for the hydrogen adsorption ( $\Delta G_{H^*}$ ) on monolayer  $MoSi_2N_4$  and  $WSi_2N_4$  is calculated to be 2.51 and 2.79 eV, respectively, which is much larger than the ideal value ( $\Delta G_{H^*} = 0$  eV). This indicates the weak binding of hydrogen in pristine monolayer  $MSi_2N_4$  ( $M = Mo/W$ ) and inertial hydrogen evolution reaction (HER) activity [180]. The HER performance of  $MSi_2N_4$ , as well as  $N_2$  reduction reaction (NRR), can be triggered by introducing N-site vacancy [180–183]. As shown in Fig. 20, it is obvious that the vacancy significantly influence  $\Delta G_{H^*}$ .  $\Delta G_{H^*}$  is decreased about 2–3 times by M-site vacancy and approaches to zero by N-site vacancy ( $\Delta G_{H^*} = -0.14$  eV in  $MoSi_2N_4$  and  $-0.02$  eV in  $WSi_2N_4$ ). This manifests that the HER performance of  $MSi_2N_4$  with the outermost N-site vacancy is comparable with and even better than that of Pt. On the other hand, transition metallic atomic doping and strain engineering are verified as the effective strategies to tune  $\Delta G_{H^*}$  and trigger HER, oxygen evolution reaction (OER) or oxygen reduction reaction (ORR) activity [182, 184, 185]. Particularly,  $|\Delta G_{H^*}|$  is calculated as only 0.05 eV in  $WSi_2N_4$  with Fe-doping at Si-site. A 3% tensile strain results in  $\Delta G_{H^*} = 0.015$  eV in  $NbGe_2N_4$ .

In the  $MA_2Z_4$  family, there exist other good photocatalysts with appropriate  $\Delta G$  [122, 131, 186, 187], for ex-

amples  $TiSi_2N_4$ ,  $HfA_2Z_4$ ,  $ZrA_2Z_4$ , Janus  $MSiGeN_4$ , etc. Recently, a theoretical method in multilevel is proposed to screen appropriate candidates for hydrogen evolution in  $MA_2Z_4$  family [186]. There exist four screening criteria: (1) small structural deformation after hydrogen absorption to maintain the potential stability during the HER processes, (2) low absolute value of Gibbs free energy ( $|\Delta G| \rightarrow 0$ ) with hydrogen adsorption, (3) suitable bandgaps, (4) high environmental stability. Taking these factors in mind, the multilevel screening workflow discovers seven  $MA_2Z_4$  with great stability and highly active HER among 144  $MA_2Z_4$  structures, i.e.,  $\alpha_1-VGe_2N_4$ ,  $\alpha_1-NbGe_2N_4$ ,  $\alpha_1-TaGe_2N_4$ ,  $\alpha_1-NbSi_2N_4$ ,  $\alpha_2-VGe_2N_4$ ,  $\alpha_2-NbGe_2N_4$ , and  $\alpha_2-TiGe_2P_4$ . Monolayer  $\alpha_1-NbSi_2N_4$  with the lowest formation energy is considered as the most promising 2D  $MA_2Z_4$  material for the HER application along the synthesis routine. At low H coverage ( $\theta < 25\%$ ), the optimal  $|\Delta G|$  of these seven  $MA_2Z_4$  is lower than 0.1 eV, which is comparable with or even superior to that of Pt ( $-0.09$  eV at  $\theta = 25\%$ ). A descriptor ( $E_{LUS}$ ) is proposed as energy level of the lowest unoccupied state to evaluate the capacity of H adsorption, since hydrogen adsorption is often accompanied with the electron transition to the CBM (for semiconductors) or the Fermi level (for metals). A higher  $E_{LUS}$  is prone to restraining electron filling and causing weaker H adsorption. On the contrary, a lower  $E_{LUS}$  represents the higher ability of H adsorption. Compared with  $\alpha_1-MoSi_2N_4$ ,  $\alpha_1-NbSi_2N_4$  with lower  $E_{LUS}$  shows higher activity toward HER.

HER performance of monolayer  $MA_2Z_4$  family is also examined by the combination of DFT calculations and machine learning algorithms including support vector regression (SVR), kernel ridge regression (KRR), random forest regression (RFR), extreme gradient boosting regression (XGBR), least absolute shrinkage, and selection operator (LASSO) [187].  $\Delta G_{H^*}$  and Gibbs free energy of deuterium ( $\Delta G_{D^*}$ ) can be accurately and rapidly predicted via XGBR by using only simple genetic programming processed elemental features, with a low predictive root-mean-square error of 0.14 eV.  $\Delta G_{H^*}$  of group-VB  $MA_2Z_4$  is closer to zero, indicating the excellent HER capacity. For example,  $TaSn_2P_4$  (0.07 eV) has a similar absolute value of  $\Delta G_{H^*}$  as  $NbSn_2P_4$  ( $-0.05$  eV), while  $\Delta G_{H^*}$  of  $CrSn_2P_4$  (0.23 eV) is nearly 3.5 times higher than that of  $TaSn_2P_4$  (0.07 eV). It can be concluded that M element is the crucial factor for the HER performance of  $MA_2Z_4$  materials. In addition,  $NbSi_2N_4$  with  $\Delta G_{H^*} = -0.041$  eV and  $\Delta G_{D^*} = -0.102$  eV, as well as  $VSi_2N_4$  with  $\Delta G_{H^*} = 0.024$  eV and  $\Delta G_{D^*} = -0.033$  eV is screened as the best HER and deuterium evolution reaction (DER) catalysts among the  $MA_2Z_4$  family.

As for ORR, the four-electron ( $4e^-$ ) mechanism favors the production of  $H_2O$ . The order of ORR activity is  $MGe_2As_4 > MSi_2As_4 > MSi_2N_4 > MSi_2P_4 > MGe_2P_4 \approx MGe_2N_4$  [188]. Among them,  $VGe_2As_4$ ,  $CrGe_2As_4$ ,  $VSi_2As_4$  and  $NbSi_2As_4$  are screened out to be highly promising electrocatalysts with a small overpotential

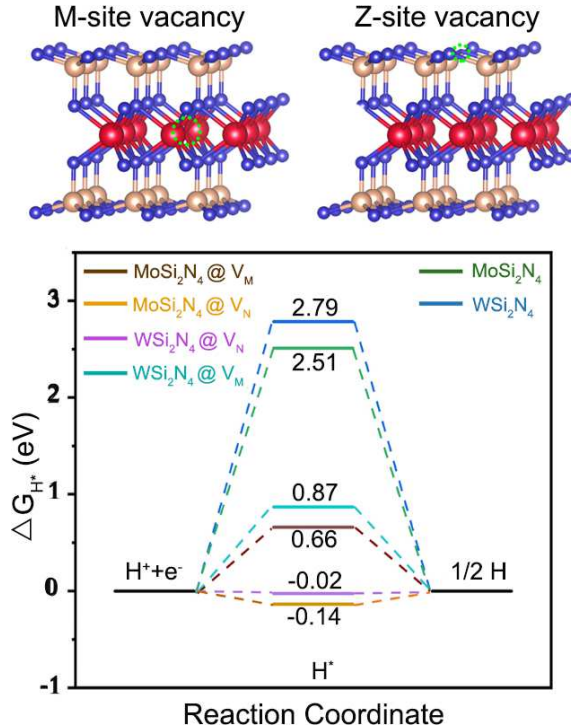


FIG. 20. Crystal structures of monolayer  $\text{MSi}_2\text{N}_4$  with M- ( $\text{V}_\text{M}$ ) and Z-site ( $\text{V}_\text{N}$ ) vacancy, and the corresponding Gibbs free energy diagram of HER processing. [180]

around 0.5–0.6 V. The topmost surface As acts as the active site, and the p-band center of the As atom shows correlation with the adsorption strength of the critical intermediate. Zhang et al. [189] efficiently screened photocatalytic OER catalysts in  $\text{MA}_2\text{Z}_4$  family via an automated high-throughput workflow. They found the adsorption ability of O atoms determines the catalytic effect.  $\beta_2\text{-ZrSi}_2\text{N}_4$  and  $\beta_2\text{-HfSi}_2\text{N}_4$  are considered as the efficient photocatalytic OER catalysts. In particular,  $\text{CrGe}_2\text{As}_4$  exhibits outstandingly high ORR activity with ultralow overpotential (0.49 V), which is comparable with the Pt-based catalysts. The metallic conductivity, as well as the moderate adsorption and orbital hybridization between As and  $\text{O}^*$  intermediate, is responsible for the exceptional activity [188].

### C. Batteries

Metal-air batteries have great advantages of high-energy-density metal anodes, active air cathodes, light weight, and simple structure, which are convenient to utilize in portable equipments. Bilayer or multilayer vdW  $\text{MoSi}_2\text{N}_4$  shows great potential application as electrodes (both anode and cathode) of Zn-air batteries [191]. On the anode side, the maximum theoretical capacity of Zn in  $\text{MoSi}_2\text{N}_4$  is up to 257 mAh/g. While on the cathode side,  $\text{O}_2$  reduction reaction on the  $\text{MoSi}_2\text{N}_4$  surface is more efficient than the general sluggish four-

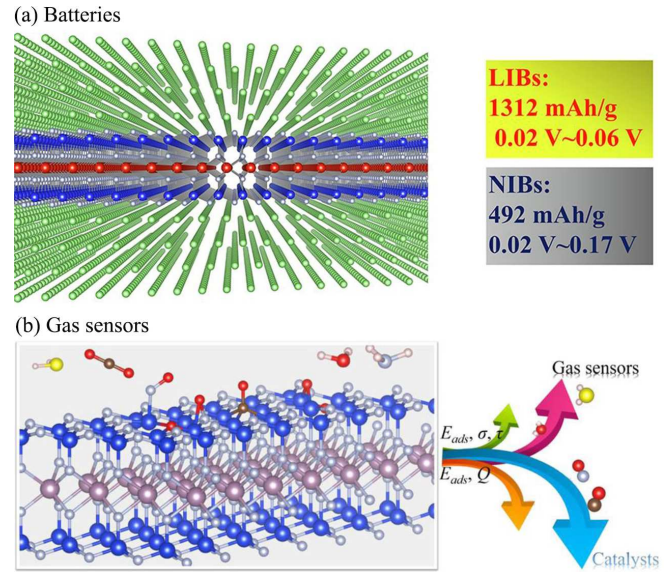


FIG. 21. Diagram of monolayer  $\text{MA}_2\text{Z}_4$  family in applications of (a) Li-Na batteries and (b) gas sensors. [45, 190]

electron aqueous  $\text{O}_2$  redox reactions. Furthermore,  $\text{VSi}_2\text{N}_4$  provides two critical specifications (high specific capacity and full battery open-circuit voltage) for the high-performance secondary Li-ion or Na-ion batteries (LIBs/NIBs) (Fig. 21(a)) [190]. The ionic capacity is up to 1312 mAh/g for Li and 492 mAh/g and Na, while the average open-circuit voltages are 0.02–0.06 V for LIBs, and 0.02–0.17 V for NIBs.

### D. Sensors

Environmental dependence of physical properties of 2D materials promotes the development of potential applications, e.g., sensors [192–196]. Gas sensor is one of the significant device for detecting gas molecules, especially contaminated and poisonous ones, which can be utilized in the field of industrial harm evaluation, cultivation of agricultural products, assessment of medical drugs, etc. The physisorption behaviors of gas molecules of monolayer  $\text{MoSi}_2\text{N}_4$  by spin-polarized DFT calculations have been investigated [45, 197]. Due to the weak interaction and small charge transfer, the gas molecules are physically adsorbed on the  $\text{MoSi}_2\text{N}_4$  surface (Fig. 21(b)). The results show that  $\text{H}_2$ ,  $\text{N}_2$ ,  $\text{CO}$ ,  $\text{CO}_2$ ,  $\text{NO}$ ,  $\text{NO}_2$ ,  $\text{H}_2\text{O}$ ,  $\text{H}_2\text{S}$ ,  $\text{NH}_3$  and  $\text{CH}_4$  molecules reduce the bandgap of  $\text{MoSi}_2\text{N}_4$  (from 1.73 eV to 1.50 eV) [197]. While the absorption of  $\text{O}_2$ ,  $\text{NO}_2$  and  $\text{SO}_2$  molecules obviously influences the electronic properties of  $\text{MoSi}_2\text{N}_4$  and even induces the spin polarization with magnetic moments ( $1\text{--}2 \mu_\text{B}$ ). The magnitude of magnetic moments is sensitive to the concentration of gas molecules, which increases with the increment of concentration of  $\text{NO}_2$  but decreases with the increment of concentration of  $\text{SO}_2$ . This indicates that  $\text{MoSi}_2\text{N}_4$ -based gas sensor has a high application poten-

tial for  $O_2$ ,  $NO$ ,  $NO_2$  and  $SO_2$  detection. Furthermore, the introduction of N vacancy into  $MoSi_2N_4$  improves the absorption performance [45], resulting in  $MoSi_2N_4$  with promising prospects in highly sensitive and reusable gas sensors of  $H_2O$  and  $H_2S$  molecules.

#### IV. SUMMARY AND OUTLOOK

In summary, the experimental achievements have brought novel 2D monolayer  $MoSi_2N_4$  and  $WSi_2N_4$ , while theoretical predictions have provided much more possibility of the emerging  $MA_2Z_4$  family due to the structural complexity and component diversity. In this review, we have summarized the latest progress of this novel 2D  $MA_2Z_4$  family with a focus on its physical and chemical properties, as well as its promising applications. Different from transition metal carbides, nitrides and dichalcogenides, this family exhibits more affluent and intriguing features, such as excellent mechanical properties, interesting electronic properties (from insulator to semiconductor to metal) related to the number of total valence electrons, wide range of thermal conductivity ( $10^1$ – $10^3$   $Wm^{-1}K^{-1}$ ), high optical absorption of visible and ultraviolet light, spin-valley effect, etc. Moreover, the properties of  $MA_2Z_4$  family are manipulable by external fields, providing more degrees of freedom to realize some specific applications. Strain engineering is demonstrated to shrink the band structure of  $MoSi_2N_4$  and induce the well-known ‘Mexican hat’, as well as result in an obvious shift in absorption spectra. By the layered strategy, semiconducting  $MA_2Z_4$ -based vdW heterostructures have promising applications in photocatalysts, while metallic ones effectively reduce the Schottky barrier height and are beneficial for the energy efficient and high-performance power devices. Finally, we survey the perspective applications of  $MA_2Z_4$ , from the aspects of transistors, photocatalysts, batteries, and sensors.

The emerging 2D  $MA_2Z_4$  family with versatile properties and applications opens the mind of low-dimensional structural designs and provides the new possibilities and opportunities to the development of 2D materials. As an outlook, there exist considerable spaces to further understand and exploit the emerging  $MA_2Z_4$  family.

- Firstly, the experience of synthesizing 2D  $MA_2Z_4$  could inspire the idea of synthesizing other 2D materials without knowing their bulk counterparts. Experimental attempts following or beyond the synthesis strategy for monolayer  $MoSi_2N_4$  are intriguing for the advent of new synthetic 2D materials.

- Secondly, since the development of interdisciplinary,

the attention to a potential material is no longer limited to some excellent characteristics. The synergistic effect of multiphysics for practical applications should also be the focus. Although the excellent properties of 2D  $MA_2Z_4$  family have been revealed, synergy of multiphysics coupling would be a crucial method to integrate the versatile properties and maximize their advantages, and even emanate more novel sparks.

- Thirdly, most of the current theoretical predictions on 2D  $MA_2Z_4$  family are made by first-principles calculations. It is highly recommended that modeling and simulation methodologies across scales be developed to understand 2D  $MA_2Z_4$  from electronic, atomistic, microstructure, to device level.

- Fourthly, the sandwich structure of 2D  $MA_2Z_4$  enables more degrees of freedom to elaborate properties and functionalities, calling for more extensive efforts. For instance, the engineering of 2D  $MA_2Z_4$  by asymmetric design of its two sides could be further explored to achieve more versatile structures and functionalities, such as ferroelectricity, multiferroics, Janus structures, etc.

- Fifthly, multilayer or  $MA_2Z_4$ -based vdW heterostructures show great potential in nanodevices. The practical application of 2D  $MA_2Z_4$  family requires more reasonable designs and attempts (e.g., assemble and stacking way, interlayer adaptability, in-plane heterostructure, etc.) to ensure the reliable realization of their advantages.

- Last but not least, the successful preparation of semiconducting monolayer  $MoSi_2N_4$  and  $WSi_2N_4$  by CVD provides the appropriate growth method for this family. However, most of the reported structures, properties, functionalities, and applications of 2D  $MA_2Z_4$  are from the theoretical predictions. Continuous experimental efforts are mandatory to verify the existence of other members (e.g., magnetic  $VSi_2N_4$  and  $VSi_2P_4$ ) as well as the theoretically predicted properties, applications, and devices.

#### ACKNOWLEDGMENT

The authors acknowledge the support from the National Natural Science Foundation of China (NSFC 11902150, 12272173), 15th Thousand Youth Talents Program of China, the Research Fund of State Key Laboratory of Mechanics and Control of Mechanical Structures (MCMS-I-0419G01 and MCMS-I-0421K01), the Fundamental Research Funds for the Central Universities (1001-XAC21021), and a project Funded by the Priority Academic Program Development of Jiangsu Higher Education Institutions.

[1] D. Akinwande, C. J. Brennan, J. S. Bunch, P. Egberts, J. R. Felts, H. Gao, R. Huang, J. S. Kim, T. Li,

Y. Li, K. M. Liechti, N. Lu, H. S. Park, E. J. Reed, P. Wang, B. I. Yakobson, T. Zhang, Y. W. Zhang,

Y. Zhou, and Y. Zhu, A review on mechanics and mechanical properties of 2D materials—Graphene and beyond, *Extreme Mechanics Letters* **13**, 42 (2017).

[2] C. Lee, X. Wei, J. W. Kysar, and J. Hone, Measurement of the elastic properties and intrinsic strength of monolayer graphene, *Science* **321**, 385 (2008).

[3] S. Bertolazzi, J. Brivio, and A. Kis, Stretching and breaking of ultrathin MoS<sub>2</sub>, *ACS Nano* **5**, 9703 (2011).

[4] A. A. Balandin, Thermal properties of graphene and nanostructured carbon materials, *Nature Materials* **10**, 569 (2011).

[5] D. Li, J. Gao, P. Cheng, J. He, Y. Yin, Y. Hu, L. Chen, Y. Cheng, and J. Zhao, 2D boron sheets: Structure, growth, and electronic and thermal transport properties, *Advanced Functional Materials* **30**, 1904349 (2020).

[6] X. Qian, J. Zhou, and G. Chen, Phonon-engineered extreme thermal conductivity materials, *Nature Materials* **20**, 1188 (2021).

[7] C. Wang, B. Lian, X. Guo, J. Mao, Z. Zhang, D. Zhang, B. L. Gu, Y. Xu, and W. Duan, Type-II Ising superconductivity in two-dimensional materials with spin-orbit coupling, *Physical Review Letters* **123**, 126402 (2019).

[8] J. Bekaert, M. Petrov, A. Aperis, P. M. Oppeneer, and M. V. Milošević, Hydrogen-induced high-temperature superconductivity in two-dimensional materials: The example of hydrogenated monolayer MgB<sub>2</sub>, *Physical Review Letters* **123**, 077001 (2019).

[9] W. Li, J. Huang, X. Li, S. Zhao, J. Lu, Z. V. Han, and H. Wang, Recent progresses in two-dimensional Ising superconductivity, *Materials Today Physics* **21**, 100504 (2021).

[10] X. Liu, Z. Hao, K. Watanabe, T. Taniguchi, B. I. Halperin, and P. Kim, Interlayer fractional quantum Hall effect in a coupled graphene double layer, *Nature Physics* **15**, 893 (2019).

[11] Q. Shi, E. M. Shih, M. V. Gustafsson, D. A. Rhodes, B. Kim, K. Watanabe, T. Taniguchi, Z. Papić, J. Hone, and C. R. Dean, Odd- and even-denominator fractional quantum Hall states in monolayer WSe<sub>2</sub>, *Nature Nanotechnology* **15**, 569 (2020).

[12] K. S. Novoselov, A. K. Geim, S. V. M. D. Jiang, Y. Zhang, S. V. Dubonos, I. V. Grigorieva, and A. A. Firsov, Electric field effect in atomically thin carbon films, *Science* **306**, 666 (2004).

[13] G. AK, Graphene: Status and prospects, *Science* **324**, 1530 (2009).

[14] M. Yi and Z. Shen, A review on mechanical exfoliation for the scalable production of graphene, *Journal of Materials Chemistry A* **3**, 11700 (2015).

[15] K. S. Novoselov, D. Jiang, F. Schedin, T. J. Booth, V. V. Khotkevich, S. V. Morozov, and A. K. Geim, Two-dimensional atomic crystals, *Proceedings of the National Academy of Sciences of the United States of America* **102**(20)0451 (2005).

[16] A. K. Geim and I. V. Grigorieva, Van der Waals heterostructures, *Nature* **499**, 419 (2013).

[17] M. M. Otrokov, I. I. Klimovskikh, H. Bentmann, D. Estyunin, A. Zeugner, Z. S. Aliev, S. Gaß, A. U. Wolter, A. V. Koroleva, A. M. Shikin, M. Blanco-Rey, M. Hoffmann, I. P. Rusinov, A. Y. Vyačazovskaya, S. V. Eremin, Y. M. Koroteev, V. M. Kuznetsov, F. Freyse, J. Sánchez-Barriga, I. R. Amiraslanov, M. B. Babanly, N. T. Mamedov, N. A. Abdullayev, V. N. Zverev, A. Alfonsov, V. Kataev, B. Büchner, E. F. Schwier, S. Kumer, A. Kimura, L. Petaccia, G. Di Santo, R. C. Vidal, S. Schatz, K. Kißner, M. Ünzelmann, C. H. Min, S. Moser, T. R. Peixoto, F. Reinert, A. Ernst, P. M. Echenique, A. Isaeva, and E. V. Chulkov, Prediction and observation of an antiferromagnetic topological insulator, *Nature* **576**, 416 (2019).

[18] R. Dong, T. Zhang, and X. Feng, Interface-assisted synthesis of 2D materials: Trend and challenges, *Chemical Reviews* **118**, 6189 (2018).

[19] Y. Huang, Y. H. Pan, R. Yang, L. H. Bao, L. Meng, H. L. Luo, Y. Q. Cai, G. D. Liu, W. J. Zhao, Z. Zhou, L. M. Wu, Z. L. Zhu, M. Huang, L. W. Liu, L. Liu, P. Cheng, K. H. Wu, S. B. Tian, C. Z. Gu, Y. G. Shi, Y. F. Guo, Z. G. Cheng, J. P. Hu, L. Zhao, G. H. Yang, E. Sutter, P. Sutter, Y. L. Wang, W. Ji, X. J. Zhou, and H. J. Gao, Universal mechanical exfoliation of large-area 2D crystals, *Nature Communications* **11**, 2453 (2020).

[20] M. Yi, Z. Shen, W. Zhang, J. Zhu, L. Liu, S. Liang, X. Zhang, and S. Ma, Hydrodynamics-assisted scalable production of boron nitride nanosheets and their application in improving oxygen-atom erosion resistance of polymeric composites, *Nanoscale* **5**, 10660 (2013).

[21] M. Yi and Z. Shen, Kitchen blender for producing high-quality few-layer graphene, *Carbon* **78**, 622 (2014).

[22] M. Yi and Z. Shen, Fluid dynamics: An emerging route for the scalable production of graphene in the last five years, *RSC Advances* **6**, 72525 (2016).

[23] A. J. Mannix, X. F. Zhou, B. Kiraly, J. D. Wood, D. Alducin, B. D. Myers, X. Liu, B. L. Fisher, U. Santiago, J. R. Guest, M. J. Yacaman, A. Ponce, A. R. Oganov, M. C. Hersam, and N. P. Guisinger, Synthesis of borophenes: Anisotropic, two-dimensional boron polymorphs, *Science* **350**, 1513 (2015).

[24] B. Feng, J. Zhang, Q. Zhong, W. Li, S. Li, H. Li, P. Cheng, S. Meng, L. Chen, and K. Wu, Experimental realization of two-dimensional boron sheets, *Nature Chemistry* **8**, 563 (2016).

[25] Y. Zhan, Z. Liu, S. Najmaei, P. M. Ajayan, and J. Lou, Large-area vapor-phase growth and characterization of MoS<sub>2</sub> atomic layers on a SiO<sub>2</sub> substrate, *Small* **8**, 966 (2012).

[26] Y. Zhang, Y. Yao, M. G. Sendeku, L. Yin, X. Zhan, F. Wang, Z. Wang, and J. He, Recent progress in CVD growth of 2D transition metal dichalcogenides and related heterostructures, *Advanced Materials* **31**, 1901694 (2019).

[27] K. S. Novoselov, A. Mishchenko, A. Carvalho, and A. H. Castro Neto, 2D materials and van der Waals heterostructures, *Science* **353**, 6298 (2016).

[28] Y. L. Hong, Z. Liu, L. Wang, T. Zhou, W. Ma, C. Xu, S. Feng, L. Chen, M. L. Chen, D. M. Sun, X. Q. Chen, H. M. Cheng, and W. Ren, Chemical vapor deposition of layered two-dimensional MoSi<sub>2</sub>N<sub>4</sub> materials, *Science* **319**(6670)1220 (2005).

[29] L. Wang, Y. Shi, M. Liu, A. Zhang, Y. L. Hong, R. Li, Q. Gao, M. Chen, W. Ren, H. M. Cheng, Y. Li, and X. Q. Chen, Intercalated architecture of MA<sub>2</sub>Z<sub>4</sub> family layered van der Waals materials with emerging topological, magnetic and superconducting properties, *Nature Communications* **12**, 2361 (2021).

[30] J. S. Yang, L. Zhao, S. Q. Li, H. Liu, L. Wang, M. Chen, J. Gao, and J. Zhao, Accurate electronic properties and non-linear optical response of two-dimensional MA<sub>2</sub>Z<sub>4</sub>, *Nanoscale* **13**, 5479 (2021).

[31] L. Kang and Z. Lin, Second harmonic generation of  $\text{MoSi}_2\text{N}_4$ -type layers, *Physical Review B* **103**, 195404 (2021).

[32] D. Liang, S. Xu, P. Lu, and Y. Cai, Highly tunable and strongly bound exciton in  $\text{MoSi}_2\text{N}_4$  via strain engineering, *Physical Review B* **105**, 195302 (2022).

[33] D. Huang, F. Liang, R. Guo, D. Lu, J. Wang, H. Yu, and H. Zhang,  $\text{MoSi}_2\text{N}_4$ : A 2D regime with strong exciton-phonon coupling, *Advanced Optical Materials* **10**, 2102612 (2022).

[34] Z. Wang, X. Kuang, G. Yu, P. Zhao, H. Zhong, and S. Yuan, Electronic properties and quasiparticle model of monolayer, *Physical Review B* **104**, 155110 (2021).

[35] J. Zhao, X. Jin, H. Zeng, C. Yao, and G. Yan, Spin-valley coupling and valley splitting in the  $\text{MoSi}_2\text{N}_4/\text{CrCl}_3$  van der Waals heterostructure, *Applied Physics Letters* **119**, 213101 (2021).

[36] L. Yan, B. T. Wang, X. Huang, Q. Li, K. Xue, J. Zhang, W. Ren, and L. Zhou, Surface passivation induced a significant enhancement of superconductivity in layered two-dimensional  $\text{MSi}_2\text{N}_4$  ( $\text{M} = \text{Ta}$  and  $\text{Nb}$ ) materials, *Nanoscale* **13**, 18947 (2021).

[37] X. Zhou, R. W. Zhang, Z. Zhang, W. Feng, Y. Mokrousov, and Y. Yao, Sign-reversible valley-dependent Berry phase effects in 2D valley-half-semiconductors, *npj Computational Materials* **7**, 160 (2021).

[38] Y. Wang, D. Legut, X. Liu, Y. Li, C. Li, Y. Sun, R. Zhang, and Q. Zhang, Mott transition and superexchange mechanism in magnetically doped  $\text{XSi}_2\text{N}_4$  caused by large 3d orbital onsite Coulomb interaction, *Physical Review B* **106**, 104421 (2022).

[39] Z. Cui, Y. Luo, J. Yu, and Y. Xu, Tuning the electronic properties of  $\text{MoSi}_2\text{N}_4$  by molecular doping: A first principles investigation, *Physica E: Low-Dimensional Systems and Nanostructures* **134**, 11873p (2021).

[40] W. Zhou, L. Wu, A. Li, B. Zhang, and F. Ouyang, Structural symmetry, spin-Orbit coupling, and valley-related properties of monolayer  $\text{WSi}_2\text{N}_4$  family, *Journal of Physical Chemistry Letters* **12**, 11622 (2021).

[41] R. Islam, B. Ghosh, C. Autieri, S. Chowdhury, A. Bansil, A. Agarwal, and B. Singh, Tunable spin polarization and electronic structure of bottom-up synthesized  $\text{MoSi}_2\text{N}_4$  materials, *Physical Review B* **104**, L201112 (2021).

[42] Q. Wu and L. K. Ang, Giant tunneling magnetoresistance in atomically thin  $\text{VSi}_2\text{N}_4/\text{MoSi}_2\text{N}_4/\text{VSi}_2\text{N}_4$  magnetic tunnel junction, *Applied Physics Letters* **120**, 022401 (2022).

[43] H. Ma, W. Zhao, Q. Zhang, D. Liu, H. Ren, H. Zhu, Y. Chi, F. Ding, and W. Guo, Chemical environment dependent stabilities, electronic properties and diffusions behaviors of intrinsic point defects in novel two-dimensional  $\text{MoSi}_2\text{N}_4$  monolayer, *Applied Surface Science* **592**, 153214 (2022).

[44] H. Zhao, G. Yang, Y. Liu, X. Yang, Y. Gu, C. Wei, Z. Xie, Q. Zhang, B. Bian, X. Zhang, X. Huo, and N. Lu, Quantum transport of sub-10 nm monolayer  $\text{WGe}_2\text{N}_4$  transistors, *ACS Applied Electronic Materials* **3**, 5086 (2021).

[45] C. Xiao, Z. Ma, R. Sa, Z. Cui, S. Gao, W. Du, X. Sun, and Q. H. Li, Adsorption behavior of environmental gas molecules on pristine and defective  $\text{MoSi}_2\text{N}_4$ : Possible application as highly sensitive and reusable gas sensors, *ACS Omega* **7**, 8706 (2022).

[46] Y. Gao, J. Liao, H. Wang, Y. Wu, Y. Li, K. Wang, C. Ma, S. Gong, T. Wang, X. Dong, Z. Jiao, and Y. An, Electronic transport properties and nanodevice designs for monolayer  $\text{MoSi}_2\text{P}_4$ , *Physical Review Applied* **18**, 034033 (2022).

[47] B. Mortazavi, B. Javvaji, F. Shojaei, T. Rabczuk, A. V. Shapeev, and X. Zhuang, Exceptional piezoelectricity, high thermal conductivity and stiffness and promising photocatalysis in two-dimensional  $\text{MoSi}_2\text{N}_4$  family confirmed by first-principles, *Nano Energy* **82**, 105716 (2021).

[48] X. Liu, H. Zhang, Z. Yang, Z. Zhang, X. Fan, and H. Liu, Structure and electronic properties of  $\text{MoSi}_2\text{P}_4$  monolayer, *Physics Letters A* **420**, 127751 (2021).

[49] Y. Yin, M. Yi, and W. Guo, High and anomalous thermal conductivity in monolayer  $\text{MSi}_2\text{Z}_4$  semiconductors, *ACS Applied Materials & Interfaces* **13**, 45907 (2021).

[50] G. H. Lee, R. C. Cooper, S. J. An, S. Lee, A. Van Der Zande, N. Petrone, A. G. Hammerberg, C. Lee, B. Crawford, W. Oliver, J. W. Kysar, and J. Hone, High-strength chemical-vapor-deposited graphene and grain boundaries, *Science* **340**, 1074 (2013).

[51] K. Liu, Q. Yan, M. Chen, W. Fan, Y. Sun, J. Suh, D. Fu, S. Lee, J. Zhou, S. Tongay, J. Ji, J. B. Neaton, and J. Wu, Elastic properties of chemical-vapor-deposited monolayer  $\text{MoS}_2$ ,  $\text{WS}_2$ , and their bilayer heterostructures, *Nano Letters* **14**, 5097 (2014).

[52] R. Zhang, V. Koutsos, and R. Cheung, Elastic properties of suspended multilayer  $\text{WSe}_2$ , *Applied Physics Letters* **108**, 042104 (2016).

[53] A. Lipatov, H. Lu, M. Alhabeb, B. Anasori, A. Gruverman, Y. Gogotsi, and A. Sinitskii, Elastic properties of 2D  $\text{Ti}_3\text{C}_2\text{T}_x$  MXene monolayers and bilayers, *Science advances* **4**, eaat0491 (2018).

[54] M. Alhabeb, H. Lu, S. Zhao, M. J. Loes, N. S. Vorobeva, Y. Dall'Agnese, Y. Gao, A. Gruverman, Y. Gogotsi, and A. Sinitskii, Electrical and elastic properties of individual single-layer  $\text{Nb}_4\text{C}_3\text{T}_x$  MXene flakes, *Advanced Electronic Materials* **6**, 1901382 (2020).

[55] Q. Wei and X. Peng, Superior mechanical flexibility of phosphorene and few-layer black phosphorus, *Applied Physics Letters* **104**, 251915 (2014).

[56] Q. Li, W. Zhou, X. Wan, and J. Zhou, Strain effects on monolayer  $\text{MoSi}_2\text{N}_4$ : Ideal strength and failure mechanism, *Physica E: Low-Dimensional Systems and Nanostructures* **131**, 114 (2021).

[57] A. Bafeekry, M. Faraji, D. M. Hoat, M. Shahrokhian, M. M. Fadlallah, F. Shojaei, S. A. H. Feghhi, M. Ghergherehchi, and D. Gogova,  $\text{MoSi}_2\text{N}_4$  single-layer: A novel two-dimensional material with outstanding mechanical, thermal, electronic, optical, and photocatalytic properties, *Journal of Physics D: Applied Physics* **54**, 155303 (2021).

[58] C. A. Marianetti and H. G. Yevick, Failure mechanisms of graphene under tension, *Physical Review Letters* **105**, 245502 (2010).

[59] T. Li, Ideal strength and phonon instability in single-layer  $\text{MoS}_2$ , *Physical Review B* **85**, 235407 (2012).

[60] B. Mortazavi, F. Shojaei, B. Javvaji, T. Rabczuk, and X. Zhuang, Outstandingly high thermal conductivity, elastic modulus, carrier mobility and piezoelectricity in two-dimensional semiconducting  $\text{CrC}_2\text{N}_4$ : A first-principles study,

Materials Today Energy **22**, 100839 (2021).

[61] M. Tian, C. Wei, J. Zhang, J. Wang, and R. Yang, Electronic, optical, and water solubility properties of two-dimensional layered  $\text{SnSi}_2\text{N}_4$  from first principles, *Physical Review B* **103**, 195305 (2021).

[62] V. D. Dat and T. V. Vu, Layered post-transition-metal dichalcogenide  $\text{SnGe}_2\text{N}_4$  as a promising photoelectric material: A DFT study, *RSC Advances* **12**, 10249 (2022).

[63] R. T. Sibatov, R. M. Meftakhtdinov, and A. I. Kochaev, Asymmetric  $\text{XMoSiN}_2$  ( $\text{X}=\text{S}$ ,  $\text{Se}$ ,  $\text{Te}$ ) monolayers as novel promising 2D materials for nanoelectronics and photovoltaics, *Applied Surface Science* **585**, 152465 (2022).

[64] S. D. Guo, Y. T. Zhu, W. Q. Mu, L. Wang, and X. Q. Chen, Structure effect on intrinsic piezoelectricity in septuple-atomic-layer  $\text{MSi}_2\text{N}_4$  ( $\text{M}=\text{Mo}$  and  $\text{W}$ ), *Computational Materials Science* **188**, 110223 (2021).

[65] S. D. Guo, Y. T. Zhu, W. Q. Mu, and W. C. Ren, Intrinsic piezoelectricity in monolayer  $\text{MSi}_2\text{N}_4$  ( $\text{M}=\text{Mo}$ ,  $\text{W}$ ,  $\text{Cr}$ ,  $\text{Ti}$ ,  $\text{Zr}$  and  $\text{Hf}$ ), *Europhysics Letters* **132**, 57002 (2020).

[66] K. A. N. Duerloo, M. T. Ong, and E. J. Reed, Intrinsic piezoelectricity in two-dimensional materials, *Journal of Physical Chemistry Letters* **3**, 2871 (2012).

[67] M. N. Blonsky, H. L. Zhuang, A. K. Singh, and R. G. Hennig, Ab initio prediction of piezoelectricity in two-dimensional materials, *ACS Nano* **9**, 9885 (2015).

[68] C. Cui, F. Xue, W. J. Hu, and L. J. Li, Two-dimensional materials with piezoelectric and ferroelectric functionalities, *npj 2D Materials and Applications* **2**, 18 (2018).

[69] C. M. Lueng, H. L. Chan, W. K. Fong, C. Surya, and C. L. Choy, Piezoelectric coefficients of aluminum nitride and gallium nitride, *Materials Research Society Symposium - Proceedings* **572**, 389 (1999).

[70] S. D. Guo, W. Q. Mu, Y. T. Zhu, and X. Q. Chen, Coexistence of intrinsic piezoelectricity and ferromagnetism induced by small biaxial strain in septuple-atomic-layer  $\text{VSi}_2\text{P}_4$ , *Physical Chemistry Chemical Physics* **22**, 28359 (2020).

[71] S. D. Guo, W. Q. Mu, Y. T. Zhu, R. Y. Han, and W. C. Ren, Predicted septuple-atomic-layer Janus  $\text{MSiGeN}_4$  ( $\text{M}=\text{Mo}$  and  $\text{W}$ ) monolayers with Rashba spin splitting and high electron carrier mobilities, *Journal of Materials Chemistry C* **9**, 2464 (2021).

[72] X. Guo and S. Guo, Janus  $\text{MSiGeN}_4$  ( $\text{M}=\text{Zr}$  and  $\text{Hf}$ ) monolayers derived from centrosymmetric  $\beta\text{-MA}_2\text{Z}_4$ : A first-principles study, *Journal of Semiconductors* **42**, 122002 (2021).

[73] S. D. Guo, Y. T. Zhu, W. Q. Mu, and X. Q. Chen, A piezoelectric quantum spin Hall insulator with Rashba spin splitting in Janus monolayer  $\text{SrAlGaSe}_4$ , *Journal of Materials Chemistry C* **9**, 7465 (2021).

[74] T. Zhong, Y. Ren, Z. Zhang, J. Gao, and M. Wu, Sliding ferroelectricity in two-dimensional  $\text{MoA}_2\text{N}_4$  ( $\text{A}=\text{Si}$  or  $\text{Ge}$ ) bilayers: High polarizations and Moiré potentials, *Journal of Materials Chemistry A* **9**, 19659 (2021).

[75] Z. Fei, W. Zhao, T. A. Palomaki, B. Sun, M. K. Miller, Z. Zhao, J. Yan, X. Xu, and D. H. Cobden, Ferroelectric switching of a two-dimensional metal, *Nature* **560**, 336 (2018).

[76] L. Li and M. Wu, Binary compound bilayer and multilayer with vertical polarizations: Two-dimensional ferroelectrics, multiferroics, and nanogen-erators, *ACS Nano* **11**, 6382 (2017).

[77] X. Zhuang, B. He, B. Javvaji, and H. S. Park, Intrinsic bending flexoelectric constants in two-dimensional materials, *Physical Review B* **99**, 054105 (2019).

[78] L. Dong, J. Lou, and V. B. Shenoy, Large in-plane and vertical piezoelectricity in Janus transition metal dichalcogenides, *ACS Nano* **11**, 8242 (2017).

[79] B. Javvaji, B. He, X. Zhuang, and H. S. Park, High flexoelectric constants in Janus transition-metal dichalcogenides, *Physical Review Materials* **3**, 125402 (2019).

[80] J. Yu, J. Zhou, X. Wan, and Q. Li, High intrinsic lattice thermal conductivity in monolayer  $\text{MoSi}_2\text{N}_4$ , *New Journal of Physics* **23**, 033005 (2021).

[81] C. Shen, L. Wang, D. Wei, Y. Zhang, G. Qin, X. Q. Chen, and H. Zhang, Two-dimensional layered  $\text{MSi}_2\text{N}_4$  ( $\text{M}=\text{Mo}$ ,  $\text{W}$ ) as promising thermal management materials: A comparative study, *Physical Chemistry Chemical Physics* **24**, 3086 (2022).

[82] T. Li, G. Nie, and Q. Sun, Highly sensitive tuning of lattice thermal conductivity of grapheme-like borophene by fluorination and chlorination, *Nano Research* **13**, 1171 (2020).

[83] Y. Cai, J. Lan, G. Zhang, and Y. Zhang, Lattice vibrational modes and phonon thermal conductivity of monolayer  $\text{MoS}_2$ , *Physical Review B* **89**, 035438 (2014).

[84] X. Gu and R. Yang, Phonon transport in single-layer transition metal dichalcogenides: A first-principles study, *Applied Physics Letters* **105**, 131903 (2014).

[85] P. Torres, F. X. Alvarez, Cartoixà X., and R. Rurrali, Thermal conductivity and phonon hydrodynamics in transition metal dichalcogenides from first-principles, *2D Materials* **6**, 035002 (2019).

[86] P. Liu, T. Bo, J. Xu, W. Yin, J. Zhang, F. Wang, O. Eriksson, and B. T. Wang, First-principles calculations of the ultralow thermal conductivity in two-dimensional group-IV selenides, *Physical Review B* **98**, 235426 (2018).

[87] Y. Sun, Z. Shuai, and D. Wang, Reducing lattice thermal conductivity of the thermoelectric  $\text{SnSe}$  monolayer: Role of phonon-electron coupling, *Journal of Physical Chemistry C* **123**, 12001 (2019).

[88] A. A. Balandin, S. Ghosh, W. Bao, I. Calizo, and C. Lau, Superior thermal conductivity of single-layer graphene, *Nano Letters* **8**, 902 (2008).

[89] S. Ghosh, I. Calizo, D. Teweldebrhan, E. P. Pokatilov, D. Nika, A. A. Balandin, W. Bao, F. Miao, and C. N. Lau, Extremely high thermal conductivity of graphene: Prospects for thermal management applications in nanoelectronic circuits, *Applied Physics Letters* **92**, 151911 (2008).

[90] L. Lindsay and D. A. Broido, Enhanced thermal conductivity and isotope effect in single-layer hexagonal boron nitride, *Physical Review B* **84**, 155421 (2011).

[91] G. A. Slack, Anisotropic thermal conductivity of pyrolytic graphite, *Physical Reviews* **127**, 694 (1962).

[92] G. A. Slack, Nonmetallic crystals with high thermal conductivity, *Journal of Physics and Chemistry of Solids* **34**, 321 (1973).

[93] X. S. Guo and S. D. Guo, Tuning transport coefficients of monolayer  $\text{MoSi}_2\text{N}_4$  with biaxial strain, *Chinese Physics B* **30**, 067102 (2021).

[94] Y. Huang, X. Zhong, H. Yuan, and H. Chen, Thermoelectric performance of  $\text{MoSi}_2\text{As}_4$  monolayer, *Europhysics Letters* **137**, 16002 (2022).

[95] C. Zhang, F. Wei, X. Zhang, W. Chen, C. Chen, J. Hao, and B. Jia, Thermoelectric properties of monolayer  $\text{MoSi}_2\text{N}_4$  and  $\text{MoGe}_2\text{N}_4$  with large Seebeck coefficient and high carrier mobility: A first principles study, *Journal of Solid State Chemistry* **315**, 123447 (2022).

[96] H. Alavi-rad, Strain engineering in optoelectronic properties of  $\text{MoSi}_2\text{N}_4$  monolayer: Ultrahigh tunability, *Semiconductor Science and Technology* **37**, 065018 (2022).

[97] H. Zhong, W. Xiong, P. Lv, J. Yu, and S. Yuan, Strain-induced semiconductor to metal transition in  $\text{MA}_2\text{Z}_4$  bilayers ( $\text{M} = \text{Ti, Cr, Mo}$ ;  $\text{A} = \text{Si}$ ;  $\text{Z} = \text{N, P}$ ), *Physical Review B* **103**, 085124 (2021).

[98] Y. Ding and Y. Wang, Computational exploration of stable 4d/5d transition-metal  $\text{MSi}_2\text{N}_4$  ( $\text{M} = \text{Y-Cd}$  and  $\text{Hf-Hg}$ ) nanosheets and their versatile electronic and magnetic properties, *Journal of Physical Chemistry C* **125**, 19580 (2021).

[99] Y. Wu, Z. Tang, W. Xia, W. Gao, F. Jia, Y. Zhang, W. Zhu, W. Zhang, and P. Zhang, Prediction of protected band edge states and dielectric tunable quasiparticle and excitonic properties of monolayer  $\text{MoSi}_2\text{N}_4$ , *npj Computational Materials* **8**, 129 (2022).

[100] Y. Cai, G. Zhang, and Y. W. Zhang, Polarity-reversed robust carrier mobility in monolayer  $\text{MoS}_2$  nanoribbons, *Journal of the American Chemical Society* **136**, 6269 (2014).

[101] H. Yao, C. Zhang, Q. Wang, J. Li, Y. Yu, F. Xu, B. Wang, and Y. Wei, Novel two-dimensional layered  $\text{MoSi}_2\text{Z}_4$  ( $\text{Z} = \text{P, As}$ ): New promising optoelectronic materials, *Nanomaterials* **11**, 559 (2021).

[102] Q. Wu, L. Cao, Y. S. Ang, and L. K. Ang, Semiconductor-to-metal transition in bilayer  $\text{MoSi}_2\text{N}_4$  and  $\text{WSi}_2\text{N}_4$  with strain and electric field, *Applied Physics Letters* **118**, 113102 (2021).

[103] X. Cai, Z. Zhang, Y. Zhu, L. Lin, W. Yu, Q. Wang, X. Yang, X. Jia, and Y. Jia, A two-dimensional  $\text{MoSe}_2/\text{MoSi}_2\text{N}_4$  van der Waals heterostructure with high carrier mobility and diversified regulation of its electronic properties, *Journal of Materials Chemistry C* **9**, 10073 (2021).

[104] Y. He, Y. H. Zhu, M. Zhang, J. Du, W. H. Guo, S. M. Liu, C. Tian, H. X. Zhong, X. Wang, and J. J. Shi, High hydrogen production in the  $\text{InSe}/\text{MoSi}_2\text{N}_4$  van der Waals heterostructure for overall water splitting, *Physical Chemistry Chemical Physics* **24**, 2110 (2022).

[105] X. Cai, Z. Zhang, A. Song, G. Chen, W. Yu, X. Jia, X. Yang, Y. Liu, and Y. Jia, Indirect to direct bandgap transition and enhanced optoelectronic properties in  $\text{WSe}_2$  monolayer through forming  $\text{WSe}_2/\text{MoSi}_2\text{N}_4$  bilayer, *SSRN Electronic Journal* (2021).

[106] C. Q. Nguyen, Y. S. Ang, S. T. Nguyen, N. V. Hoang, N. M. Hung, and C. V. Nguyen, Tunable type-II band alignment and electronic structure of  $\text{C}_3\text{N}_4/\text{MoSi}_2\text{N}_4$  heterostructure: Interlayer coupling and electric field, *Physical Review B* **105**, 045303 (2022).

[107] J. Q. Ng, Q. Wu, L. K. Ang, and Y. S. Ang, Tunable electronic properties and band alignments of  $\text{MoSi}_2\text{N}_4/\text{GaN}$  and  $\text{MoSi}_2\text{N}_4/\text{ZnO}$  van der Waals heterostructures, *Applied Physics Letters* **120**, 103101 (2022).

[108] C. Liu, Z. Wang, W. Xiong, H. Zhong, and S. Yuan, Effect of vertical strain and in-plane biaxial strain on type-II  $\text{MoSi}_2\text{N}_4/\text{Cs}_3\text{Bi}_2\text{I}_9$  van der Waals heterostructure, *Journal of Applied Physics* **131**, 163102 (2022).

[109] Y. Guo, J. Min, X. Cai, L. Zhang, C. Liu, and Y. Jia, Two-dimensional type-II  $\text{BP}/\text{MoSi}_2\text{P}_4$  vdW heterostructures for high-performance solar cells, *Journal of Physical Chemistry C* **126**, 4677 (2022).

[110] C. Nguyen, N. V. Hoang, H. V. Phuc, A. Y. Sin, and C. V. Nguyen, Two-dimensional boron phosphide/ $\text{MoGe}_2\text{N}_4$  van der Waals heterostructure: A promising tunable optoelectronic material, *Journal of Physical Chemistry Letters* **12**, 5076 (2021).

[111] Q. Liang, X.-y. Luo, Y.-x. Wang, Y.-c. Liang, and Q. Xie, Modulation of Schottky barrier in  $\text{XSi}_2\text{N}_4$  / graphene ( $\text{X}=\text{Mo}$  and  $\text{W}$ ) heterojunctions by biaxial strain, *Chinese Physics B* **31**, 087101 (2022).

[112] L. Cao, G. Zhou, Q. Wang, L. K. Ang, and Y. S. Ang, Two-dimensional van der Waals electrical contact to monolayer  $\text{MoSi}_2\text{N}_4$ , *Applied Physics Letters* **118**, 013106 (2021).

[113] K. D. Pham, C. Q. Nguyen, C. V. Nguyen, P. V. Cuong, and N. V. Hieu, Two-dimensional van der Waals graphene/transition metal nitride heterostructures as promising high-performance nanodevices, *New Journal of Chemistry* **45**, 5509 (2021).

[114] N. T. Binh, C. Q. Nguyen, T. V. Vu, and C. V. Nguyen, Interfacial electronic properties and tunable contact types in Graphene/Janus  $\text{MoGeSiN}_4$  heterostructures, *Journal of Physical Chemistry Letters* **12**, 3934 (2021).

[115] C. V. Nguyen, C. Q. Nguyen, S.-T. Nguyen, Y. S. Ang, and N. V. Hieu, Two-dimensional metal/semiconductor contact in a Janus  $\text{MoSH}/\text{MoSi}_2\text{N}_4$  van der Waals heterostructure, *Journal of Physical Chemistry Letters* **13**, 2576 (2022).

[116] D. K. Pham, Electronic properties of a two-dimensional van der Waals  $\text{MoGe}_2\text{N}_4/\text{MoSi}_2\text{N}_4$  heterobilayer: Effect of the insertion of a graphene layer and interlayer coupling, *RSC Advances* **11**, 28659 (2021).

[117] C. Xuefeng, H. Wennan, J. Minglei, R. Fengzhu, P. Chengxiao, G. Qinfen, W. Bing, and Y. Huabing, A direct Z-scheme  $\text{MoSi}_2\text{N}_4/\text{BlueP}$  vdW heterostructure for photocatalytic overall water splitting, *Journal of Physics D: Applied Physics* **55**, 215502 (2022).

[118] A. Bafecky, M. Faraji, A. Abdollahzadeh Ziabari, M. M. Fadlallah, C. V. Nguyen, M. Ghergherehchi, and S. A. Feghhi, A van der Waals heterostructure of  $\text{MoS}_2/\text{MoSi}_2\text{N}_4$ : A first-principles study, *New Journal of Chemistry* **45**, 8291 (2021).

[119] J. Wang, X. Zhao, G. Hu, J. Ren, and X. Yuan, Manipulable electronic and optical properties of two-dimensional  $\text{MoSTe}/\text{MoGe}_2\text{N}_4$  van der Waals heterostructures, *Nanomaterials* **11**, 3338 (2021).

[120] A. Yadav, J. Kangsabanik, N. Singh, and A. Alam, Novel two-dimensional  $\text{MA}_2\text{N}_4$  materials for photovoltaic and spintronic applications, *Journal of Physical Chemistry Letters* **12**, 10120 (2021).

[121] M. Norouzi Azizabad and H. Alavi-Rad, Quasiparticle and excitonic effects in  $\text{WSi}_2\text{N}_4$  monolayer, *Physica Scripta* **96**, 125826 (2021).

[122] Y. Yu, J. Zhou, Z. Guo, and Z. Sun, Novel two-dimensional Janus  $\text{MoSiGeN}_4$  and  $\text{WSiGeN}_4$  as highly efficient photocatalysts for spontaneous overall water splitting, *ACS Applied Materials and Interfaces* **13**, 28090 (2021).

[123] C.-c. Jian, X. Ma, J. Zhang, and X. Yong, Strained  $\text{MoSi}_2\text{N}_4$  monolayers with excellent solar energy absorption and carrier transport properties,

*Journal of Physical Chemistry C* **125**, 15185 (2021).

[124] X. Lv, Y. Xu, B. Mao, G. Liu, G. Zhao, and J. Yang, Strain modulation of electronic and optical properties of monolayer MoSi<sub>2</sub>N<sub>4</sub>, *Physica E: Low-Dimensional Systems and Nanostructures* **125**, 114064 (2020).

[125] N. Mwankemwa, H.-e. Wang, T. Zhu, Q. Fan, F. Zhang, and W. Zhang, First principles calculations investigation of optoelectronic properties and photocatalytic CO<sub>2</sub> reduction of (MoSi<sub>2</sub>N<sub>4</sub>)<sub>5-n</sub>/(MoSiGeN<sub>4</sub>)<sub>n</sub> in-plane heterostructures, *Results in Physics* **37**, 105549 (2022).

[126] A. Bafeckry, C. Stampfl, M. Naseri, M. M. Fadlallah, M. Faraji, M. Ghergherehchi, D. Gogova, and S. A. Feghhi, Effect of electric field and vertical strain on the electro-optical properties of the MoSi<sub>2</sub>N<sub>4</sub> bilayer: A first-principles calculation, *Journal of Applied Physics* **129**, 155103 (2021).

[127] J. Xu, Q. Wu, Z. Sun, N. Mwankemwa, W. bin Zhang, and W. xing Yang, First-principles investigations of electronic, optical, and photocatalytic properties of Au-adsorbed MoSi<sub>2</sub>N<sub>4</sub> monolayer, *Journal of Physics and Chemistry of Solids* **162**, 110494 (2022).

[128] Z. Sun, J. Xu, N. Mwankemwa, W. Yang, X. Wu, Z. Yi, S. Chen, and W. Zhang, Alkali-metal (Li, Na, and K)-adsorbed MoSi<sub>2</sub>N<sub>4</sub> monolayer: An investigation of its outstanding electronic, optical, and photocatalytic properties, *Communications in Theoretical Physics* **74**, 015503 (2022).

[129] R. Chen, D. Chen, and W. Zhang, First-principles calculations to investigate stability, electronic and optical properties of fluorinated MoSi<sub>2</sub>N<sub>4</sub> monolayer, *Results in Physics* **30**, 104864 (2021).

[130] J. Zeng, L. Xu, Y. Yang, X. Luo, H. J. Li, S. X. Xiong, and L. L. Wang, Boosting the photocatalytic hydrogen evolution performance of monolayer C<sub>2</sub>N coupled with MoSi<sub>2</sub>N<sub>4</sub>: Density-functional theory calculations, *Physical Chemistry Chemical Physics* **23**, 8318 (2021).

[131] J. Chen and Q. Tang, The versatile electronic, magnetic and photo-electro catalytic activity of a new 2D MA<sub>2</sub>Z<sub>4</sub> Family, *Chemistry - A European Journal* **27**, 9925 (2021).

[132] C. Formed, J.-k. Yoon, K.-h. Lee, S. B. Touski, J. Xu, X. Mao, and Z.-h. Xie, Band-gap engineering, magnetic behavior and Dirac-semimetal character in the MoSi<sub>2</sub>N<sub>4</sub> nanoribbon with armchair and zigzag edges, *Journal of Physics D: Applied Physics* **55**, 035301 (2022).

[133] Y. Ding and Y. Wang, First-principles study of two-dimensional MoN<sub>2</sub>X<sub>2</sub>Y<sub>2</sub> (X=B-In, Y=N-Te) nanosheets: The III-VI analogues of MoSi<sub>2</sub>N<sub>4</sub> with peculiar electronic and magnetic properties, *Applied Surface Science* **593**, 153317 (2022).

[134] Y. Feng, Z. Wang, X. Zuo, and G. Gao, Electronic phase transition, spin filtering effect, and spin Seebeck effect in 2D high-spin-polarized VSi<sub>2</sub>X<sub>4</sub> (X = N, P, As), *Applied Physics Letters* **120**, 092405 (2022).

[135] D. Dey, A. Ray, and L. Yu, Intrinsic ferromagnetism and restrictive thermodynamic stability in MA<sub>2</sub>N<sub>4</sub> and Janus VSiGeN<sub>4</sub> monolayers, *arXiv:2203.11605* (2022).

[136] X. L. Wang, Dirac spin-gapless semiconductors: Promising platforms for massless and dissipationless spintronics and new (quantum) anomalous spin Hall effects, *National Science Review* **4**, 252 (2017).

[137] X. Wang, T. Li, Z. Cheng, X. L. Wang, and H. Chen, Recent advances in Dirac spin-gapless semiconductors, *Applied Physics Reviews* **5**, 041103 (2018).

[138] Q. Cui, Y. Zhu, J. Liang, P. Cui, and H. Yang, Spin-valley coupling in a two-dimensional VSi<sub>2</sub>N<sub>4</sub> monolayer, *Physical Review B* **103**, 085421 (2021).

[139] M. R. K. Akanda and R. K. Lake, Magnetic properties of VSi<sub>2</sub>N<sub>4</sub>, VSi<sub>2</sub>N<sub>4</sub>, and VSi<sub>2</sub>P<sub>4</sub> monolayers, *Applied Physics Letters* **119**, 052402 (2021).

[140] M. Xue, W. He, Q. Gong, M. Yi, and W. Guo, Nonlinear elasticity and strain-tunable magnetocalorics of antiferromagnetic monolayer mnps3, *Extreme Mechanics Letters* **10**, 101900 (2022).

[141] L. Webster and J. A. Yan, Strain-tunable magnetic anisotropy in monolayer CrCl<sub>3</sub>, CrBr<sub>3</sub>, and CrI<sub>3</sub>, *Physical Review B* **98**, 144411 (2018).

[142] S. Zheng, C. Huang, T. Yu, M. Xu, S. Zhang, H. Xu, Y. Liu, E. Kan, Y. Wang, and G. Yang, High-temperature ferromagnetism in an Fe<sub>3</sub>P monolayer with a large magnetic anisotropy, *Journal of Physical Chemistry Letters* **10**, 2733 (2019).

[143] H. L. Zhuang, P. R. Kent, and R. G. Henning, Strong anisotropy and magnetostriction in the two-dimensional Stoner ferromagnet Fe<sub>3</sub>GeTe<sub>2</sub>, *Physical Review B* **93**, 134407 (2016).

[144] H. Han, H. Zheng, Q. Wang, and Y. Yan, Enhanced magnetic anisotropy and Curie temperature of the NiI<sub>2</sub> monolayer by applying strain: A first-principles study, *Physical Chemistry Chemical Physics* **22**, 26917 (2020).

[145] E. Torun, H. Sahin, C. Bacaksiz, R. T. Senger, and F. M. Peeters, Tuning the magnetic anisotropy in single-layer crystal structures, *Physical Review B* **92**, 104407 (2015).

[146] B. Huang, G. Clark, E. Navarro-Moratalla, D. R. Klein, R. Cheng, K. L. Seyler, D. Zhong, E. Schmidgall, M. A. McGuire, D. H. Cobden, W. Yao, D. Xiao, P. Jarillo-Herrero, and X. Xu, Layer-dependent ferromagnetism in a van der Waals crystal down to the monolayer limit, *Nature* **546**, 270 (2017).

[147] Z. Fei, B. Huang, P. Malinowski, W. Wang, T. Song, J. Sanchez, W. Yao, D. Xiao, X. Zhu, A. F. May, W. Wu, D. H. Cobden, J. H. Chu, and X. Xu, Two-dimensional itinerant ferromagnetism in atomically thin Fe<sub>3</sub>GeTe<sub>2</sub>, *Nature Materials* **17**, 778 (2018).

[148] J. Y. You, Z. Zhang, X. J. Dong, B. Gu, and G. Su, Two-dimensional magnetic semiconductors with room Curie temperatures, *Physical Review Research* **2**, 013002 (2020).

[149] Z. Jiang, P. Wang, J. Xing, X. Jiang, and J. Zhao, Screening and design of novel 2D ferromagnetic materials with high Curie temperature above room temperature, *ACS Applied Materials and Interfaces* **10**, 39032 (2018).

[150] Y. Li, J. Wang, G. Yang, and Y. Liu, Strain-induced magnetism in MSi<sub>2</sub>N<sub>4</sub> (M = V, Cr): A first-principles study, *Annalen der Physik* **533**, 2100273 (2021).

[151] A. Ray, S. Tyagi, N. Singh, and U. Schwingenschlögl, Inducing half-metallicity in monolayer MoSi<sub>2</sub>N<sub>4</sub>, *ACS Omega* **6**, 30371 (2021).

[152] M. A. Abdelati, A. A. Maarouf, and M. M. Fadlallah, Substitutional transition metal doping in MoSi<sub>2</sub>N<sub>4</sub> monolayer: Structural, electronic and magnetic properties, *Physical Chemistry Chemical Physics* **24**, 3035 (2022).

[153] M. Yi, B. X. Xu, R. Müller, and D. Gross, Strain-mediated magnetoelectric effect for the electric-field control of magnetic states in nanomagnets,

*Acta Mechanica* **230**, 1247 (2019).

[154] D. Sander, The correlation between mechanical stress and magnetic anisotropy in ultrathin films, *Reports on Progress in Physics* **62**, 809 (1999).

[155] Q. Gong, M. Yi, and B. X. Xu, Electric field induced magnetization reversal in magnet/insulator nanoheterostructure, *International Journal of Smart and Nano Materials* **11**, 298 (2020).

[156] I. J. Park, S. Kwon, and R. K. Lake, Effects of filling, strain, and electric field on the Néel vector in antiferromagnetic CrSb, *Physical Review B* **102**, 224426 (2020).

[157] J. Yuan, Q. Wei, M. Sun, X. Yan, Y. Cai, L. Shen, and U. Schwingenschlögl, Protected valley states and generation of valley- and spin-polarized current in monolayer  $MA_2Z_4$ , *Physical Review B* **105**, 195151 (2022).

[158] Z. Cui, K. Yang, K. Ren, S. Zhang, and L. Wang, Adsorption of metal atoms on  $MoSi_2N_4$  monolayer: A first principles study, *Materials Science in Semiconductor Processing* **152**, 107072 (2022).

[159] B. Li, J. Geng, H. Ai, Y. Kong, H. Bai, K. H. Lo, K. W. Ng, Y. Kawazoe, and H. Pan, Design of 2D materials- $MSi_2C:ZN_{4-x}$  ( $M = Cr, Mo$ , and  $W$ ;  $X=1$  and 2)-with tunable electronic and magnetic properties, *Nanoscale* **13**, 8038 (2021).

[160] S. Li, W. Wu, X. Feng, S. Guan, W. Feng, Y. Yao, and S. A. Yang, Valley-dependent properties of monolayer  $MoSi_2N_4$ ,  $WSi_2N_4$ , and  $MoSi_2As_4$ , *Physical Review B* **102**, 235435 (2020).

[161] H. Ai, D. Liu, J. Geng, S. Wang, K. H. Lo, and H. Pan, Theoretical evidence of the spin-valley coupling and valley polarization in two-dimensional  $MoSi_2X_4$  ( $X = N, P$ , and  $As$ ), *Physical Chemistry Chemical Physics* **23**, 3144 (2021).

[162] Y. Liu, T. Zhang, K. Dou, W. Du, R. Peng, Y. Dai, B. Huang, and Y. Ma, Valley-contrasting physics in single-layer  $CrSi_2N_4$  and  $CrSi_2P_4$ , *Journal of Physical Chemistry Letters* **12**, 8341 (2021).

[163] S. Sheoran, D. Gill, A. Phutela, and S. Bhattacharya, Coupled spin-valley, Rashba effect and hidden persistent spin polarization in  $WSi_2N_4$  family, *arXiv:2208.00127* (2022).

[164] C. Yang, Z. Song, X. Sun, J. Lu, L. Berkeley, and O. P. Materials, Valley pseudospin in monolayer  $MoSi_2N_4$  and  $MoSi_2As_4$ , *Physical Review B* **103**, 035308 (2020).

[165] X. Feng, X. Xu, Z. He, R. Peng, Y. Dai, B. Huang, and Y. Ma, Valley-related multiple Hall effect in monolayer  $VSi_2P_4$ , *Physical Review B* **104**, 075421 (2021).

[166] S. Li, Q. Wang, C. Zhang, P. Guo, and S. A. Yang, Correlation-driven topological and valley states in monolayer  $VSi_2P_4$ , *Physical Review B* **104**, 085149 (2021).

[167] Y. Wang and Y. Ding, Switchable valley polarization and quantum anomalous Hall state in the  $VN_2X_2Y_2$  nanosheets ( $X = \text{group-III}$  and  $Y = \text{group-VI}$  elements), *Applied Physics Letters* **119**, 193101 (2021).

[168] X. Sun, Z. Song, N. Huo, S. Liu, C. Yang, J. Yang, W. Wang, and J. Lu, Performance limit of monolayer  $MoSi_2N_4$  transistors, *Journal of Materials Chemistry C* **9**, 14683 (2021).

[169] J. Huang, P. Li, X. Ren, and Z. X. Guo, Promising properties of a sub-5-nm monolayer  $MoSi_2N_4$  transistor, *Physical Review Applied* **16**, 044022 (2021).

[170] B. Ye, X. Jiang, Y. Gu, G. Yang, Y. Liu, H. Zhao, X. Yang, C. Wei, X. Zhang, and N. Lu, Quantum transport of short-gate MOSFETs based on monolayer  $MoSi_2N_4$ , *Physical Chemistry Chemical Physics* **24**, 6616 (2022).

[171] N. Ghobadi, M. Hosseini, and S. B. Touski, Field-effect transistor based on  $MoSi_2N_4$  and  $WSi_2N_4$  monolayers under biaxial strain: A computational study of the electronic properties, *IEEE Transactions on Electron Devices* **69**, 863 (2022).

[172] K. Nandan, G. S. Member, B. Ghosh, A. Agarwal, and S. Bhowmick, Two-dimensional  $MoSi_2N_4$ : An excellent 2-D semiconductor for field-effect transistors, *IEEE Transactions on Electron Devices* **69**, 406 (2022).

[173] H. Zhang, B. Shi, L. Xu, J. Yan, W. Zhao, Z. Zhang, Z. Zhang, and J. Lu, Sub-5 nm monolayer  $MoS_2$  transistors toward low-power devices, *ACS Applied Electronic Materials* **3**, 1560 (2021).

[174] S. Zhu and D. Wang, Photocatalysis: Basic principles, diverse forms of implementations and emerging scientific opportunities, *Advanced Energy Materials* **7**, 1700841 (2017).

[175] Y. Li, C. Gao, R. Long, and Y. Xiong, Photocatalyst design based on two-dimensional materials, *Materials Today Chemistry* **11**, 197 (2019).

[176] W. Shi, G. Yin, S. Yu, T. Hu, and X. Wang, Atomic precision tailoring of two-dimensional  $MoSi_2N_4$  as electrocatalyst for hydrogen evolution reaction, *Journal of Materials Science* (2022).

[177] J. Zhao, Y. Zhao, H. He, P. Zhou, Y. Liang, and T. Frauenheim, Stacking engineering: A boosting strategy for 2D photocatalysts, *Journal of Physical Chemistry Letters* **12**, 10190 (2021).

[178] G. Hussain, M. Manzoor, M. W. Iqbal, I. Muhammad, A. Bafecky, H. Ullah, and C. Autieri, Strain modulated electronic and optical properties of laterally stitched  $MoSi_2N_4/XSi_2N_4$  ( $X=W, Ti$ ) 2D heterostructures, *Physica E: Low-dimensional Systems and Nanostructures* **144**, 1154 (2022).

[179] Y. T. Ren, L. Hu, Y. T. Chen, Y. J. Hu, J. L. Wang, P. L. Gong, H. Zhang, L. Huang, and X. Q. Shi, Two-dimensional  $MSi_2N_4$  monolayers and van der Waals heterostructures: Promising spintronic properties and band alignments, *Physical Review Materials* **6**, 064006 (2022).

[180] Y. Zang, Q. Wu, W. Du, Y. Dai, B. Huang, and Y. Ma, Activating electrocatalytic hydrogen evolution performance of two-dimensional  $MSi_2N_4$  ( $M=Mo, W$ ): A theoretical prediction, *Physical Review Materials* **5**, 045801 (2021).

[181] W. Qian, Z. Chen, J. Zhang, and L. Yin, Monolayer  $MoSi_2N_{4-x}$  as promising electrocatalyst for hydrogen evolution reaction: A DFT prediction, *Journal of Materials Science and Technology* **99**, 215 (2022).

[182] C. Xiao, R. Sa, Z. Cui, S. Gao, W. Du, X. Sun, X. Zhang, Q. Li, and Z. Ma, Enhancing the hydrogen evolution reaction by non-precious transition metal (Non-metal) atom doping in defective  $MoSi_2N_4$  monolayer, *Applied Surface Science* **563**, 150388 (2021).

[183] Y. Luo, M. Li, Y. Dai, X. Zhang, R. Zhao, F. Jiang, C. Ling, and Y. Huang, Screening of effective NRR electrocatalysts among the Si-based  $MSi_2N_4$  ( $M = Ti, Zr, Hf, V, Nb, Ta, Cr, Mo$ , and  $W$ ) monolayers, *Journal of Materials Chemistry A* **9**, 15217 (2021).

[184] S. Lu, Y. Zhang, F. Lou, K. Guo, and Z. Yu, Non-precious metal activated  $\text{MoSi}_2\text{N}_4$  monolayers for high-performance OER and ORR electrocatalysts: A first-principles study, *Applied Surface Science* **579**, 152234 (2022).

[185] M. R. Sahoo, A. Ray, and N. Singh, Theoretical insights into the hydrogen evolution reaction on  $\text{VGe}_2\text{N}_4$  and  $\text{NbGe}_2\text{N}_4$  monolayers, *ACS Omega* **7**, 7837 (2022).

[186] Y. Liu, Y. Ji, and Y. Li, Multilevel theoretical screening of novel two-dimensional  $\text{MA}_2\text{Z}_4$  family for hydrogen evolution, *Journal of Physical Chemistry Letters* **12**, 9149 (2021).

[187] J. Zheng, X. Sun, J. Hu, S. Wang, Z. Yao, S. Deng, X. Pan, Z. Pan, and J. Wang, Symbolic transformer accelerating machine learning screening of hydrogen and deuterium evolution reaction catalysts in  $\text{MA}_2\text{Z}_4$  materials, *ACS Applied Materials and Interfaces* **13**, 50878 (2021).

[188] Y. Chen, S. Tian, and Q. Tang, First-principles studies on electrocatalytic activity of novel two-dimensional  $\text{MA}_2\text{Z}_4$  monolayers toward oxygen reduction reaction, *Journal of Physical Chemistry C* **125**, 22581 (2021).

[189] C. Lin, X. Feng, D. Legut, X. Liu, Z. W. Seh, R. Zhang, and Q. Zhang, Discovery of efficient visible-light driven oxygen evolution photocatalysts: Automated high-throughput computational screening of  $\text{MA}_2\text{Z}_4$ , *Advanced Functional Materials*, 2207415 (2022).

[190] Z. Wang, G. Zhang, Y. Wang, C. Huang, Y. Liu, C. Ouayng, and J. Hu, Heavy 2D  $\text{VSi}_2\text{N}_4$ : High capacity and full battery open-circuit voltage as Li/Na-ion batteries anode, *Applied Surface Science* **593**, 153354 (2022).

[191] X. M. Li, Z. Z. Lin, L. R. Cheng, and X. Chen, Layered  $\text{MoSi}_2\text{N}_4$  as electrode material of Zn–Air battery, *Physica Status Solidi - Rapid Research Letters* **16**, 2200007 (2022).

[192] R. E. Munteanu, P. S. Moreno, M. Bramini, and S. Gáspár, 2D materials in electrochemical sensors for in vitro or in vivo use, *Analytical and Bioanalytical Chemistry* **413**, 701 (2020).

[193] D. J. Buckley, N. C. Black, E. G. Castanon, C. Melios, M. Hardman, and O. Kazakova, Frontiers of graphene and 2D material-based gas sensors for environmental monitoring, *2D Materials* **7**, 032002 (2020).

[194] D. Tyagi, H. Wang, W. Huang, L. Hu, Y. Tang, Z. Guo, Z. Ouyang, and H. Zhang, Recent advances in two-dimensional-material-based sensing technology toward health and environmental monitoring applications, *Nanoscale* **12**, 3535 (2020).

[195] K. Li, W. Yang, M. Yi, and Z. Shen, Graphene-based pressure sensor and strain sensor for detecting human activities, *Smart Materials and Structures* **30**, 085027 (2021).

[196] B. B. Subbanna, K. Choudhary, S. Singh, and S. Kumar, 2D material-based optical sensors: a review, *ISSS Journal of Micro and Smart Systems* **11**, 169 (2022).

[197] A. Bafeekry, M. Faraji, M. M. Fadlallah, A. Abdolahzadeh Ziabari, A. Bagheri Khatibani, S. A. Feghhi, M. Ghergherehchi, and D. Gogova, Adsorption of habitat and industry-relevant molecules on the  $\text{MoSi}_2\text{N}_4$  monolayer, *Applied Surface Science* **564**, 150326 (2021).